CrossMark

Orbital and Absolute Magnitude Distribution of Jupiter Trojans

David Vokrouhlický[1] ⓘ, David Nesvorný[2] ⓘ, Miroslav Brož[1] ⓘ, William F. Bottke[2] ⓘ, Rogerio Deienno[2] ⓘ, Carson D. Fuls[3], and Frank C. Shelly[3]

[1] Astronomical Institute, Charles University, V Holešovičkách 2, CZ 18000, Prague 8, Czech Republic; vokrouhl@cesnet.cz
[2] Department of Space Studies, Southwest Research Institute, 1050 Walnut Street, Suite 300, Boulder, CO 80302, USA
[3] Lunar and Planetary Laboratory, The University of Arizona, 1629 E. University Boulevard, Tucson, AZ 85721-0092, USA
Received 2023 November 16; revised 2024 January 12; accepted 2024 January 22; published 2024 February 28

Abstract

Jupiter Trojans (JTs) librate about the Lagrangian stationary centers L4 and L5 associated with this planet on typically small-eccentricity and moderate-inclination heliocentric orbits. The physical and orbital properties of JTs provide important clues about the dynamical evolution of the giant planets in the early solar system, as well as populations of planetesimals in their source regions. Here we use decade-long observations from the Catalina Sky Survey (station G96) to determine the bias-corrected orbital and magnitude distributions of JTs. We distinguish the background JT population, filling smoothly the long-term stable orbital zone about L4 and L5 points and collisional families. We find that the cumulative magnitude distribution of JTs (the background population in our case) has a steep slope for $H \leqslant 9$, followed by a moderately shallow slope until $H \simeq 14.5$, beyond which the distribution becomes even shallower. At $H = 15$ we find a local power-law exponent 0.38 ± 0.01. We confirm the asymmetry between the magnitude-limited background populations in L4 and L5 clouds characterized by a ratio 1.45 ± 0.05 for $H < 15$. Our analysis suggests an asymmetry in the inclination distribution of JTs, with the L4 population being tighter and the L5 population being broader. We also provide a new catalog of the synthetic proper elements for JTs with an updated identification of statistically robust families (9 at L4, and 4 at L5). The previously known Ennomos family is found to consist of two overlapping Deiphobus and Ennomos families.

Unified Astronomy Thesaurus concepts: Solar system astronomy (1529); Small Solar System bodies (1469)

1. Introduction

Jupiter Trojans (JTs), objects librating about the stationary Lagrangian centers L4 and L5 accompanying this planet, have a special status among the populations of small bodies in the solar system. Their fundamental role is twofold. First, they represent an outpost of the distant heliocentric populations that are difficult to reach by ground-based observations. Understanding JTs therefore has broader implications for the small-body populations far beyond Jupiter. Second, because of their strong gravitational coupling to Jupiter, the properties of the Trojan populations provide unique information about the orbital history of this planet, and in fact the early fate of the giant planets in general. Additionally, a special circumstance of the JTs is their duality: they are organized in two swarms, one about the leading center L4 and the other about the trailing center L5. Once the objects became part of their respective Trojan clan, they became disconnected from each other (both dynamically and collisionally). However, before that moment, they were, in all likelihood, part of the same population of planetesimals born in the trans-Neptunian region.

In this paper, we adopt the presently favored capture hypothesis about the Trojan origin associated with Jupiter's chaotic orbital evolution during the giant planet's reconfiguration (e.g., Morbidelli et al. 2005; Nesvorný et al. 2013; Nesvorný 2018). Alternative models, such as in situ Trojan formation, Jupiter's large-scale inward migration leading to gas-drag-assisted capture, or capture related to the terminal runaway mass increase of Jupiter due to a collapse of its gaseous envelope, all have more difficulty matching JT constraints than the aforementioned orbitally triggered capture mechanism. (see also reviews by Marzari et al. 2002; Slyusarev & Belskaya 2014; Emery et al. 2015).

We argue that substantial differences in the parameters of the L4 and L5 swarms may provide important clues about (i) the capture mechanism, and/or (ii) the post-capture evolution of one (or both) of the swarms. Aspects that have grown enigmatic over the past decades are (i) the putative population asymmetry between the two swarms, and (ii) differences in their inclination distribution (and a closely related issue of the Trojan families).

Denoting the magnitude-limited populations of the L4 and L5 Trojan swarm by N_4 and N_5, we define their ratio $f_{45} = N_4/N_5$ to help us investigate a potential asymmetry. As an aside, we note that Grav et al. (2011) and Grav et al. (2012) do not report any statistically significant difference in albedo-size dependence of the L4 and L5 populations, yet they note small differences in albedo distribution and taxonomy. This means that one needs to be cautious about interpreting the magnitude-limited asymmetry as an equal measure of the size-limited asymmetry. It is possible that a small change in albedo for each population may influence the link (see Section 6).

Deviation of f_{45} from unity was considered as soon as the known Trojan population grew sizable. Still, studies up to the late 1990s had to face small samples of detected Trojans in both swarms and, in the absence of solid debiasing efforts, asymmetric observational incompleteness (implying the intrinsic f_{45} value was different from what plain observations provided, e.g., Shoemaker et al. 1989). The situation started to change in the 2000s with a flood of new data from powerful and well-characterized sky surveys. For example, Szabó et al. (2007) analyzed a sample of about 900 JTs (and candidate

Trojans) in nearly five years of the Sloan Digital Sky Survey (SDSS) observations. These authors found $f_{45} = 1.6 \pm 0.1$ down to the inferred $H \simeq 13.8$ mag completeness.

In a second example, Nakamura & Yoshida (2008) used observations of the 8.2 m Subaru telescope in a campaign conducted during the 2001 season to characterize the L4 and L5 populations to small sizes. They adopted an empirical distribution function of the ecliptic longitude and latitude to characterize the sky-plane density of Trojans near their respective libration center. Using this approach, these authors found $f_{45} = 1.85 \pm 0.42$ for $D > 2$ km (assuming a fixed albedo of 0.04).

In a third example, Grav et al. (2011) analyzed space-borne observations of more than 2000 known and candidate JTs taken by the Wide-field Infrared Survey Explorer (WISE) during its half-year cryogenic phase and about the same timespan of the postcryogenic extension. The strength of the WISE multiband observations in infrared is their ability to determine the size of the targets. Albedos can then be inferred, provided the absolute magnitudes of the targets are well characterized. In what these authors called a preliminary debiasing effort, Grav et al. (2011) found $f_{45} = 1.4 \pm 0.2$ for $D > 10$ km JTs.

As a preamble of our work, we present a highly simplified guess of the asymmetry parameter f_{45} from today's data based on the following reasoning (we shall largely substantiate this result in Section 5). We find it plausible that the photometric completion of the Trojan clouds as of today is close to $H_c \simeq 13.8$ mag (this is near the 10 km limit considered by Grav et al. 2011, assuming a mean geometric albedo of $p_V \simeq 0.075$). This value is consistent with the modestly lower completion limit of Catalina Sky Survey (CSS) observations between 2013 and 2022; we will analyze these data below (Section 5). It also matches the results from Hendler & Malhotra (2020). The Minor Planet Center (MPC) orbital database contains $N_4 \simeq 2040$ and $N_5 \simeq 1410$ Trojans with $H \leqslant H_c$ after subtracting populations of the major families identified in Appendix A (Table 4). Adopting a naive $\simeq \sqrt{N}$ population uncertainty, which is probably an underestimate, we would estimate that $f_{45} = 1.45$ with an uncertainty $\simeq f_{45} [(1/N_4) + (1/N_5)]^{1/2} \simeq 0.05$, thus $f_{45} = 1.45 \pm 0.05$ for $H \leqslant H_c$. This result is close to the value reported in Grav et al. (2011).

Another aspect of the L4 and L5 swarm asymmetry, often discussed by previous studies, concerns the orbital inclination distribution. For instance, Jewitt et al. (2000) analyzed data from a week-long campaign using the University of Hawaii 2.2 m telescope to observe a sector of the L4 swarm and detected 93 Trojans. Assuming a simple Gaussian sky-plane density distribution function and approximate relation of the sky-plane motion of the detected Trojan to the inclination of its heliocentric orbit, these authors determined the biased-corrected inclination distribution of the L4 Trojans in the 0°–30° range. They observed a bimodality with maxima at $\simeq 9°$ and $\simeq 19°$. Earlier observations of the L5 Trojans did not show this structure (see already Degewij & van Houten 1979). Instead, the L5 swarm inclinations were recognized to extend to larger values with a maximum near $\simeq 27°$. Slyusarev & Belskaya (2014) sum up the inclination data, working with the observed biased populations, and refer to the above-mentioned differences as an unsolved problem. We note that this inclination difference was also discussed and analyzed in Pirani et al. (2019a).

These reported anomalies can be explained by the presence of the Trojan families, mainly Eurybates, Arkesilaos, and Hektor in L4 and the Ennomos/Deiphobus clan in L5 (see, e.g., Figures 10 and 28, or data in Table 4). As discussed below, the families are strongly concentrated in inclination, and the principal clans may contain a substantial number of members. In this sense, the inclination problem is also closely related to the population problem mentioned above. An objective comparison of the L4 and L5 populations must subtract the family contribution before performing any analysis. Nevertheless, the issues with Trojan inclinations lead to more issues to consider, namely the number and properties of the Trojan families in the L4 and L5 populations. There seem to be differences between the two swarms that warrant an explanation.

Accordingly, understanding the differences in the Jupiter Trojan L4 and L5 populations requires analysis of both the orbital and magnitude (or size) frequency distributions. In Section 2 we review the presently known JT populations and discuss what has been detected by CSS. The latter will form the basis of our analysis. The reason is that most CCS data were carefully characterized, which allows us to calculate a bias-corrected model. Some of the complex bias features are illustrated in Section 2, with further details provided in Appendix B. In Section 3 we introduce our model for the orbital architecture of the JTs, as well as the assumption about their magnitude distribution. In both cases, we distinguish two components: (i) the background continuous population, and (ii) Trojans in the discrete families. As to the latter, we consider eight prominent families (five in the L4 swarm and three in the L5 swarm), all newly identified in Appendix A. In Section 4 we describe the complete (bias-corrected) Trojan populations from the bias-affected observations. This will include (i) the definition of the detection probability as well as how it maps onto our model parameters (Section 4.1), and (ii) numerical tools that can find the model that best matches the available observations (Section 4.2). Our results are summarized in Section 5, with our conclusions discussed in Section 6. As a part of our project, we determined a new catalog of JT proper orbital elements and identified an updated set of Trojan families, both of which are provided in Appendix A.

2. The Observed Trojan Population

In this section, we will discuss the currently known population of JTs. Next, we will determine what fraction has been detected by CSS and briefly discuss the most important selection effects.
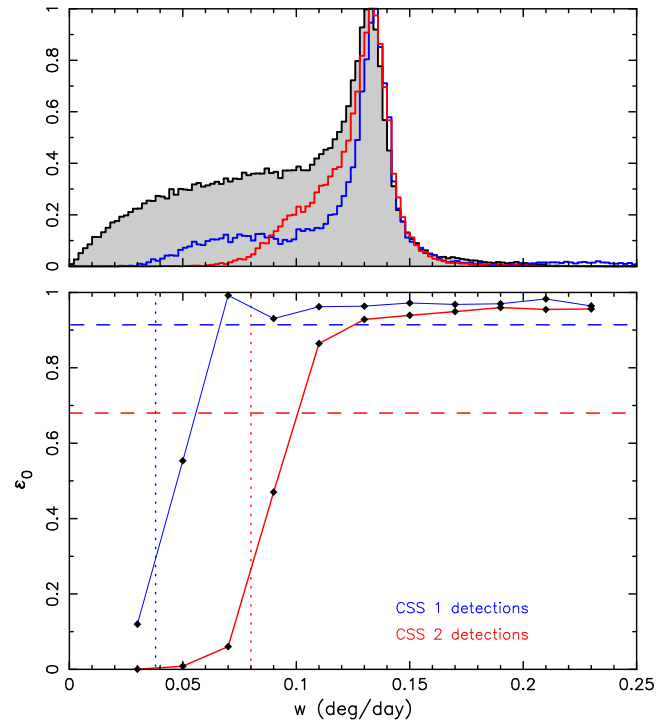
Population of known Jupiter Trojans. We determined the currently known population of JTs using a two-step scheme. First, we downloaded the orbital catalog `MPCORB.DAT` from the Minor Planet Center website (the 2023 February 22 version). Next, we selected all inputs using simple criteria in osculating orbital elements that were available for a common epoch of MJD 60,000. The initial database represented about 1,245,000 orbits, but about 2% were rejected because they reflected poorly determined single-opposition orbits given at different, mostly earlier epochs. The orbital selection was: (i) semimajor axis a in between 4.95 and 5.45 au, (ii) eccentricity smaller than 0.6, (iii) inclination smaller than 50°, and (iv) absolute value of the resonant angle σ larger than 20° and smaller than 130°. This search resulted in 7929 orbits around the L4 libration center and 4189 orbits around the L5 libration center. A small number of these orbits, however, correspond to

unstable Jupiter family comets masquerading as JTs. This led us to numerically propagate all selected orbits, together with all planets and the Sun, for a 1 Myr timespan. We found that 26 and 12 candidate Trojans near L4 and L5, respectively, escaped from the libration region about their Lagrange center, were discarded from the simulation by striking Jupiter, or were ejected from the Solar system. The remaining 7903 bodies near L4 and 4177 bodies near L5 were found to reside in the resonant zone of their respective center, with their σ librating for the entire timespan of the integration. Note that additional losses might occur if the integration was extended, but we believe the selected population is sufficient for our needs.

Catalina Sky Survey observations of Jupiter Trojans. We now use the Trojans identified in the MPC database to determine which of them were detected by the Catalina Sky Survey.[4] CSS, managed by the Lunar and Planetary Laboratory of the University of Arizona, is one of the two most prolific survey programs that have been in action over the past decade (e.g., Christensen et al. 2019). Its principal mission is to discover and further track near-Earth objects, aiming at the characterization of a significant fraction of the population with sizes as small as 140 m. However, CSS is an invaluable source of data for other solar system studies as well (e.g., Vokrouhlický et al. 2023, leaving aside numerous applications of CSS data in studies of variable stars and optical transients), and this also includes the JT population.

In this paper, we use observations of the CSS 1.5 m survey telescope located at Mt. Lemmon (MPC observatory code G96). Nesvorný et al. (2024) carefully evaluated the asteroid detection probability for the G96 operations in the period between 2013 January and 2022 June. Additionally, this interval has been divided into two phases: (i) observations before 2016 May 14 (phase I), and (ii) observations after 2016 May 31 (phase II). Not only is the second phase longer, allowing the survey to collect more observations (the available database contains 61,585 well-characterized frames— sequences of four, typically 30 s exposure images—during phase I and 162,280 well-characterized frames during phase II), but the primary difference stems from an important upgrade of the CCD camera in the second half of 2016 May. The new camera has a 4 times larger field of view, and even slightly better photometric sensitivity, allowing it to cover a much larger latitude region about the ecliptic (its only drawback is the large pixel size, as discussed below). Investigating this database, we found the following. In phase I, there were (i) 14,303 detections of 4551 individual bodies librating about the L4 center and 7230 detections of 2460 individual bodies librating about the L5 center. In phase II, there were 40,832 detections of 6307 individual bodies librating about the L4 center and 18,293 detections of 3041 individual bodies librating about the L5 center. As a result, the CSS operations during the 2013–2022 period were powerful enough to detect 75–80% of the known Trojans. The remaining 20–25% of cases that escaped CSS attention were discovered and/or detected by other surveys (such as Pan-STARRS) or were detected by CSS only after 2022 June 14 (the last date for which we have characterized the survey's performance).

Selection effects that have an influence on CSS observations. The completeness of the population data in the CCS observations is affected by two broad categories of effects:

Figure 1. Upper panel: intrinsic distribution of the apparent motion of Jupiter Trojans in the fields of view of CSS phase II (determined from a modeled synthetic population of objects) is shown by the black histogram with gray shading. The color-coded histograms are the apparent motion distributions of the detected Trojans (red for L4 and blue for L5 Trojans); all distributions are normalized to maximum. Detected populations miss the tail of very slowly moving objects (see below). Lower panel: mean value of the bright-end detection probability ϵ_0 of the CSS observations during phase I (red) and phase II (blue) as a function of the apparent motion w on the CCD detector of G96 (abscissa in deg day^{-1}). The horizontal dashed lines are global average values of ϵ_0 over all w values, and the vertical dotted lines denote a critical w value for which ϵ_0 drops to $\simeq 0.25$. The drop in the detection efficiency below $\simeq 0.04$ deg day^{-1} (phase I) and $\simeq 0.08$ deg day^{-1} (phase II) is related to a finite pixel size of the detector, preventing the identification of a clear tracklet for a slowly moving Trojan image.

(i) the *geometric bias*, expressing completeness of the CSS fields of view coverage of the sky zone onto which Trojans project, and (ii) the *photometric bias*, constraining our ability to detect objects in the Trojan population due to telescope/detector limitations. The photometric bias itself represents a set of complicated phenomena, whose origin is twofold: (a) the telescope's and detector's ability to record signals up to a certain limit, beyond which the observed Trojan is too faint and therefore undetected, and (b) the ability to identify the Trojan as a moving object on a stellar background. We use a detailed and properly calibrated formulation of the CSS detection efficiency developed by Nesvorný et al. (2024) within a project to create a new model of the near-Earth object (NEO) population. While the faintness problem is the same, the critical issues of the identification problem for NEOs and Trojans are just the opposite. Denoting the apparent motion of the observed object on the CCD camera by w, a delicate issue to face in NEO detection is the limit of its large values ($w \geqslant 5$ deg day^{-1}, say). Yet, this case is important because the smallest NEOs may only be detected during their close encounters with the Earth when the apparent motion is high. In Trojans, the opposite limit of very small w values may be a source of trouble. This is because when w is too small, $w \leqslant 0.04$ deg day^{-1} in phase I and $w \leqslant 0.08$ deg day^{-1} in phase II (Figure 1), the record of the Trojan does not allow one
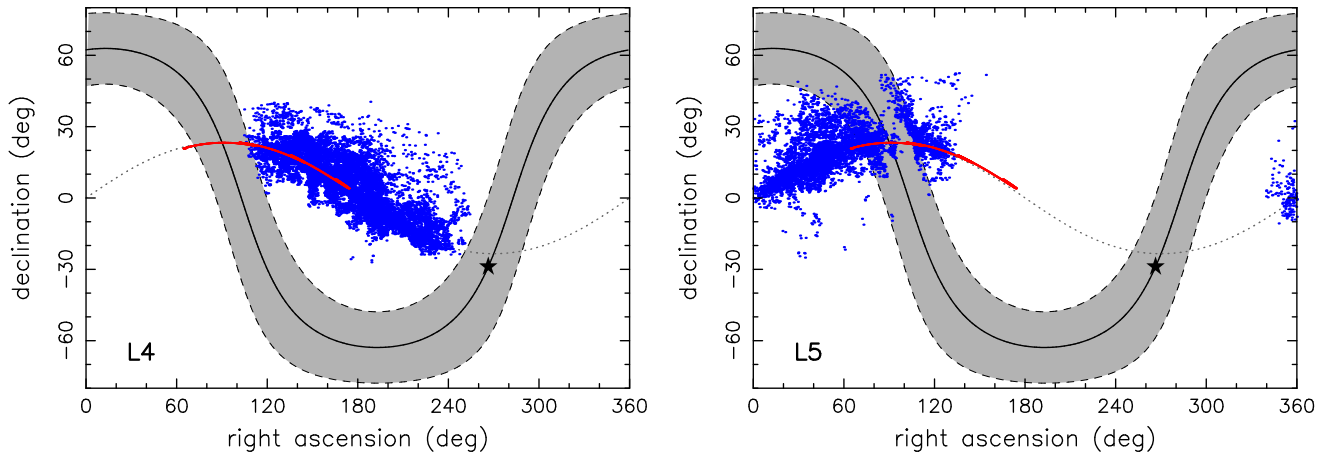
Figure 2. Jupiter Trojan detections by the CSS operations between 2013 January 2 and 2016 May 14 (phase I). There are 14,303 detections of 4551 individual bodies librating about the L4 center (left panel) and 7230 detections of 2460 individual bodies librating about the L5 center (right panel). The blue symbols are topocentric R.A. (abscissa) and decl. (ordinate) of the observations. The red line is the Jupiter track in the same period of time near the ecliptic plane (dotted line). The solid black line is the projection of the galactic plane surrounded by the $\pm 15°$ latitude strip (gray region). The black star is the direction of the galactic center.
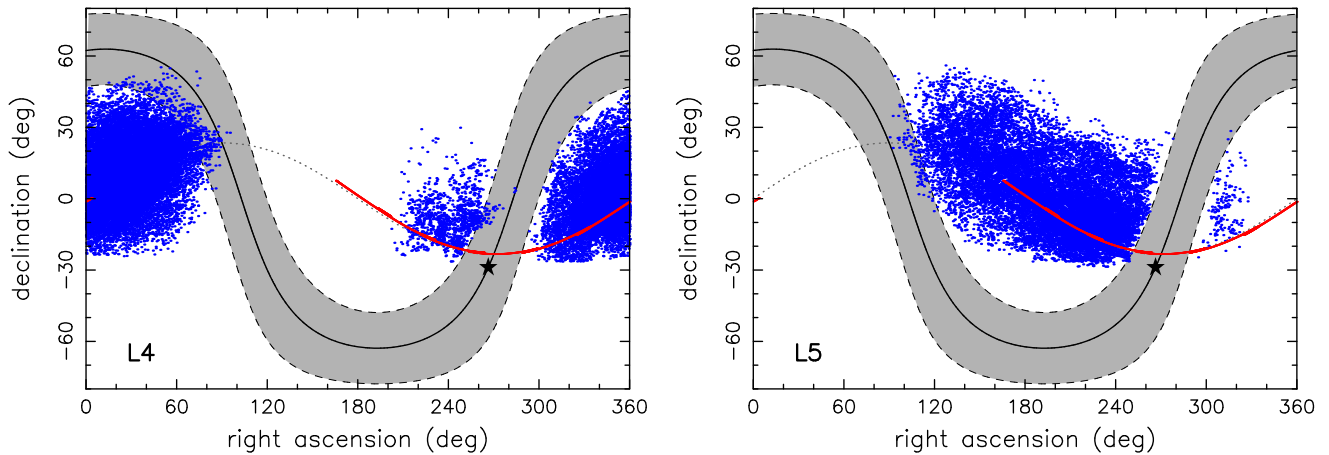
Figure 3. Jupiter Trojan detections by the CSS operations between 2016 May 31 and 2022 June 14 (phase II). There are 40,832 detections of 6307 individual bodies librating about the L4 center (left panel) and 18,293 detections of 3041 individual bodies librating about the L5 center (right panel). The blue symbols are topocentric R.A. (abscissa) and decl. (ordinate) of the observations. The red line is the Jupiter track in the same period of time near the ecliptic plane (dotted line). The solid black line is the projection of the galactic plane surrounded by the $\pm 15°$ latitude strip (gray region). The black star is the direction of the galactic center. The observations primarily avoid pointing toward crowded stellar fields near the galactic center.

to construct a recognizable tracklet. The identification may even fail for very bright objects. We therefore extended the analysis of Nesvorný et al. (2024) to allow reliable determination of the detection efficiency in the very small limit of w.

As an example of our analysis, we show in Figure 1 how the bright-object limit of the detection probability ϵ_0 depends on w in both phases of the CSS operations. Interestingly, phase I may reach Trojans down to smaller w values than in phase II, which is otherwise superior in many respects. This is because the larger pixel size of the new camera installed in 2016 May requires faster moving Trojans to spread their trail on the detector over a sufficient number of different pixels, defining thus a characteristic tracklet.

Next, we briefly describe the various geometric and additional photometric aspects of the bias in Trojan observations (overall, one may argue that observations of planetary Trojans, including those of Jupiter, could serve as a textbook example of a plethora of bias phenomena). An insight into this component of the bias is provided by Figures 2–4. There are two basic periods modulating this part of the bias, namely (i)

the annual effect (in fact $\simeq 1.09$ yr effect of Jupiter's synodic period with respect to the Earth), simply dictating when the respective cloud appears at opposition on the night sky, and (ii) a $\simeq 11.9$ yr cycle of Jupiter's heliocentric revolution. This latter has an influence on the position of libration centers L4 and L5 on the sky in absolute terms. Locations near the galactic plane are observationally prohibited and could cause an absence of the data (see, e.g., a small number of L4 Trojan detections from 2017 to 2019 in Figure 4). As a result, a survey lasting less than $\simeq 11.9$ yr may suffer from highly unbalanced observational conditions for the two clouds. The CSS data available to us spans 9.5 yr. While not ideal, the geometric limitations are fortunately not severe, and neither L4 nor L5 Trojans are underrepresented in the observations.

The second bias component is photometric (see Figures 5 and 6). In fact, limitations of detectability may affect both bright and faint objects. This is, for instance, the case for main belt observations by CSS, which did not detect the brightest bodies (e.g., Ceres or Juno). Luckily, this problem does not appear to affect the Trojan data, for which even the largest
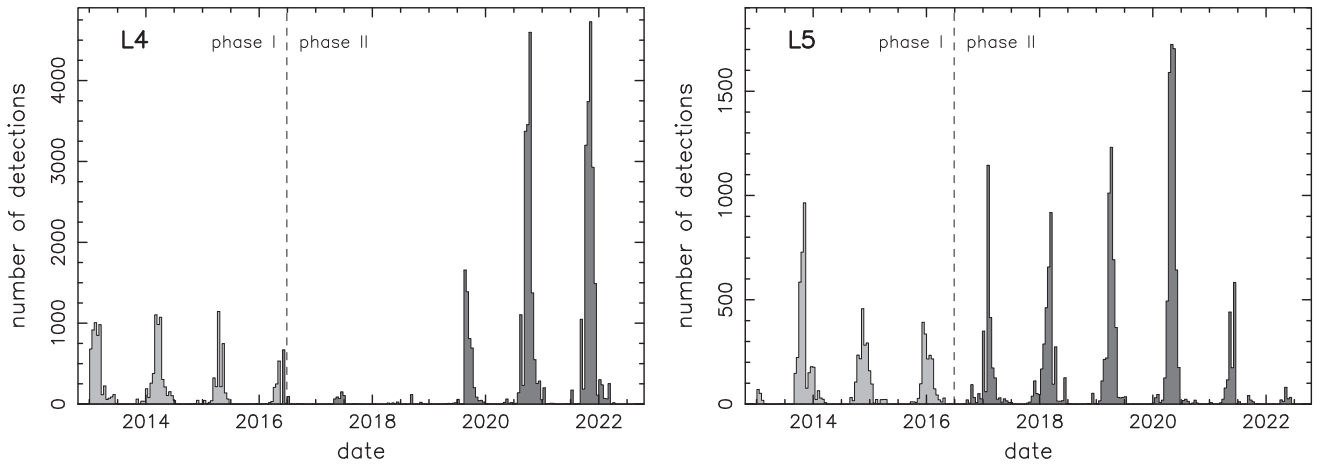
Figure 4. Number of Trojan detections throughout the CSS operations in phases I and II: left for L4 cloud, right for L5 cloud. Apart from the obvious annual variation, due to the Earth's revolution about the Sun changing the viewing geometry of the Trojan clouds at the night sky, there is also a longer-term variation due to Jupiter's motion. This dictates when a particular cloud, L4 or L5, appears projected in the direction of the galactic plane. For instance, the major minimum of L4 object detection around 2018 is when the cloud overlaps with the galactic center direction. Finally, data during the phase II operations of CSS are roughly 4 times more numerous than during phase I operations due to a 4 times larger field of view.
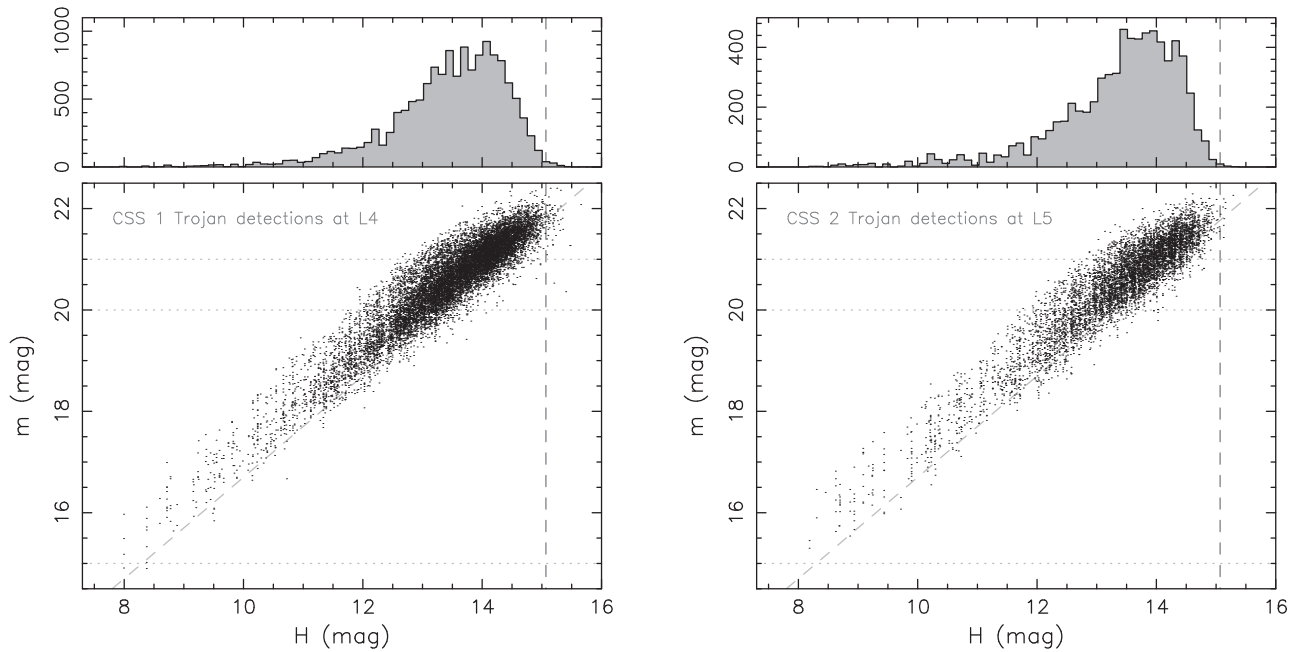

Figure 5. Upper panel: histogram of the absolute magnitude H values for detections of L4 (left) and L5 (right) Trojans during the CSS phase I operations (the ordinate is the number of such detections within the bin). The vertical dashed line shows the magnitude at the center of a bin in which the number of detections dropped below 5% of the bin with a maximum number of detections. This value is about $\simeq 15.1$ for both L4 and L5 clouds. Bottom panel: correlation between the absolute magnitude H at the abscissa and visual magnitude m at the ordinate for detections of L4 (left) and L5 (right) Trojans during the CSS phase I operations. At an ideal opposition, $m - H \simeq 6.7$ (neglecting the phase function correction) from simple distance arguments (the dashed line). The nearly 2 mag spread toward larger m values are detections at different phase angles. The dotted lines between visual magnitudes 20 and 21 indicate a typical 50% photometric efficiency of detections. Objects brighter than $m \simeq 15$ (lower dotted line) may saturate exposures and be undetected due to their slow motion. Luckily, there are detection losses due to this effect for Trojan populations because even the largest of them at opposition barely reach this limit. The only photometric limit, indicated by the vertical dashed line from the upper panel, thus occurs at the faint end of the spectrum.

population members are faint enough that saturation and confusion with stationary objects do not occur. Obviously, a given telescope/detector configuration will always suffer from limitations at the faint end.

For CSS operations, the characteristic 50% detection efficiency ranges between 20 and 21 apparent visual magnitude (depending on the night conditions). Neglecting the phase function correction, we may roughly estimate the corresponding absolute magnitude limit using Pogson's relation

$m - H \simeq 5 \log(r\Delta)$, where $r \simeq 5.2$ au and $\Delta \simeq 4.2$ au are heliocentric and geocentric distances at opposition. This provides $m - H \simeq 6.7$, shown by the dashed line in Figures 5 and 6. Trojans having magnitudes up to $H \simeq 14$ should thus be reached by CSS with a still fairly well-characterized detection efficiency, but this may also apply to bodies that are a magnitude fainter. The rough estimate of Trojan population completeness near this H value is also supported by the fact that no new object with $H \leqslant 14.2$–14.3 was discovered within
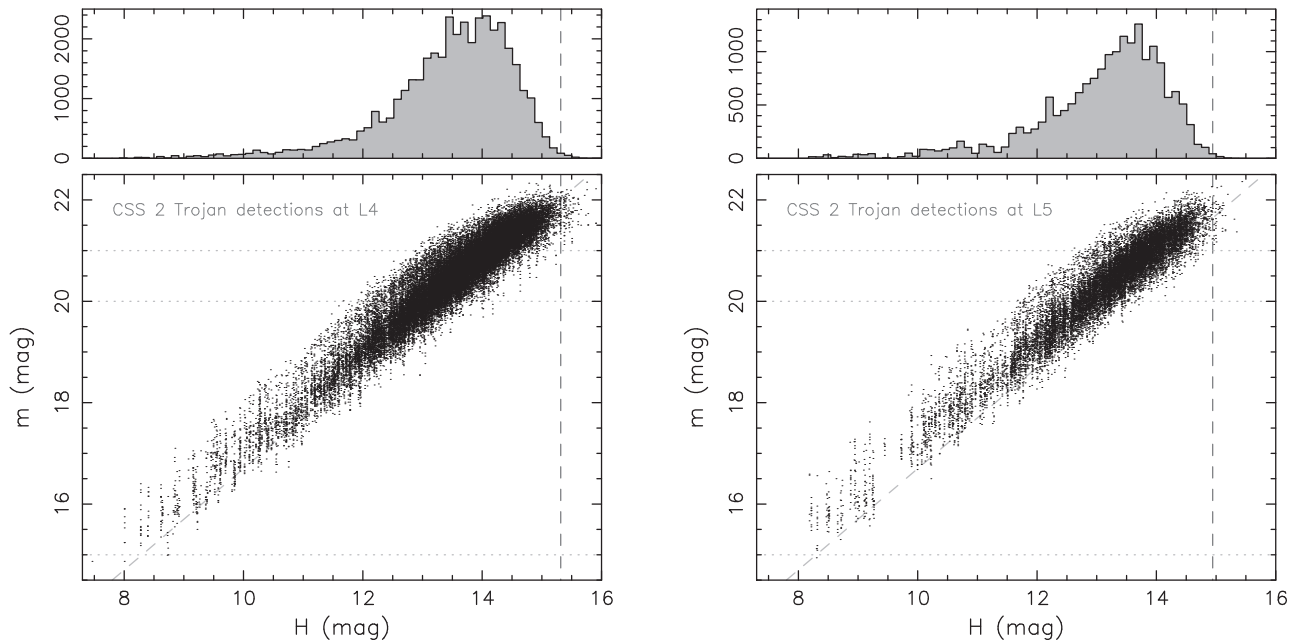
Figure 6. The same as in Figure 5, but now for the CSS phase II operations containing roughly 3 times more detections. The vertical dashed lines are now different for the two Trojan clouds: $\simeq 15.35$ for L4 and $\simeq 14.95$ for L5.

the past five years (see Hendler & Malhotra 2020, who give $H \simeq 13.8–13.9$ as a completeness limit for JTs).

A comparison of the two panels in Figure 6 indicates an interesting (and important) difference between G96 observations of the L4 versus L5 Trojans: the L4 detections sample the population about $\simeq 0.35$ mag deeper in terms of absolute magnitude compared to the L5 detections (see the dashed vertical lines). This is a result of yet another bias. During phase II of the CSS operations, Jupiter moved on its elliptic orbit between the mean anomaly $\simeq 160°$ at the beginning to $\simeq 310°$ at the end. On average, the L4 Trojans were thus at smaller heliocentric and geocentric distances. Given the constant detection limit of G96 in terms of the apparent magnitude, the survey was able to reach slightly smaller L4 Trojans compared to L5 Trojans.

Some more illustrations of the selection effects in the CSS observations are provided in Appendix B, where we also conduct a test justifying our simplifying assumptions about the detection probability function. The fundamental issue of how to map the above-mentioned selection effects and the detection probability on the CSS images to the detection probability in the parameter space of the observed population of JTs is postponed to Section 4.1.

3. Orbital Architecture and Magnitude Distribution of the Trojan Population

3.1. Simple Parameterization for Model Fitting

Several previous studies have attempted to debias the Trojan observations, with the goal being to determine the complete population down to some size or absolute magnitude. The orbital distribution properties of the Trojans were most often characterized by observer-related parameters, namely by the distribution of the heliocentric ecliptic longitude and latitude relative to Jupiter or the corresponding libration center. Typically, simple double-Gaussian distributions were adopted (e.g., Szabó et al. 2007; Wong & Brown 2015, and others).

Some studies, see Jewitt et al. (2000), attempted to go beyond this approach by introducing a very simple approximation of the orbital inclination distribution.

Here we intend to describe the orbital architecture of the Trojan population in greater detail than previous attempts, namely with the most relevant orbital parameters. This description will be more complete, and we will also attempt to discern the background population from the populations in major families (such as Eurybates or Ennomos). This removal is needed to describe the putative asymmetry in the L4 and L5 populations.

3.1.1. Orbital Distribution

Orbital elements of a different level of sophistication were developed by both analytical and numerical methods. Here, we do not need to work with precise parameters whose stability will last over very long timescales. Rather, we need parameters that are basically osculating at an epoch close to the decade of CSS observations (the close link to the osculating elements will make them easy to implement in the debiasing methods; Section 4.1), and which capture the basic features of Jupiter's perturbations. With that in mind, here is our choice (we note that Vinogradova (2015) and Vinogradova (2019) used variables e_p and I_p similar to ours A and B to search for principal Trojan families).

Orbital Inclination. We link the heliocentric orbital inclination I and longitude of node Ω together into a complex variable ζ, such that ($\iota = \sqrt{-1}$)

$$\zeta = \sin I \exp(\iota\Omega) = \zeta_J + A \exp(\iota\varphi), \tag{1}$$

where ζ_J is the same variable for Jupiter orbit. The second term on the right-hand side of (1) describes the orbit free of the main Jupiter perturbing effect; namely, the amplitude A crudely represents what would be the proper sine of inclination.

Orbital eccentricity. Next, we link the heliocentric eccentricity e and longitude of perihelion ϖ together into a complex
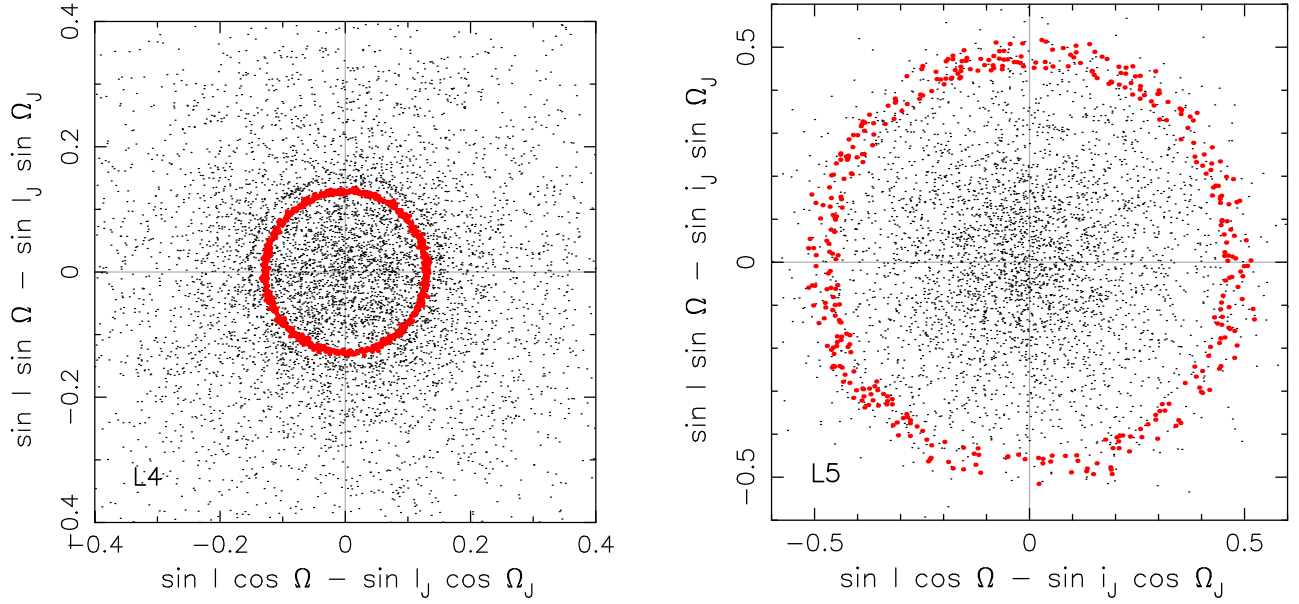
Figure 7. Cartesian representation of $\zeta - \zeta_J$ for 7903 L4 Trojans (left) and 4177 L5 Trojans (right) from the MPC catalog as of 2023 February (using osculating elements at MJD 60,000). The red symbols show the major families in the respective Trojan clouds: Eurybates at L4 and Ennomos/Deiphobus at L5, using their identifications in Appendix A. At the zero level, the population distribution is independent of the polar angle φ in these coordinates, depending only on the radial coordinate A (see Equation (1)).

variable z, such that

$$z = e \exp(\iota(\varpi - \varpi_J)) = e_J \exp(\pm\iota\pi/3) + B \exp(\iota\psi), \quad (2)$$

where e_J and ϖ_J are the respective variables for Jupiter orbit. As above, the amplitude B of the second term on the right-hand side here crudely represents what would be the proper eccentricity (see, e.g., Bien & Schubart 1987; Li et al. 2021).

Orbital semimajor axis and longitude in orbit. Sicardy & Dubois (2003), see already Yoder et al. (1983), and Morais (1999, 2001) developed the simplest but very useful representation of the resonant motion of Jupiter's Trojans. Averaging the perturbing Hamiltonian over periods of Jupiter's heliocentric revolution and shorter, they further neglected orbital eccentricity and inclination terms and showed that Trojan libration near L4 and L5 equilibria has an integral of motion

$$\left(\frac{da}{a_J}\right)^2 = \frac{8\mu}{3}[C - f(\sigma)], \quad (3)$$

where

$$f(\sigma) = \frac{1 + 4|\sin\sigma/2|^3}{2|\sin\sigma/2|}, \quad (4)$$

with $\sigma = \lambda - \lambda_J$, $da = a - a_J$ ($a_J \simeq 5.206$ au), and $\mu = m_J/(m_\odot + m_J)$. The value of the integration constant C satisfies $C \in (C_{min}, C_{max})$, where for tadpole orbits $C_{min} = 1.5$ and $C_{max} = 2.5$. Equation (3) expresses, at the zero level, the resonant correlation between the involved orbital elements, namely the semimajor axis a and the longitude in orbit λ (the neglected terms are proportional to e^2 and I^2). As above, the parameter C crudely represents the proper semimajor axis da_P, such that $da_P \simeq a_J\sqrt{8\mu\,\Delta C/3}$, where $\Delta C = C - C_{min}$ is the excess of C over its minimum value $C_{min} = 1.5$.

Assumed background orbital distribution of the Jupiter Trojans. The currently known population of JTs in L4 and L5

clouds is shown using the above-described variables in Figures 7, 8, and 9. Obviously, this is the observationally biased population. In order to characterize the complete (biased-corrected) population, we need to describe it using a relatively simple functional form. Its free parameters will be adjusted in the process of (i) turning the complete synthetic population into the biased synthetic population (applying the CSS biases), and (ii) comparison of the latter with the observations.

Let us start with the background population. A quick look at Figures 7 and 8 reveals that the Trojan distribution density is basically independent of the phase angles φ and ψ defined in Equations (1) and (2). Rather, it only depends on the respective radial coordinates A and B. Similarly, the Trojan distribution density in the $(da, \sigma = \lambda - \lambda_J)$ plane (Figure 9) basically depends on the C parameter, being homogeneous within a given $(C, C + dC)$ bin (this is because the principal orbital shear occurs within the bin, and possibly across neighboring bins only). Therefore, at the zero approximation, we may represent the orbital architecture of the Trojan clouds at L4 and L5 using the distribution function depending on the A, B, and C parameters only. Additionally, to keep things simple, we neglect correlations between these parameters such that the orbital distribution function $dN_{back}(A, B, C)$, specifying the number of Trojans in the bin $(A, A + dA; B, B + dB; C, C + dC)$, may be split into independent contributions

$$dN_{back}(A, B, C) = dN_{back}(A)dN_{back}(B)dN_{back}(C). \quad (5)$$

The observed, albeit biased, population hints the possible functional form:

$$\frac{dN_{back}(A)}{dA} \propto A^{\alpha_1} \exp\left[-\frac{1}{2}\left(\frac{A}{s_A}\right)^{\alpha_2}\right], \quad (6)$$

$$\frac{dN_{back}(B)}{dB} \propto B^{\beta_1} \exp\left[-\frac{1}{2}\left(\frac{B}{s_B}\right)^{\beta_2}\right], \quad (7)$$
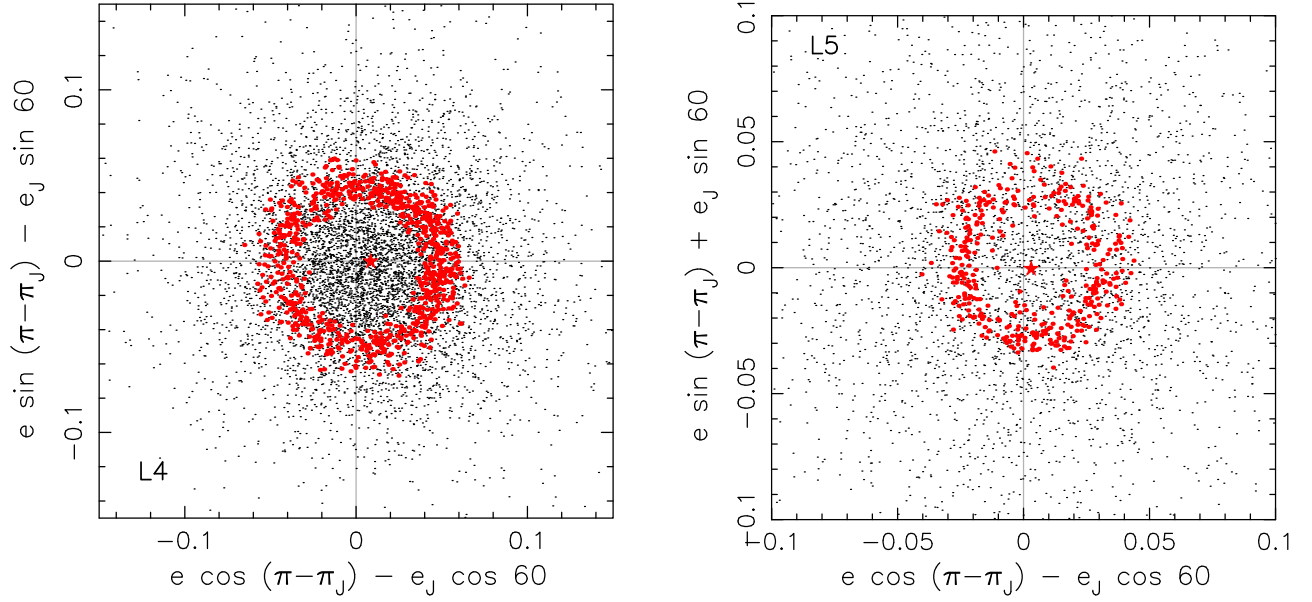
Figure 8. Cartesian representation of $z - e_J \exp(\pm \imath \pi/3)$ for 7903 L4 Trojans (left) and 4177 L5 Trojans (right) from the MPC catalog as of 2023 February (using osculating elements at MJD 60,000). The red symbols show the major families in the respective Trojan clouds: Eurybates at L4 and Ennomos/Deiphobus at L5, using their identifications in Appendix A. At the zero level, the population distribution is independent of the polar angle ψ in these coordinates, depending only on the radial coordinate B (see Equation (2)).
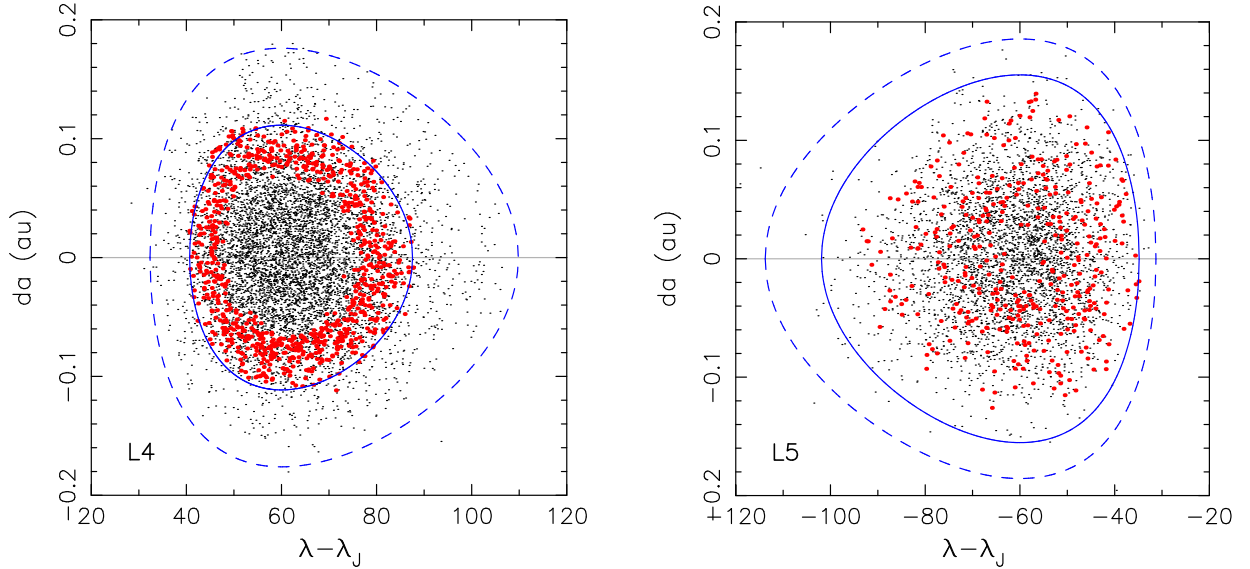
Figure 9. Projection of the MPC Trojan clouds as of 2023 February onto the $\lambda - \lambda_J$ (abscissa) and $da = a - a_J$ (ordinate) plane (using osculating elements at MJD 60,000, and $a_J = 5.204$ au). The left panel is for L4, and the right panel is for L5. Red symbols among the L4 population highlight the Eurybates family members, those among the L5 population show the more dispersed Ennomos/Deiphobus family members. The blue lines are the isolines of the first integral of the Trojan motion Equation (3) for selected values of the C parameter: (i) $C = 1.68$ (solid) and $C = 1.95$ (dashed) in the L4 panel, and (ii) $C = 1.88$ (solid) and $C = 2$ (dashed) in the L5 panel. In spite of its huge simplicity, representation using Equation (3) helps to parameterize the population for our purposes.

and

$$\frac{dN_{\mathrm{back}}(C)}{dC} \propto \exp\left[-\frac{1}{2}\left(\frac{C - C_{\min}}{s_C} \right)^{\gamma} \right], \qquad (8)$$

may hold for the background population (Figure 10), over which the contribution of significant families are linearly superimposed (their distribution is simpler, because we assume the families uniformly occupy a very limited interval—possibly a single bin—in A, B, and C proper elements; see below). The fair match of the biased population justifies the use of

Equations (6), (7), and (8) also for the complete (debiased) populations near L4 and L5. Note, however, that this is a particular operational choice of our model, which could be reassessed or improved in future studies. Obviously, the parameters (such as α, β, γ, s_A, s_B, s_C) are to be considered as solved-for quantities along with the debiasing procedure (Section 5). Note that the absolute normalization of the population is to be set by the absolute magnitude distribution modeling discussed in Section 4.

Returning to the Trojan families issue, we note that especially the leftmost panel in Figure 10 (showing the
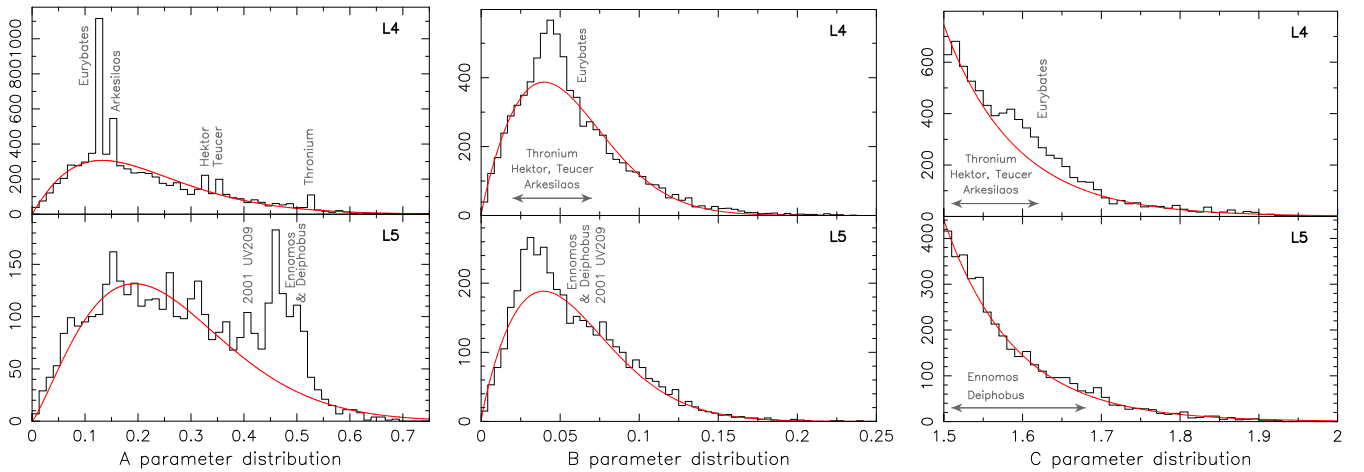
Figure 10. The observed population of Jupiter Trojans in the MPC catalog as of 2023 February represented using the distribution of the A, B, and C orbital parameters: L4 cloud on top, L5 cloud at the bottom. As to their definition, see Equations (1), (2), and (3). The red lines are approximate fits of the background population using the simple few-parametric functions in Equations (6), (7), and (8), avoiding the contribution of the major families. In particular, we used: $\alpha_1 = 1$, $\alpha_2 = 1.3$ and $s_A = 0.095$ for the inclination distribution, $\beta_1 = 0.87$, $\beta_2 = 1.75$ and $s_B = 0.04$ for the eccentricity distribution, and $\gamma = 1$ and $s_C = 0.045$ in the L4 population, and $\alpha_1 = 1.2$, $\alpha_2 = 1.6$ and $s_A = 0.15$ for the inclination distribution, $\beta_1 = 0.85$, $\beta_2 = 1.6$ and $s_B = 0.038$ for the eccentricity distribution, and $\gamma = 1$ and $s_C = 0.045$ in the L5 population. The most prominent Trojan families contribute to the total population with specific values of the proper elements. As usual, they are most noticeable in the inclination distribution (left panel; the Thronium family was formerly called 1996 RJ). The population in Eurybates family accounts for more than 10% of the observed population in L4. The Ennomos/Deiphobus clan (see the Appendix) may represent a slightly smaller share among the L5 Trojans.

inclination distribution) is a very useful tool to judge, in a preliminary manner, their potential role. For instance, we could straightforwardly estimate the population of the most outstanding Eurybates family in the L4 swarm to be $\simeq 850$ members (this is the level by which it surpasses the smooth background in its local A bin). Indeed, a more sophisticated clustering identification of the Eurybates family in the 3D space of the proper orbital elements (see Appendix A, Table 4) reveals a population of 875 currently known members. This represents $\simeq 11\%$ of the whole L4 swarm. Adding more than 300 members to the Hektor and Arkesilaos families, the fraction in L4 families increases to $\simeq 15\%$, and our analysis of the magnitude distribution of the background population and individual families below shows that this fraction increases for fainter Trojans. The family share of the net population seems to be slightly smaller in the L5 swarm, with Ennomos/Deiphobus representing the only standout clan (see Appendix A). Its population reaches about 10% of the total.

The stability zone and the A–B–C correlations. The above-mentioned simple solution of the libration about the stationary points L4 or L5 of the 1:1 mean–motion resonance with Jupiter (Equation (3)) neglects eccentricity and inclination terms. Therefore, our description misses coupling between the libration amplitude or C, eccentricity B, and inclination A. One may, however, impose such effects after the fact either from theoretical considerations or from estimates based on numerical simulation and/or data.

In the first step, we represented the known population of JTs using 2D projections in the space of these parameters, namely (C, A), (C, B), and (A, B) in Figure 11. As expected (see Rabe 1965, 1967; Levison et al. 1997), the strongest correlation concerns C versus B: larger B (eccentricity) values require smaller C (libration amplitude) values. That helps to avoid close approaches to Jupiter. The gray line in the middle panels of Figure 11 is a zero-order estimate of the stability limit. There is a weaker effect in the inclination too, but this element is constrained by a maximum value of $\simeq 43°$; this is likely related to the perturbing effects of several secular resonances (such as

s_7 and s_8, or even resonances in which secular frequencies are combined with that of the great inequality; see Marzari et al. 2003; Robutel & Gabern 2006).

In the second step, we characterize the stable zone of JTs in a more sophisticated way, namely using a direct numerical experiment. This work allows us to determine the portion of the (A, B, C) parameter space where Trojan orbits are long-term stable. This result will allow us to determine the complete Trojan population discussed in Section 4.

We parsed the (C, B) plane with limiting values shown in the middle panel of Figure 11 into rectangular bins with width $\Delta B = 0.01$ and $\Delta C = 0.015$, altogether 1040 such cells. We considered 28 variant orbits starting in each of the cells, assigning them seven distinct but fixed values of the A parameter (corresponding to the orbital inclination). In order to set up initial orbital elements, we complemented (A, B, C) values with three angles (φ, ψ, θ), introduced in Section 4.1, randomly sampling intervals $(0°, 360°)$.

We numerically propagated this set of synthetic orbits, starting in the libration zone about both the L4 and L5 stationary points, with the Sun and giant planets for 100 Myr forward in time (the initial epoch was MJD 60,000.0). Because the terrestrial planets were neglected, we performed the barycentric correction to state vectors of all integrated bodies (massive planets and massless Trojans). This means (i) we added masses of all terrestrial planets to the center (the Sun), and (ii) shifted the Sun to the barycenter of the inner Solar system. We used the well-tested and efficient package `swift` (specifically `swift_rmvs4` code) for our simulation and used a short timestep of 0.25 yr. During the propagation, we monitored the heliocentric orbits of the test bodies as to their residence in the respective libration zones about the L4 and L5 points and eliminated those that escaped from their initial regions. At the end of the simulation, we evaluated the statistics of the particle orbital histories and projected them onto their starting bins in the (C, B) plane.

The results are shown in Figures 12 and 13. As expected, the stable region has a triangular shape populated by the observed
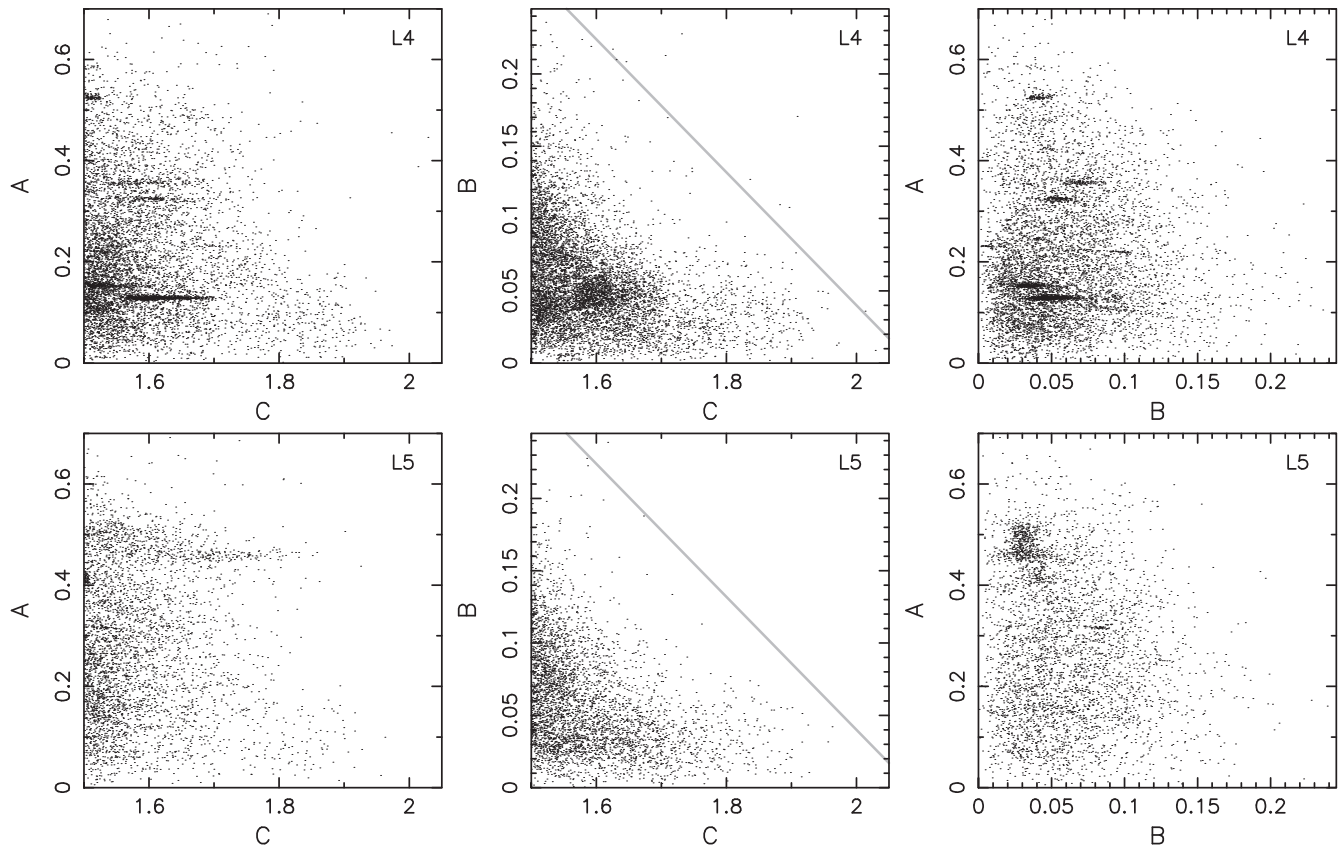
Figure 11. The observed population of Jupiter Trojans in the MPC catalog as of 2023 February represented by 2D projections in the A, B, and C orbital parameters: (i) A vs. C (left), (ii) B vs. C (middle), and (iii) A vs. B (right). The top panels are for the L4 cloud, and the bottom panels are for the L5 cloud. Two distinct features are worth noting: (i) correlation between C and B in the middle panels (such that larger B requires smaller C), which is the expression of orbital stability constraint, and (ii) orbital clusters, most distinctly seen in the A vs. B plane in the right panels (see also Figure 9 in Vinogradova 2015, 2019). The gray line in the middle panels approximates the stability limit (we improve this guess by a direct numerical experiment in Figures 12 and 13). The latter are the Trojan families, collections of fragments from the collisional disruption of parent bodies. Curiously, the L4 cloud shows clear evidence of nine families, starting with the best-known Eurybates case (e.g., Brož & Rozehnal 2011; Rozehnal et al. 2016; Marschall et al. 2022). The families in L5, while also existing, seem to be blurred by either higher ejection velocities, dynamical diffusion at their particular location, or some other effect.

Trojans. The region of stability first slightly increases with increasing A, but then shrinks when A becomes large. We note that the integrated timespan of 100 Myr is rather short, and extending it to Gyr would lead to additional collapse of the stability zone (e.g., Levison et al. 1997; Robutel & Gabern 2006). A small fraction of the observed Trojans (blue symbols in Figures 12 and 13) fall into the unstable bins. This outcome is in agreement with the known marginal stability of the Trojan swarms, filling the available dynamical zone around the L4 and L5 stationary points to its "full capacity" (see, e.g., Milani 1993; Levison et al. 1997; Holt et al. 2020b). The resolution given by our large bins is too poor to identify the very fine secular resonant features discussed by Robutel & Gabern (2006; though some structures on the stability border-line at the top panels of Figures 12 and 13 might be traced to these effects). Finding this behavior, however, was not the primary motivation of our experiment. Instead, we aimed at the zero-order definition of the phase space zone available for the stable Trojan orbits. This information will be used in Section 4 for a definition of the orbital zone in the (A, B, C) space of variables over which we shall debias the Trojan population.

Figure 14 shows a comparison of the stability limit of the Trojan orbits identified in our numerical experiments for several values of the proper inclination parameter A. We specifically compare the limiting curves for L4 and L5 libration

zones, using a "mirror representation" in the upper and lower panels. There are no statistically meaningful differences, implying that the orbital stability of the L4 and L5 regions is the same. Obviously, this is not a novel result but rather a confirmation of what has been known previously (e.g., Marzari et al. 2003; Di Sisto et al. 2014; Hou et al. 2014). This symmetry stems from the stationary configuration of planetary orbits, Jupiter in particular. It would be broken if the planets were to migrate (e.g., Sicardy & Dubois 2003; Hou et al. 2016; Pirani et al. 2019a; Li et al. 2023b).

Assumed orbital distribution of the Jupiter Trojans in families. Several statistically reliable Trojan families have been identified in the Trojan population (see, e.g., Nesvorný et al. 2015, and references therein). Since the latest publicly available identification of the Trojan families dates back to the 2015 release of the catalog at the PDS node (with some additional data available from Vinogradova 2015; Rozehnal et al. 2016; Holt et al. 2020b; Vinogradova 2020), we decided to take the "bull by the horns" and update this information. Our work was motivated by the rapid increase of the known Trojan population and a need to separate the family members from the background as much as possible in this work. To that end, we (i) determined a new set of Trojan proper elements using methods described in Appendix A of Holt et al. (2020a) and applied them to the currently known population of Trojans, and
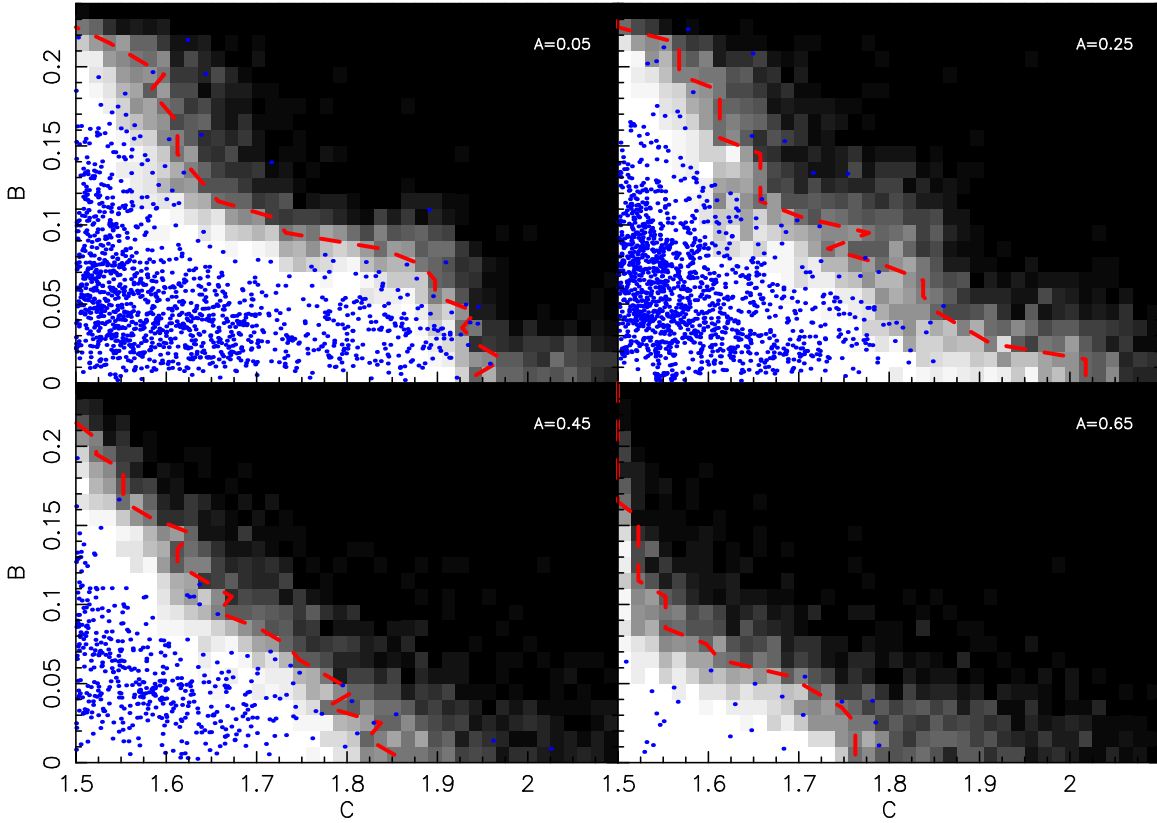
Figure 12. Results of a numerical experiment probing stability of Trojan orbits in the L4 cloud. Orbits of 28 clone variants were started in different bins in the C vs. B plane (i.e., librations amplitude vs. eccentricity), with four different fixed values of A (i.e., inclination) given by the label. Residence in the libration zone about the L4 stationary point was monitored throughout the simulation, reaching 100 Myr period of time. All orbits in the white cells are stable, and all orbits in the black cells are unstable (i.e., escaped from the Trojan region within the integration). The gray bins were found partially stable, and the scale of grayness is linearly proportional to the number of clone orbits that escaped. The stability limit is shown by the red dashed line connecting the first bins with 50% partial instability for the given B value. The blue symbols show the known Trojan population within the ± 0.05 value of A referred to as the nominal value.

(ii) identified principal families in the population. Results are briefly summarized in Appendix A.

In spite of having this new set of proper elements available to us, we opted to continue using the simplified variables introduced above for the population analysis in this paper. The reason is that they have a more straightforward connection to the osculating orbital elements (a step that would be more complicated for the proper elements), and this facilitates the determination of the detection probability of CSS discussed in Section 4.1. We thus use the families identified in the space of proper elements and locate them in the space of parameters A, B, and C.[5] Note that this step is only approximate and may potentially lead to some inaccuracies, mainly because the families are identified in the proper element space as a collection of individual Trojans. We now need to represent each of the families by a continuous distribution function

$$dN_{\mathrm{fam}}(A, B, C) = dN_{\mathrm{fam}}(A)\,dN_{\mathrm{fam}}(B)\,dN_{\mathrm{fam}}(C). \quad (9)$$

By itself, the function tells us "where the family is located," but does not exclude presence of possible interloping (background) Trojans in the same zone as well. Therefore $dN_{\mathrm{fam}}(A, B, C)$ should have a nonzero value in a correctly tuned region: (i) not too large (as this would imply too many interlopers are included), and (ii) not too small (which would mean we

<hr>

[5] We note that Vinogradova (2015) and Vinogradova (2019) used variables similar to our A and B to search for Trojan families in the restricted 2D space.

undershot the contribution of families). There are only approximate solutions between the two limits.

We experimented with different representations of $dN_{\mathrm{fam}}(A, B, C)$, starting with simple boxcar functions delimiting the corresponding parameter in a certain interval of values, such as $dN_{\mathrm{fam}}(A) \propto (H[A - A_{\mathrm{min}}] - H[A - A_{\mathrm{max}}])\,dA$, where $H[x]$ is the Heaviside function and $(A_{\mathrm{min}}, A_{\mathrm{max}})$ the corresponding interval of A values. However, tests indicated this definition would often wrap many interloping objects from the background populations that are unrelated to a given family. A tighter representation was educated by a distribution of the known members in the families, as identified in the space of proper orbital elements. We used
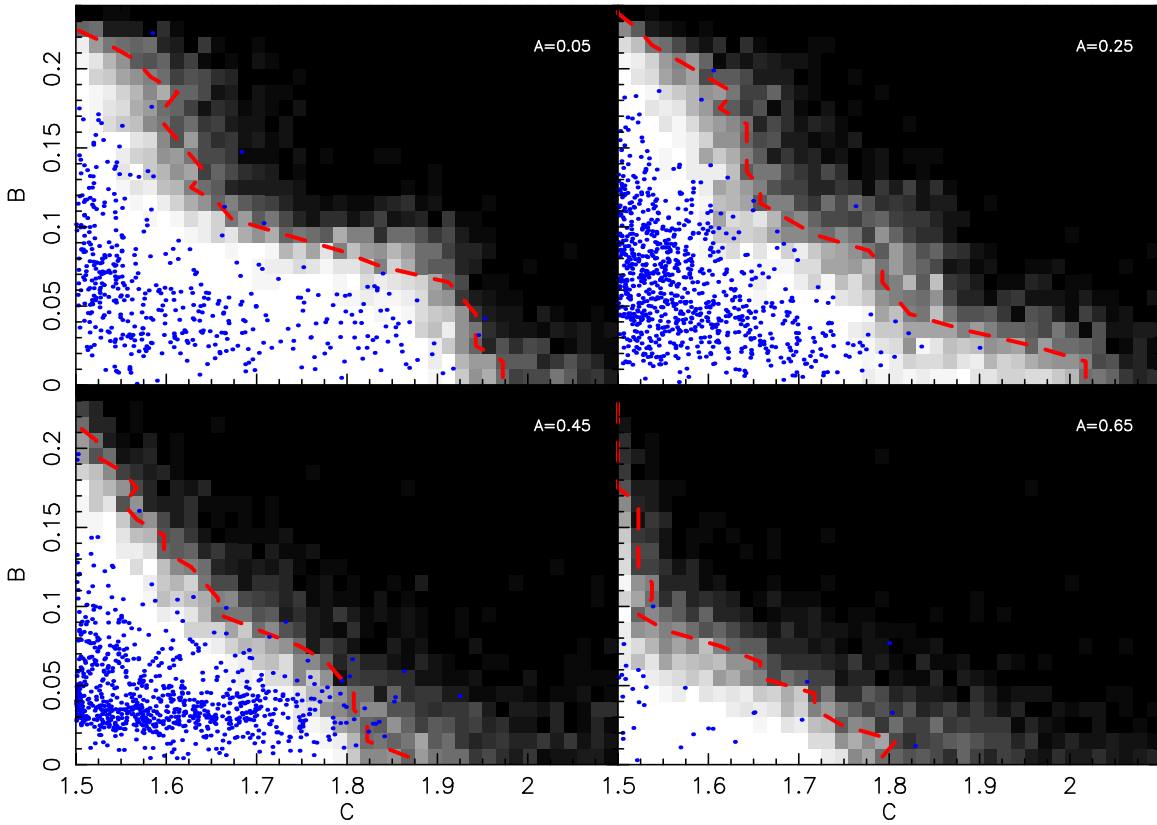
$$\frac{dN_{\mathrm{fam}}(A)}{dA} \propto \exp\left[-\frac{1}{2}\left(\frac{A - A_{\mathrm{ref}}}{s_A^{\mathrm{F}}}\right)^{\alpha^{\mathrm{F}}}\right], \quad (10)$$

$$\frac{dN_{\mathrm{fam}}(B)}{dB} \propto \exp\left[-\frac{1}{2}\left(\frac{B - B_{\mathrm{ref}}}{s_B^{\mathrm{F}}}\right)^{\beta^{\mathrm{F}}}\right], \quad (11)$$

and

$$\frac{dN_{\mathrm{fam}}(C)}{dC} \propto (C - C_{\mathrm{ref}})^{\gamma_1^{\mathrm{F}}} \exp\left[-\frac{1}{2}\left(\frac{C - C_{\mathrm{ref}}}{s_C^{\mathrm{F}}}\right)^{\gamma_2^{\mathrm{F}}}\right]. \quad (12)$$

Figure 13. The same is in Figure 12, but now for the L5 Trojan population.

Coefficients $(A_{ref}, s_A^F, \alpha^F; B_{ref}, s_B^F, \beta^F; C_{ref}, s_C^F, \gamma_1^F, \gamma_2^F)$ were determined from distribution of the identified (although biased) population in the family. They were fixed and not subject to further refinement when the complete Trojan population was determined in Section 5. Their values for the families considered are given in Table 1.

3.1.2. Magnitude Distribution

Apart from the orbital distribution of Trojans in their respective clouds described above, their absolute magnitude H distribution is the second quantity of major interest here. In differential form, we denote $dN(H)$ as the number of Trojans in the bin $(H, H + dH)$. We assume the orbital and magnitude distributions are decoupled. The reason is that collisional communication within one Trojan cloud (L4 and/or L5) is large enough that everything hits everything else, making the magnitude distribution in each orbital bin equal. As a result, the differential form $dN(A, B, C; H)$ of the Trojan distribution in the orbital and magnitude space, specifying the complete Trojan population in a bin $(A, A + dA; B, B + dB; C, C + dC; H, H + dH)$, may be written as

$$dN_{model}(A, B, C; H) = dN(A, B, C)dN(H), \qquad (13)$$

with $dN(A, B, C)$ from either Equation (5) or (9). This means we distinguish the background population and the population in major Trojan families, which linearly superpose to the total population

$$\begin{aligned} dN_{model}(A, B, C; H) = {} & dN_{back}(A, B, C; H) \\ & + dN_{fam}(A, B, C; H). \end{aligned} \qquad (14)$$

Each term on the right-hand side again breaks independently to the orbital and magnitude parts as in Equation (13). Next, we describe the assumed functional form of the magnitude terms.

Background population. Traditionally, the Trojan magnitude distribution has been represented using a broken power law with a steeper leg (characterized by an exponent α_1) below a break at magnitude H_b and a shallower slope (characterized by an exponent α_2) above, such that[6] (see, e.g., Jewitt et al. 2000; Wong et al. 2014; Wong & Brown 2015)

$$dN_{back}(H) = 10^{\alpha_1(H-H_0)} dH \qquad \text{for } H < H_b, \quad (15)$$

$$dN_{back}(H) = 10^{\alpha_2 H + (\alpha_1 - \alpha_2)H_b - \alpha_1 H_0} dH \quad \text{for } H > H_b. \quad (16)$$

There are four independent parameters in this model, three of which (H_b, α_1, α_2) characterize the shape of the magnitude distribution, and H_0 sets the absolute normalization (see Figures 15 and 16). Two more parameters are to be added when a second break at a few kilometers in size has been identified beyond magnitude $H_{b2} \simeq 15$ (Wong & Brown 2015); for $H > H_{b2}$ the magnitude distribution becomes even shallower (likely because the population has experienced 4.5 Gyr of collisional grinding, e.g., Marschall et al. 2022; Bottke et al. 2023). Further studies obtained slightly different values, shifting the second break point down to

---

[6] Yet another, more complicated model would divide the background population into two subpopulations, namely the spectrally "very red" and "red" groups (Wong & Brown 2015). As shown by these authors, both have different magnitude distributions. We do not pursue this interesting pathway in this paper because we do not use color data in the optimization procedure. However, our ability to include the most prominent Trojan families, which distinctly show in the orbital element space, partly substitutes the missing "red" population that Wong & Brown (2015) attribute to collisional fragments
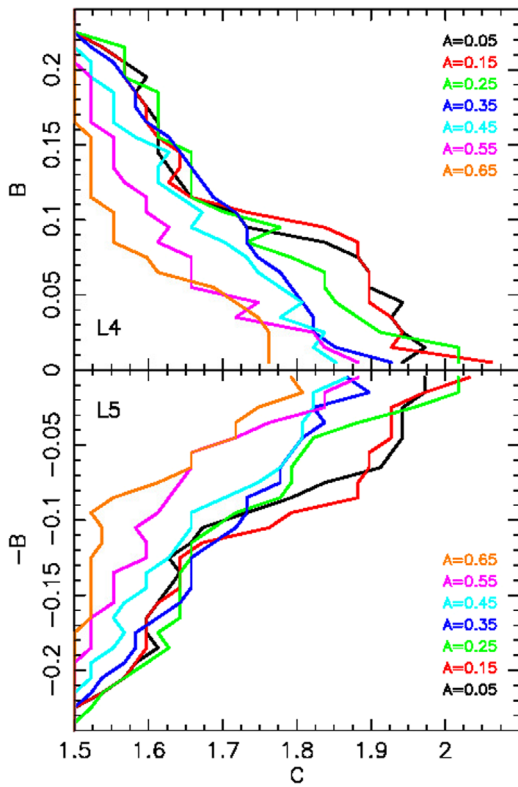
Figure 14. Comparison of the stability limits for Trojan orbits in the C vs. B plane determined by our numerical experiment spanning 100 Myr. Different curves for seven different values of A are labeled and identified by color. The upper panel is for L4 Trojans, and the bottom panel is for L5 Trojans; for the sake of comparison, we transformed $B \rightarrow -B$ in this panel. There is no difference in the orbital stability for L4 and L5 clouds (see also Robutel & Gabern 2006; Di Sisto et al. 2014).

$H_{b2} \simeq 13.6$ (Yoshida & Terai 2017; Uehata et al. 2022), but the changes in the slope are quite subtle. Apriori, the 1.5 m aperture of the CSS/G96 telescope at Mt. Lemmon cannot rival the results of Subaru-scale telescopes in reaching very faint Trojans (see Figures 5 and 6). As a consequence, our ability to accurately determine the location of this second break point and the magnitude distribution properties just below and beyond it is limited. At best, we could eliminate implausibly low values of H_{b2} (see Section 5).

Given the significantly larger number of known Trojans today, and the level of detail at which we want to describe their population, we considered an analytical description of $dN_{back}(H)$, such as given in Equations (15) and (16), would be too rigid. Instead, we used a more flexible approach introduced to study the magnitude distribution of the near-Earth population by Nesvorný et al. (2023, 2024). In particular, we represent the cumulative magnitude distribution $\log_{10} N_{back}(<H)$ using cubic splines in the interval $7 < H < 15$ in the initial analysis, extending to a larger interval $7 < H < 15.5$ in further tests: (i) there are no Trojans with $H < 7$ (the largest being 624 Hektor with MPC $H = 7.45$), and (ii) there are too few G96 detections beyond magnitude 15.5, such that no reliable results may be obtained for a population of these faintest objects from the data we have. In practice, we split this interval into a certain number of segments. In each of those, we consider a mean slope parameter to be a free parameter (for n segments, this implies n independent slopes to be fitted). Additionally, we add $(n+1)$-th parameter representing the absolute normalization $N_{back}(<H_r)$ of the population at a certain

reference magnitude H_r; we use $H_r = 14.5$. There are no additional parameters to be fitted, since the solution for $\log_{10} N(<H)$ is then fixed by enforcing continuity (including the first derivative) at the segment boundaries. After a brief phase of experimenting with the model, we set up six segments, implying seven free parameters in the initial analysis. Comparing the degrees of freedom in our approach to the traditional method, we find that our work does not overparameterize the problem, yet it does gain a significant benefit in generality.

In Section 5.2 we find support for statistically robust features of the magnitude distribution, which cannot be described by the simple broken power-law model. In addition to this aspect, we point out a conceptual issue. The piecewise spline approximation is in fact very close to piecewise power law, with different power slopes in different segments, but splines connect different slopes smoothly (i.e., without discontinuities, including the derivatives). This conforms to the real size distributions, which are continuous and smooth. On the other hand, the broken power-law approach violates the natural smoothness requirement.

Population in families. Similar to the situation in the asteroid belt, studies of Trojan families (clusters of fragments all related to the disruption of a parent body) flourished when a large population of Trojans were known, and accurate proper elements became available (see the pioneering works of Milani 1993; Beaugé & Roig 2001). As the number of Trojans has rapidly increased over the past decade or so, the potential of reliably identifying families in the Trojan population has increased (see, e.g., Brož & Rozehnal 2011; Rozehnal et al. 2016). This advance has also motivated a number of photometric and spectroscopic studies focused on family members, with the goal of seeking possible differences with respect to the background Trojan population.

In our simple description of the Trojan orbits, the principal families are most easily discerned in inclination (Figures 7, 10, and 11). The left panel in Figure 10 clearly demonstrates that families represent a surplus over the background population that may account for as much as $10-15\%$ of the whole population. In order to compare the background populations in the L4 and L5 clouds, we need to treat the families as separate populations.

Several studies (see Rozehnal et al. 2016, and our Appendix for the most recent updates) indicate that (i) the magnitude distribution of the family members is steeper than the background population in the $H \simeq 12-15$ range (e.g., Figure 16), and (ii) except for the few largest members it can be reasonably approximated by a single power law

$$dN_{fam}(H) \simeq 10^{\beta_1(H-H_0)} \, dH. \qquad (17)$$

For instance, approximating the observed (biased) population we obtain $\beta_1 \simeq 0.74$ for the Eurybates and $\beta_1 \simeq 0.94$ for the Arkesilaos families in the L4 swarm, and $\beta_1 \simeq 0.74$ for the Ennomos/Deiphobus clan in the L5 swarm (see Figure 16). These values are significantly larger than the slope $\simeq 0.46$ of the background population in the same magnitude range, signaling the families may be an important population partner to the background at smaller Trojan sizes. Obviously, this depends on their age, as collisional communication with the background population will grind the families and change the power-law slope of their size distributions from a certain size down (e.g., Marschall et al. 2022).

In order to prevent oversimplistic analytical assumptions about the magnitude distribution of the families, such as in (17), we use again the cubic-spline representation of $\log_{10} N_{fam}(<H)$ as above for the background population. While
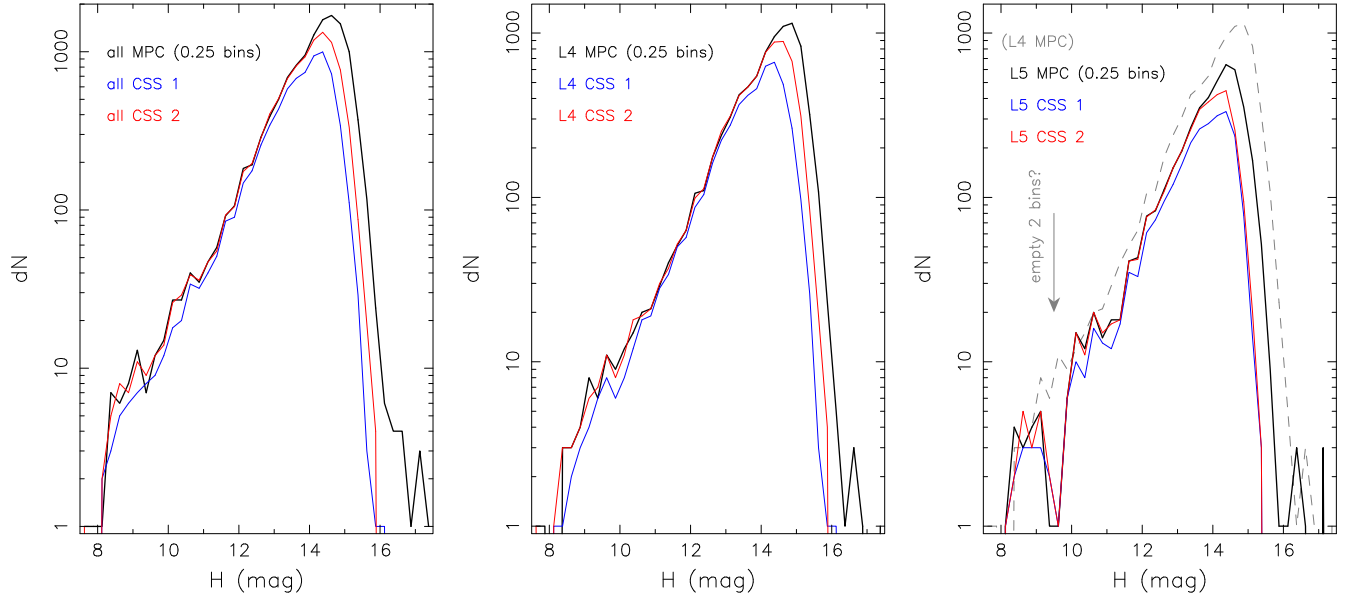
Figure 15. Differential magnitude distribution of Trojan populations (bin width 0.25 mag): (i) left is the complete count (L4 and L5 together), (ii) middle is the L4 cloud, and (iii) right is the L5 cloud. The black line is the population in the MPC database, the blue line is detections by CSS during phase I, and the red line is detections by CSS during phase II. The dashed gray curve on the right panel reproduces the MPC L4 population for the sake of comparison. We find it curious that the L5 population has nearly empty two bins centered at $\simeq 9.5$ mag: there are 46 L4 objects with $H < 10$ vs. 26 L5 objects with $H < 10$. While this may be an effect of a small number of statistics, the paucity of the L5 continues beyond magnitude 11.

Table 1
Parameters of the Trojan Families Included in Our Analysis

Family/location		$A_{\rm ref}$	$s_A^{\rm F}$	$\alpha^{\rm F}$	$B_{\rm ref}$	$s_B^{\rm F}$	$\beta^{\rm F}$	$C_{\rm ref}$	$s_C^{\rm F}$	$\gamma_1^{\rm F}$	$\gamma_2^{\rm F}$	$\sin I_{\rm P}$	$e_{\rm P}$	$H_{\rm LR}$	$N_{\rm mem}$
Eurybates	L4	0.129	0.004	3.5	0.049	0.009	2.6	1.553	0.04	1.1	1.75	0.129	0.044	9.82	875
Arkesilaos	L4	0.153	0.004	2.8	0.035	0.007	3.5	1.5	0.02	0.6	1.3	0.155	0.029	11.97	235
Hektor	L4	0.323	0.004	3.5	0.0553	0.007	3.5	1.558	0.05	1.3	2.1	0.326	0.054	7.45	118
Thronium[a]	L4	0.5252	0.004	4.5	0.0415	0.007	5	—	—	—	—	0.526	0.049	9.69	69
Teucer	L4	0.3565	0.004	3	0.0715	0.01	4	1.5	0.055	1.7	2	0.358	0.073	8.87	86
Ennomos[b]	L5	0.464	0.011	4	0.03	0.01	3	1.5	0.055	1.4	1.3	0.459	0.032	8.68	88
Deiphobus[b]	L5	0.505	0.018	4.5	0.032	0.008	4	1.5	0.05	0.9	1.6	0.475	0.029	8.45	233
2001 UV209	L5	0.415	0.007	2.5	0.041	0.006	3	1.5	0.01	0.1	3.5	0.415	0.041	12.62	46

Notes. For a more complete list of the currently known Trojan families and a discussion, see Appendix A, Table 4. The second column indicates in which swarm—L4 or L5—the family is located. The third to twelfth columns specify parameters of the family in A, B, and C parameter distributions defined in Equations (10), (11), and (12). The ninth and tenth columns are proper orbital elements of the largest fragment in the family for the sake of comparison (we use our new determination of the Trojan proper elements described in Appendix A and make them available in the electronic form at https://sirrah.troja.mff.cuni.cz/~mira/tmp/trojans/). The last columns give the absolute magnitude of the largest remnant in the family $H_{\rm LR}$ and the number of members in the nominal family $N_{\rm mem}$.
[a] Thronium was formerly called the 1996 RJ family in most of the previous literature. In this case, the $dN_{\rm fam}(C)$ was represented using a simple boxcar distribution between 1.5 and 1.53.
[b] These two families, overlapping in the space of proper orbital elements, were most often denoted just Ennomos family in the previous literature.

keeping $H_{\rm r} = 14.5$ for the absolute normalization parameter $N_{\rm fam}(<H_{\rm r})$, we can use fewer segments now. The exact number has been adopted for each of the families separately, with four segments used in the case of prominent families like Eurybates and Arkesilaos, and only three segments for other, less populous families.

4. Complete Trojan Population via Model Calibration on the CSS Data

After presenting (i) the available observations (Section 2), and (ii) the Trojan orbital and magnitude model (Section 3), we now describe how we connect them via adjustments to the free parameters of the model. Note that the model itself does not allow us to describe the observations directly because we need to account for and quantify incompleteness (bias) in the CSS

survey. It is only the convolution of the bias and the model that may be compared to the observations. So, the last element to be formulated is the bias description.

4.1. Detection Probability Defined on the Space of Model Parameters

Given our limited data set, we have chosen here to compromise complexity for computational efficiency. Consider that every single Trojan orbit is described by six orbital elements, and that this information is complemented by the body's absolute magnitude. Together, these seven parameters have their own probability of detection during the time-constrained survey, which in turn is limited by its photometric sensitivity. To avoid small number statistics in our method, we choose to downgrade the available information for each orbit by averaging.
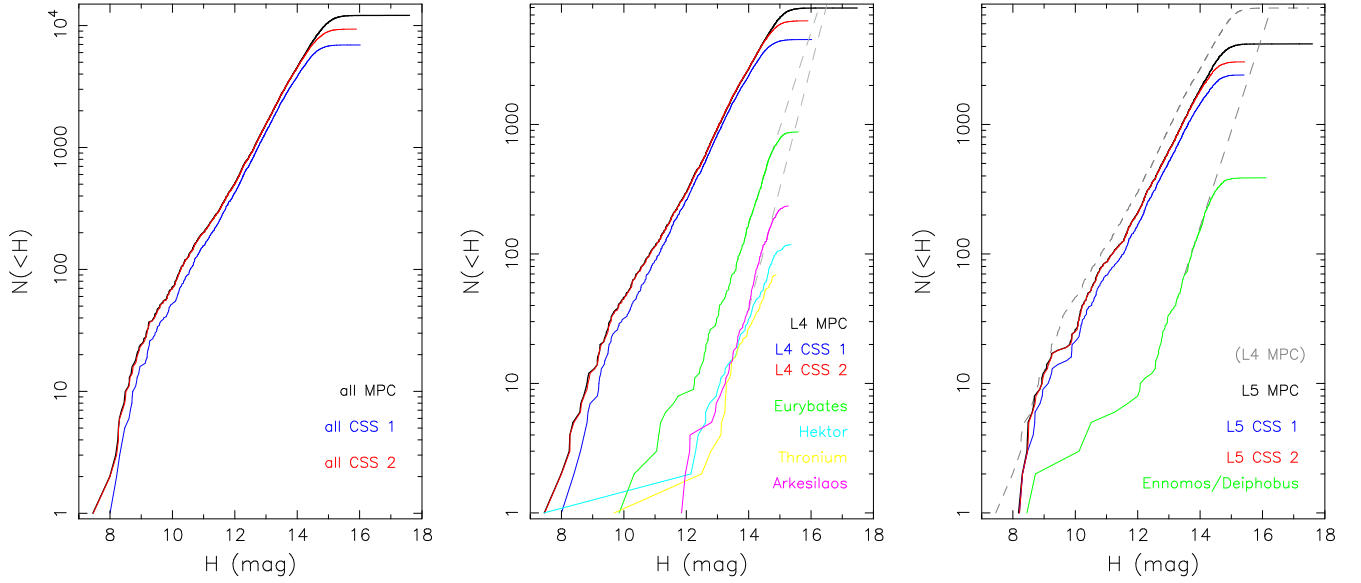
Figure 16. The same as in Figure 15, but now the cumulative rather than differential distribution is shown. The principal Trojan families are also shown: (i) Eurybates (green), Hektor (cyan), Arkesilaos (magenta), Thronium (yellow) in the L4 population, and (ii) Ennomos/Deiphobus clan in the L5 population. Eurybates has the largest population with 875 known members, followed by Arkesilaos with 235 known members (see Table 4). Even at magnitude 14.5 these two families represent compositely ≃12% of the total L4 population. Furthermore, the magnitude distribution is much steeper (see the dashed gray extrapolation), and their population may reach up to 25–30% of the total population at magnitudes 16.5–17 if continued with a straight power law. The Ennomos/Deiphobus is equally abundant among the L5 population: at magnitude ≃14.25, their population represents ≃10% of the total, and this fraction increases toward a larger magnitude.

The scheme is driven by the model, whose intrinsic parameters are the proper elements (A, B, C) and the absolute magnitude H. To make things simple, we shall assume the detection probability $\mathcal{P}$ is given as a function of the same parameters, namely $\mathcal{P} = \mathcal{P}(A, B, C; H)$. The Trojan population, predicted to be seen by the survey, is then given by the distribution function

$$dN_{\text{pred}}(A, B, C; H) = \mathcal{P}(A, B, C; H)$$
$$\times \, dN_{\text{model}}(A, B, C; H), \qquad (18)$$

which can be finally compared to the observations. Before we get to the method of this comparison (Section 4.2), we deal with the detection probability $\mathcal{P}$.

As to the orbital part, having $\mathcal{P}$ dependent on (A, B, C) only, implies averaging over the three complementary angular variables. Uniformity of the observed Trojan population in these angles appears as a reasonable justification for this procedure.[7] The most straightforward situation concerns the inclination (A) and eccentricity (B), for which the suppressed angles are directly φ and ψ in Equations (1) and (2). These equations also provide a simple mapping of (A, B, φ, ψ) onto osculating orbital elements (e, I, Ω, ϖ). The reader should keep in mind that neither of the resonant variables, da/a_J and $\sigma = \lambda - \lambda_J$, is suitable for the intended averaging. Rather, it would be a (polar) angular variable θ with the origin shifted to the respective libration center (L4 or L5), representing an affine parameter on the chosen $C = \text{const.}$ isoline. Put more simply, in the process of letting θ span the whole interval of values $0°–360°$, one completes one turn about the libration center along the chosen C − isoline.

The definition of θ still depends on how we scale the ordinate and abscissa in Figure 9. Here we follow

Milani ([1993](#)), who proposed a relation

$$da = 0.2783(\sigma - \chi_\star)\tan\theta, \qquad (19)$$

where $\chi_\star = \pm\pi/3$ corresponds to the respective libration center for L4 or L5 Trojans. Inputting (19) into Equation (3), one finds a correspondence of θ to σ and da on the given C − isoline. Unlike the da and σ minimum and maximum values,[8] this needs to be solved by numerical iterations, and it provides a one-to-one mapping of (C, θ) onto the remaining osculating orbital elements (a, λ).

With this preliminary information, we now outline the procedure for how we determine the detection probability $\mathcal{P}$ by the survey:

1. Consider a small bin about the central value (A, B, C), namely $(A - \frac{1}{2}dA, A + \frac{1}{2}dA, B - \frac{1}{2}dB, B + \frac{1}{2}dB, C, - \frac{1}{2}dC, C + \frac{1}{2}dC)$

---

[7] Further justification is provided by our numerical test in Appendix B.

[8] Given a certain value of the C parameter $(C > C_{\min} = 1.5)$, we can determine the limiting values of da and the resonant angle σ on the integral curve (3) analytically. The case of the semimajor axis is trivial because the minimum and maximum values $\pm a_J\sqrt{8\mu(C - C_{\min})/3}$ are readily obtained by plugging $\sigma = \chi_\star$ into Equation (3). A more interesting problem is to find extremes, say σ_1 and σ_2, of the resonant angle σ. This is a nice exercise of the "casus irreducibilis" within the Cardano family of cubic equation solutions. Intending to express the solution using real variables, we first define an auxiliary angle $\xi \in (\pi/2, \pi)$, such that

$$\sin\xi = \sqrt{1 - (3/2C)^3}, \quad \cos\xi = -(3/2C)^{3/2}. \qquad (20)$$

Then, we have

$$\sin(\sigma_1/2) = \pm\sqrt{\frac{2C}{3}}\cos\xi/3, \qquad (21)$$

$$\sin(\sigma_2/2) = \pm\sqrt{\frac{2C}{3}}\cos(\xi - 2\pi)/3, \qquad (22)$$

where the $\pm$ sign on the right-hand side corresponds to L4, resp. L5, case (thus σ either positive or negative).

and choose (A', B', C') within this bin assuming a uniform distribution. Complement it with randomly chosen angles (φ, ψ, θ) having again a uniform distribution in the 0° and 360° interval. The set $(A', B', C', \varphi, \psi, \theta)$ uniquely transforms into Keplerian orbital elements as described above. In order to sample a sufficient number of configurations, we generate $N_{\rm orb} = 5000$ such orbits within each bin. The epoch of osculation is MJD 60,000.0, or 2023 February 25, corresponding to the epoch of data in the MPC catalog we used for identification of the presently known population of JTs. Each of these orbits is numerically propagated backward in time over little more than a decade, namely to 2013 January 1, which precedes the first available frame of the phase I observations of CSS.

2. Next, we consider information about the CSS operations during phases I and II (Section 2). This includes a full list of frames with specific fields of view obtained at a certain specific time: there are (i) $N_{\rm FoV} = 61, 585$ such frames in phase I, and (ii) $N_{\rm FoV} = 162, 280$ such frames in the phase II operations of CSS (altogether making 223, 865 frames available). Nesvorný et al. (2024) conducted a detailed analysis of moving objects identified on each of these frames and determined their detection probability $\epsilon(m, w)$ as a function of the apparent magnitude m and the rate of motion w.

3. We then analyze the orbital history of the synthetic trajectories propagated from the orbital bins (A, B, C) and consider whether it geometrically appears in the field of view of any of the CSS frames. To that end, we use the publicly available `objectsInField` code (oIF) from the Asteroid Survey Simulator package (Naidu et al. 2017). For frames not crossed by the particular orbit, we assign a detection probability $\epsilon = 0$ when the body appears in a certain frame, and we use $\epsilon(m, w)$ to determine its detection probability. We test a sufficient range of absolute magnitudes H in between 7 and 19 (using 0.25 mag bins) and compute the apparent magnitude m on the frame using Pogson's relation:

$$m = H + 5 \log(R\Delta) - P(\alpha). \tag{23}$$

As expected, m is directly related to the absolute magnitude H –thus the dependence of $\mathcal{P}$ on H–plus several correction factors. The second term on the right-hand side of (23) simply follows from the flux dilution with heliocentric distance R and observer distance Δ. The last term is the phase function, dependent on the phase angle α (i.e., Sun–asteroid–observer); P describes the fraction of the asteroid's hemisphere seen by the observer that is illuminated by the Sun, but it also captures the complicated effects of the sunlight reflection and scattering in the surface layer. In accord with previous Trojan studies, we adopt a simple $H - G$ magnitude-phase function system

$$P(\alpha) = 2.5 \log[(1 - G)\Phi_1 + G\Phi_2], \tag{24}$$

relying on two base functions Φ_1 and Φ_2, whose contribution is weighted by the slope parameter G (see, e.g., Bowell et al. 1989; Muinonen et al. 2010), which read

$$\Phi_i = \exp\left(-A_i[\tan(\alpha/2)]^{B_i}\right) \qquad (i = 1, 2), \tag{25}$$

with empirical constants $A_1 = 3.33$, $A_2 = 1.87$, $B_1 = 0.63$, $B_2 = 1.22$. The partitioning slope factor G has to be found

from observations. The previous Trojan literature (e.g., Grav et al. 2011; Yoshida & Terai 2017; Uehata et al. 2022) used $G = 0.15$, and this was also our first choice as well. Shevchenko et al. (2012) conducted a careful study of the phase function for three bright Trojans and found a mean magnitude-phase slope of 0.042 mag deg^{-1} up to $\simeq 10°$ phase angle. This is in reasonable accord with the formulation in (24) and (25), and $G = 0.15$. While popular so far, we note that the canonical $G = 0.15$ has been found most appropriate for the taxonomic class C of asteroids. The more common D and P types among Trojans, however, have a mean magnitude-phase slope even steeper than the C's, making the effective G parameter lower, namely $G \simeq 0.09$ (e.g., Vereš et al. 2015). For that reason we consider this lower G value nominal in our work, saving the previously used higher value for simulations whose purpose is to calculate realistic uncertainties in our results. This procedure is especially important for the faintest detectable Trojans, for which the apparent magnitude m determined using Equation (23) is near the photometric detection limit of the survey. Modeling of additional factors of uncertainty in m, such as the role of the rotation phase in the detection of small, irregularly shaped Trojans with possibly large amplitude of the rotation curve (e.g., Chang et al. 2021; Kalup et al. 2021), represents a difficult problem and we do not include it in our analysis. For Trojans near the detection limit of the telescope, the corresponding noise element in the $m(H)$ relation (23) may not contribute with zero average. As a result, faint Trojans will be preferentially detected near the peak of their apparent magnitude variation, and thus deemed brighter. But we find this issue more of an interpretation problem (once the reader knows these effects have not been taken into account). Indeed, the inferred population of small Trojans will appear volumetrically larger than it really is, but this only means the resulting absolute magnitude distribution we obtain for Trojans in Section 5.2 should not be overinterpreted toward the physical parameters of the population.

As a result, we have for (i) each of the synthetic orbits $j = 1,\ldots,N_{\rm orb}$, (ii) each of the frames $k = 1,\ldots,N_{\rm FoV}$, and (iii) all the H magnitudes within the needed range, the corresponding detection probability $\epsilon_{j,k}$ computed. Finally, the representative detection probability of a given orbit in the (A, B, C) bin and a magnitude H over the whole duration of the survey is expressed as

$$\mathcal{P}(A, B, C; H) = \frac{1}{N_{\rm orb}} \sum_{j=1}^{N_{\rm orb}} \left\{ 1 - \prod_{k=1}^{N_{\rm FoV}} [1 - \epsilon_{j,k}] \right\}. \tag{26}$$

Note, that $\mathcal{P}$ is actually evaluated as a complementary value to the nondetection of the body, which on each frame reads $1 - \epsilon_{j,k}$. Similarly, we define the representative rate of detection

$$\mathcal{R}(A, B, C; H) = \frac{1}{N_{\rm orb}} \sum_{j=1}^{N_{\rm orb}} \sum_{k=1}^{N_{\rm FoV}} \epsilon_{j,k}, \tag{27}$$

providing the mean number of frames in which a Trojan in the bin around $(A, B, C; H)$ should be detected by the survey.

Table 2
Orbital Parameters and Absolute Magnitudes Considered in Our Model

Parameter	Minimum	Maximum	Bin Width	Number of Bins
A	0	0.7	0.025	28
B	0	0.25	0.01	25
C	1.5	2.05	0.01	55
H	7	17	0.10	100

Note. The second and third columns give the minimum and maximum values, the fourth column is the width of the bin, and the fifth column gives the number of bins.

4.2. Optimization of Model Parameters

The orbital-magnitude space is the arena in which the target function of the optimization is evaluated. In practice, we discretize it into a large number of bins about the central values $(A, B, C; H)$. Table 2 provides information about the range of their values and bin width. Altogether, there are more than 3.8 million bins (in reality, though, nearly half of the orbital bins are excluded, as they would lead to long-term unstable motion as determined in Section 3). This is far larger than the number of observations by CSS, which implies that the orbital-magnitude space is very sparsely populated by the data.

Consider a certain bin indexed j in which CSS detected $n_j(\geqslant 0)$ individual Trojans and, at the same bin, our model predicts $\lambda_j = dN_{\mathrm{pred}}(A, B, C; H)$ such objects (see Equation (18)). Assuming conditions of the Poisson statistics are satisfied, drawing n_j objects out of λ_j expected obeys a probability distribution

$$p_j(n_j) = \frac{\lambda_j^{n_j} \exp(-\lambda_j)}{n_j!}. \tag{28}$$

Combining the information from all bins in the orbital-magnitude parameter space, and assuming no correlations among the bins, we have a joint probability of the model prediction versus data

$$P = \prod_j \frac{\lambda_j^{n_j} \exp(-\lambda_j)}{n_j!}. \tag{29}$$

Finally, the target function (log-likelihood) is defined as

$$\mathcal{L} = \ln P = -\sum_j \lambda_j + \sum_j n_j \ln \lambda_j, \tag{30}$$

where a constant term $-\sum_j \ln(n_j!)$ has been dropped (representing just an absolute normalization of $\mathcal{L}$ that cannot affect the optimization of the model parameters). The parameter optimization procedure seeks maximization of $\mathcal{L}$ on the space of free parameters of the model. The role of the two terms on the right-hand side of (30) is complementary: (i) the first does not depend on n_j and thus this is the single contribution for those bins, where CCS has $n_j = 0$ detected Trojans; clearly, the situation when the model predicts a large number λ_j of objects needs to be penalized and thus the negative sign of this term; and (ii) the second term, which includes the number of detected Trojans n_j, combines in these bins with the first term to maximize $\mathcal{L}$ when $\lambda_j \simeq n_j$; clearly, the match of the model with data is the preferred configuration.

The optimization procedure seeks a maximum of $\mathcal{L}$ over the space of free parameters of the model. Because the new camera significantly improved CSS performance in 2016 May, we formally consider phases I and II described in Section 2 as two independent surveys. The target function to be maximized is a linear combination of the individual parts, namely $\mathcal{L} = \mathcal{L}_{\mathrm{I}} + \mathcal{L}_{\mathrm{II}}$. As for the parameter set, there are eight parameters of the $dN_{\mathrm{back}}(A)$, $dN_{\mathrm{back}}(B)$, and $dN_{\mathrm{back}}(C)$ distribution functions given by Equations (6), (7), and (8), defining the orbital distribution. The magnitude component has seven parameters of the background population $dN_{\mathrm{back}}(H)$ in Equations (15) and (16), and each of the Trojan families adds additional parameters (typically 4–5). Therefore, with up to five families, the L4 population requires altogether 38 parameters. The L5 population has only one significant cluster (the Ennomos/Deiphobus clan) and a smaller family of about 2001 UV209, making altogether 27 parameters when we represent each part in the Ennomos/Deiphobus clan as an individual family (Table 1).

We use powerful and well-tested MultiNest[9] code to perform optimization procedures, namely parameter estimation and error analysis (e.g., Feroz & Hobson 2008; Feroz et al. 2009). The popularity and power of MultiNest stems from its ability to efficiently deal with complex parameter space endowed with degeneracies in high dimensions. For the sake of brevity, we refer to the above-quoted literature to learn more about this versatile package.

5. Results

### 5.1. Detection Probability of CSS Trojan Observations

As an introductory step, we first describe the behavior of the detection probability $\mathcal{P}(A, B, C; H)$. We also define a population-averaged detection probability

$$\bar{\mathcal{P}}(H) = \frac{\int_{\mathcal{D}} dD \, w(A, B, C) \mathcal{P}(A, B, C; H)}{\int_{\mathcal{D}} dD \, w(A, B, C)}, \tag{31}$$

where the integration is performed over a stable domain $\mathcal{D}$ of the orbital parameter space ($dD = dA\, dB\, dC$), and $w(A, B, C)$ is some weighting function. A uniform weight $w = 1$ is the simplest choice, but this likely assigns too much statistical significance to the extreme borders of the orbital stability zone. We also used w defined by a product of the 1D distribution functions given in Equations (6)–(8), as a refined alternative. At this moment, we use the set of coefficients $(\alpha_1, \alpha_2, \ldots, \gamma)$ given in the caption of Figure 10, which matches the biased populations of Trojans. The reason is that we only want to illustrate the difference in the uniform weight case. In the same way, we also define the population mean rate of detection $\bar{\mathcal{R}}(H)$ with $\mathcal{R}(A, B, C; H)$ from Equation (27).

Figure 17 shows detection probability $\mathcal{P}(A, B, C; H)$ for fixed values $B = 0.055$ and $C = 1.605$, centers of the respective bins, as a function of the absolute magnitude H at the abscissa. Different gray curves are for 28 values of A, namely mid-values in the bins covering the definition interval $(0, 0.7)$ (see Table 2). The B and C values were purposely chosen to reach some of the principal Trojan families for a particular A value (see Table 1). As expected, the overall performance during
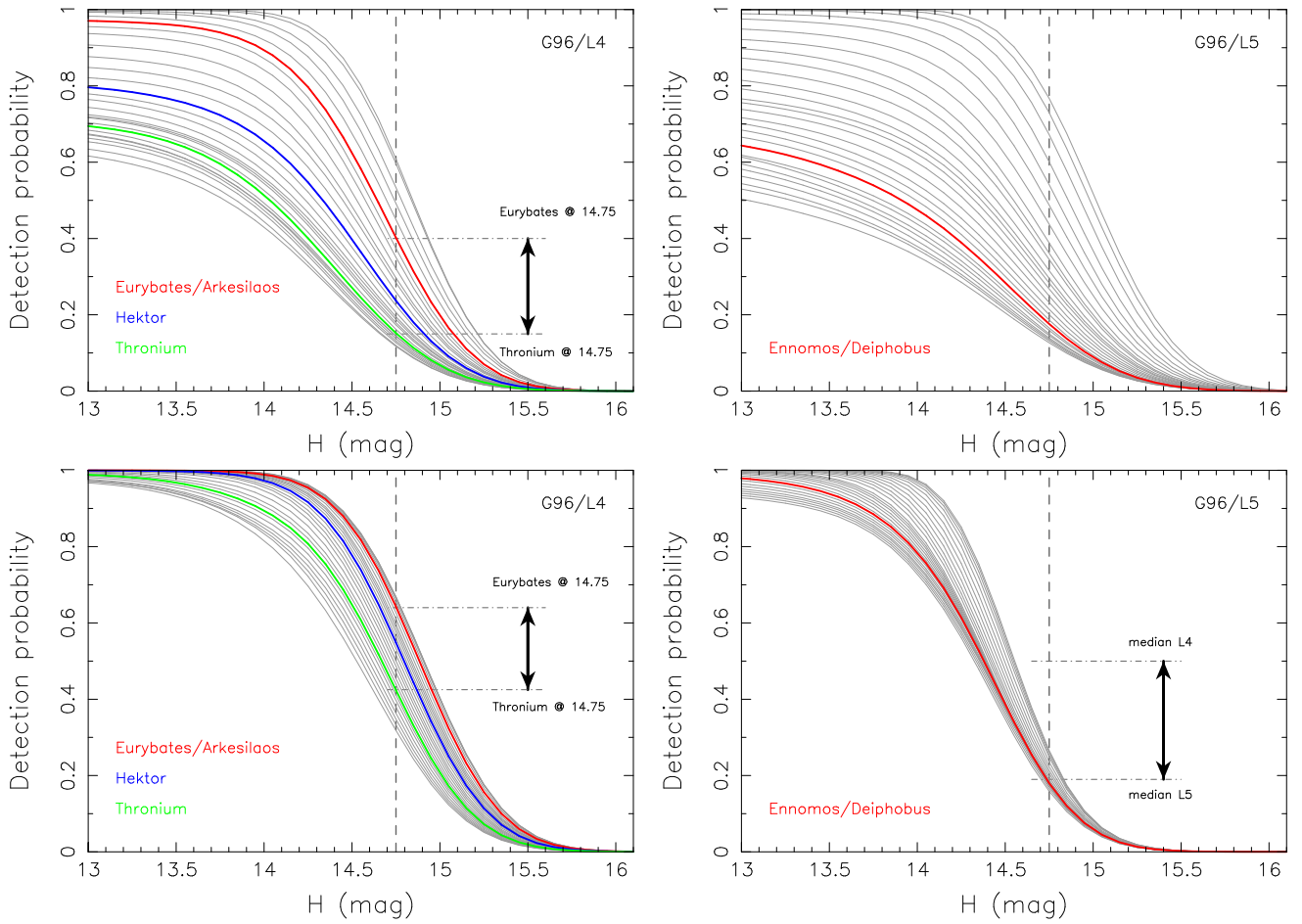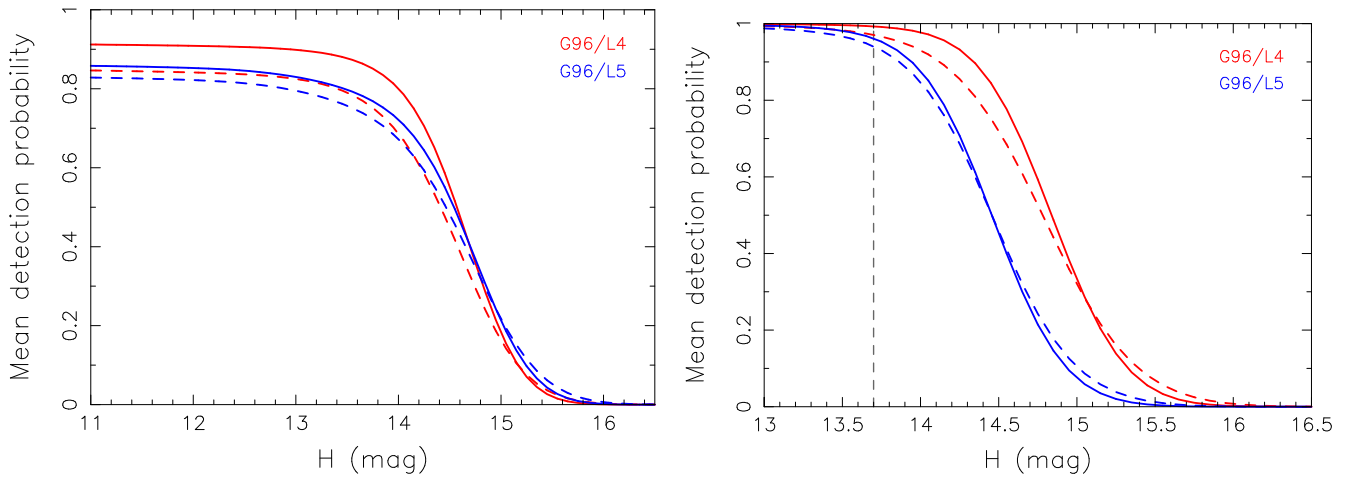

Figure 17. Detection probability $\mathcal{P}(A, B, C; H)$ of the L4 (left panels) and L5 (right panels) population Trojans in a specific set of the orbital bins centered about $B = 0.055$ and $C = 1.605$ values: various curves for a full range of values of the A parameter from 0 to 0.7 (the upper curves for the smallest A value, progressing to the lowest curve for the largest A values). The abscissa is the absolute magnitude H. The top panels are for phase I of the CSS operations, and the bottom panels are for phase II of the CSS operations (Section 2). The five major Trojan L4 and L5 families are intersected by the chosen string of bins at different values of A (i.e., orbital inclination). The respective detection probability curves are color-highlighted: (i) Eurybates centered at $A \simeq 0.125$ and Arkesilaos at $A \simeq 0.15$ (both represented in red, L4), (ii) Hektor at $A \simeq 0.325$ (green, L4), (iii) Thronium at $A \simeq 0.525$ (magenta, L4), and (iv) Ennomos/Deiphobus at $A \simeq 0.475$ (red, L5). Bins/families at higher inclinations have progressively smaller detection probability. For instance, at magnitude 14.75, the detection probability spread from the smallest to the largest inclination bins in the L4 population is $\simeq 0.4$ to $\simeq 0.72$ (phase II) and $\simeq 0.12$ to $\simeq 0.65$ (phase I). Detection probability in phase I and high-inclination bins are systematically much lower, not reaching unity even for large Trojans (small H values). A more subtle effect concerns phase II, in which the detection probability for the same bins in the L5 swarm levels off the unity earlier by about 0.3 mag.

phase II is much better than in phase I of the CSS operations (Section 2). In the former part, the detection probability does not reach unity at mid and high inclinations, even for bright Trojans. This is because this phase was shorter, but mainly the fields of view pointed near the ecliptic plane, not reaching large ecliptic latitudes (Figure 2). At low inclinations, phase I detection probability is nearly as good as that during phase II for L5 Trojans but still worse for L4 Trojans. The family corresponding detection probability profiles are highlighted by colors and indicated by labels. The lowest-inclination families (Eurybates and Arkesilaos) have a detection advantage over the highest-inclination family (Thronium). The effect is not too large for bright objects during phase II, but at the faint end ($H \geqslant 14.5$, say), the detection probability in the Thronium family is nearly twice as small as the Eurybates family. A similar trend is also seen in the L5 swarm (right panel). The sensitivity of the observations for the high-inclination zone of the Ennomos/Deiphobus clan is poor at the faint end: at $H \geqslant 14.75$, shown by the dashed line, the detection probability reaches barely 30% during phase II, and only 20% during phase I. Indeed, the right panel on Figure 16 shows that the

detected population of the Ennomos/Deiphobus clan levels off the straight power law at $\simeq 14.1$ mag. A subtler effect is seen in comparison of the L4 and L5 detection probabilities during phase II. The L4 detection probability is systematically higher than the L5 detection probability (at $H \simeq 14.75$ mag, the difference in mean detection probability may only reach values modestly smaller than a factor of 2).

Figure 18 shows the population-averaged detection probability $\bar{\mathcal{P}}(H)$ from Equation (31) for both L4 and L5 swarms and for both phases I (left panel) and II (right panel). This is global information for the swarms from the respective phases, such that many different factors related to fields of view pointing, galactic-plane intersection, and phase of Jupiter's motion in decl. contribute nontrivially to these curves. The comparison of the sensitivity during phase I and II therefore exhibits different behavior, whose main aspects can be straightforwardly understood.

During phase I, the detection probability for the L4 and L5 swarms reaches nearly the same H limit (with $\bar{\mathcal{P}} \simeq 0$ at $H \simeq 16$), but never reaches unity, even for bright Trojans. Additionally, the effect is more serious for the L5 swarm, for

Figure 18. Detection probability $\bar{\mathcal{P}}(H)$ of the L4 (red curve) and L5 (blue curve) population Trojans averaged over all orbital bins. Two variants of weighting defined in Equation (31) are shown: (i) a uniform weight $w = 1$ (dashed lines), and (ii) a weight based on Equations (6)–(8) (solid lines). The abscissa is the absolute magnitude H. The left panel is for phase I of the CSS operations, and the right panel is for phase II of the CSS operations (Section 2). The vertical dashed line at 13.7 mag in the right panel is an approximate formal completeness limit. This limit is not reached during phase I because of its shorter timespan and fields of view pointing near the ecliptic (thus missing a fraction of high-inclination Trojans).

which $\bar{\mathcal{P}} \simeq 0.87$ at $H \simeq 11$, while $\bar{\mathcal{P}} \simeq 0.92$ for the same magnitude for the L4 swarm. This stems from the fact that G96 operations during phase I were limited to fields of view near the ecliptic and did not reach large latitude zones. This means that segments of high-inclination orbits among Trojans escaped observations, and the effect is independent of object brightness.

Another type of behavior is observed in phase II. Here, we find that $\bar{\mathcal{P}}(H) \simeq 1$ up to $\simeq 13.7$ mag for both swarms, beyond which the detection probability levels off. Interestingly, the L5 population is more biased, as already noted in Figure 17. The relation between the two population curves in Figure 18 may be approximately characterized as a $\simeq 0.35$ mag shift. Overall, this finding confirms earlier estimates of the completion limit of JTs (e.g., Hendler & Malhotra 2020). Indeed, the largest Trojans discovered within the past decade are 2013 BD8 in L4 (with $H = 13.7$) and 2013 SP62 in L5 (with $H = 13.6$), and there are only 4/9 discovered Trojans during this interval of time brighter than $H = 14$ in L4/L5. At magnitudes $\simeq 16$ and $\simeq 15.5$, for L4 and L5 swarms, $\bar{\mathcal{P}}(H) \simeq 0$ because the Trojans become too faint even at the perihelia of their orbit to overcome the apparent magnitude limit for the G96 detection. The reason for the magnitude shift was discussed at the end of Section 2 (see Figure 8) and has to do with systematically larger heliocentric and geocentric distances of the L5 Trojans during phase II of the G96 operations.

This shift is confirmed in Figure 19, where we compare the number of detections for the observed Trojans with the population-averaged prediction $\bar{\mathcal{R}}(H)$ (using the simple weighting based on Equations (6)–(8) and preliminary parameters from matching the biased population in Figure 10). The spread in the number of detections for a given absolute magnitude, shown by blue vertical intervals, indicates principally the expected dependence of this quantity in the orbital inclination. There are generally fewer detections during phase I, and detection of L4 Trojans during phase I reaches up to magnitude 16, while only $\simeq 15.6$ for L5 Trojans. The theoretical curves roughly match the trend seen in the observations, whose scatter is large. This is partly because we have combined observations of Trojans at all possible orbits but also because it is likely that $\bar{\mathcal{R}}(H)$ is more sensitive to the averaging over the angular variables (φ, ψ, θ) associated with

the elements (A, B, C) (Section 4.1). At this moment, we satisfy ourselves with the fair agreement but do not use information about the detection rate in the model fitting procedure.

5.2. Bias-corrected L4/L5 Populations

We now describe the main results, namely properties of the bias-corrected population of the L4 and L5 clouds of JTs. We start with a nominal model that has the maximum absolute magnitude set to 15. We find there are too few observations of L5 Trojans by G96 beyond this limit (see Figure 15). As a result, we explore the solution beyond $H = 15$ only for L4 Trojans in an extension of the nominal solution at the end of this section.

We combine full sets of CSS phase I and phase II detections for both L4 and L5 observations. In each of the survey phases, we use unique detections only (i.e., we do not account for Trojan redetections). However, considering the two CSS phases separately, a number of objects may be detected in both of them. The observations are mapped onto the bins in $(A, B, C; H)$ as described in Table 2. Next, we run simulations[10] using `MultiNest` to optimize parameters of the global model described by Equation (14), with the observation prediction given by the convolution of the model with the detection probability as in Equation (18). Recall the model has a (i) smooth background component, and (ii) contribution from selected Trojan families. In the case of the background population, we adjust the parameters of the orbital distribution described in Equations (6)–(8) and the absolute magnitude distribution (in the nominal setup in between magnitudes 7 and 15 using six segments; Table 3 and Figure 23). In the case of the families, we use distribution functions in Equations (10) to (12) with fixed parameters listed in Table 1 to make them identified in the orbital space (A, B, C), and we adjust only parameters of their absolute magnitude range of values (H_1, H_2) individual to each family. The range for each of the families is shown by the gray polygons in Figure 23. The largest family members typically have an irregular distribution of magnitudes that is not suitable for any analytic representation. This sets our

---

[10] These simulations were run on the NASA Pleiades Supercomputer.
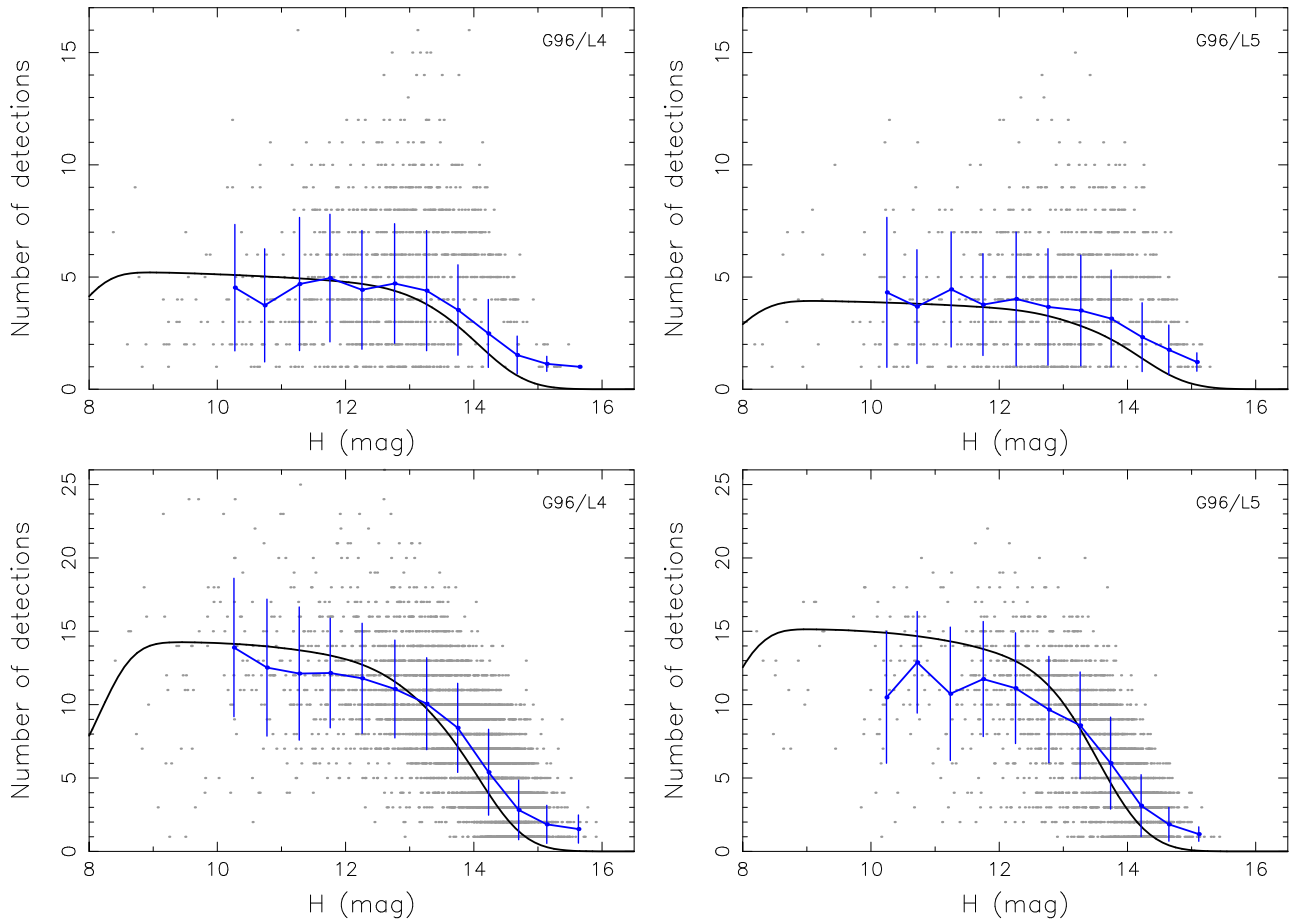
Figure 19. Number of independent detections (gray symbols) for Jupiter Trojans observed by CSS station G96 during the phase I (top panels) and phase II (bottom panels) period (Section 2). The left panels are for the L4 swarm, and the right panels are for the L5 swarm. The abscissa is the absolute magnitude H. The black curves provide the predicted detection rate $\bar{\mathcal{R}}(H)$ for G96 determined by averaging over all long-term stable (A, B, C) bins using weights based on Equations (6)–(8). The blue curves are simply mean values of detection counts grouped in 0.5 wide bins in absolute magnitude, and the vertical bars represent the standard deviation within the respective magnitude bin. By their definition, the blue curves cannot decrease below one detection, while the predicted rates may. This produces an apparent mismatch beyond $H \simeq 14.5$–15.

individual choice of H_1 for each of the families. Having avoided modeling the largest few members in the families is not a problem for the global model because we make sure that the population is complete to H_1. The maximum value H_2 expresses a limit beyond which the nominal family, determined by the clustering method in the proper element space (see Appendix A), already has too few members detected by CSS.

The typical value of H_1 ranges from 12.2 to 13.3, while the H_2 values span an interval between 14.7 and 15. Note that the location in orbital space is the only information about the families we provide to the optimization procedure. We do not separate the background and family populations in the observations and let the split be decided by the `MultiNest` algorithm uniquely.

`MultiNest` also provides posterior distributions of model parameters. These help us to determine the uncertainties of the parameter values (the best-fit and uncertainty values for the background populations parameters for the nominal model are listed in Table 3) as well as higher-dimensional statistical quantities, such as parameter correlations. They also serve to construct posterior models, useful to visualize and check on the validity of the results, as they are confronted with observations using different parametric projections.

Comparison of the biased model to the observations. Figures 20 and 21 show the biased model predictions

(Equation (18)) compared to the observations using 1D projections in all parameters $(A, B, C; H)$ for both L4 and L5 clouds. The solution for the L4 population is markedly superior to the solution for the L5 population. This is because of two factors: (i) the available observations of L5 Trojans are less numerous, and only a few of them reach the last magnitude segment between 14.5 and 15 (see the right panel of Figure 15), and (ii) the Trojan families in the L5 cloud are extended and diffuse, which makes their precise identification more difficult to determine (see Figure 11). Finally, the mask functions for the largest L5 families, Ennomos and Deiphobus, partly overlap (see Table 1), which brings additional confusion to the solution of the L5 population.

As a result, the biased model of the L5 population exhibits several drawbacks; for instance (i) it does not decrease very fast in the last segment of the CSS phase I observations (Figure 20), or (ii) it falls short in a compromise between the background and family signal in orbital space (see especially the A coordinate on Figure 21). While not perfect, the correspondence between the biased model prediction and the CSS data is much better for the L4 population. More compact Trojan families in the L4 cloud reveal their identity more clearly in the fitting procedure. Figure 21 confirms that the smooth background population matches the expected trend over which the principal families contribute with the foreseen punctual signal.

Table 3
Median and Uncertainties of Jupiter Trojan Background Population Parameters
in the Nominal Model

	Median	$\pm\sigma$	Median	$\pm\sigma$
	Orbital distribution parameters			
	L4 parameters		*L5 parameters*	
s_A	0.0533	0.0105	0.3352	0.0178
α_1	1.274	0.091	0.644	0.046
α_2	1.008	0.063	3.012	0.247
s_B	0.0191	0.0028	0.0307	0.0041
β_1	1.156	0.077	1.106	0.086
β_2	1.144	0.061	1.140	0.088
s_C	0.0507	0.0031	0.0443	0.0036
γ	0.941	0.030	0.929	0.038
	Magnitude distribution parameters			
	L4 parameters		*L5 parameters*	
N_{back}	3951	44	2664	39
γ_1	1.236	0.448	1.404	0.386
γ_2	0.656	0.094	0.638	0.090
γ_3	0.429	0.021	0.431	0.025
γ_4	0.497	0.014	0.468	0.016
γ_5	0.447	0.008	0.473	0.010
γ_6	0.388	0.055	0.344	0.009

Notes. The L4/L5 cloud parameters in their respective columns. The seven parameters at the bottom part of the Table specify the cumulative magnitude distribution: (i) γ_i are mean slopes on seven magnitude segments defined by intervals (7–8.5, 8.5–10, 10–12, 12–13, 13–14, 14–15), and (ii) $N_{back} = N_{back}(< H_r)$ is the complete population up to $H_r = 14.5$ mag. The eight parameters at the top part of the Table specify parameters of the orbital distribution in the (A, B, C) space, Equations (6), (7), and (8).

The small differences may be due to the large bins we used. The fit of the magnitude distribution of both the phase I and phase II data in Figure 20 is fairly satisfactory in this case, too.

Figure 22 shows the posterior distribution for the 15 parameters of the background L4 population organized in the triangular form, which allows us to see possible mutual correlations. A well-behaved model is perceived to have no, or minimum number of, correlations between the parameters. In our case, this is the situation of the magnitude sector of the model (parameters 9–15). Certain groups of the orbital distribution parameters are found to be strongly correlated with each other: $(s_A, \alpha_1, \alpha_2)$ of the A distribution function $dN_{back}(A)$, (s_B, β_1, β_2) of the B distribution function $dN_{back}(B)$, and (s_C, γ) of the C distribution function $dN_{back}(C)$ (see the subdiagonal plots of the first eight parameters in Figure 22). This behavior is understood by inspecting the formulae (6), (7), and (8); for instance, s_A and α_2 literally form a single parameter $s_A' = s_A^{\alpha_2}$ in Equation (6), and thus their values must be highly correlated. Nevertheless, the robustness of MultiNest algorithm makes the result well behaved. Reparameterization of the orbital distribution functions may lead to a set of parameters with lower correlations, but as long as the optimization scheme does not fail, this is not a serious problem.

Properties of the bias-corrected model. Figure 23 shows the cumulative distribution of the bias-corrected population of the L4 and L5 clouds. The model naturally provides the background population separated from the population in the families. To more easily make a one-to-one comparison, we also show CSS observations, which were, for the purpose of this figure, divided into background and family components; both are shown by red lines, those from phase I are dashed, and those from phase II are solid. We also show the complete

background population of L4 and L5 Trojans identified in the MPC database (in blue). This population contains a surplus of faint Trojans with $H \geqslant 14.5$ that were not detected by CSS but instead by larger-aperture surveys (e.g., Pan-STARRS) or the occasional dedicated efforts using large telescopes (e.g., Subaru). We find it useful to display this data set, even though it is obviously a biased sample, as it represents a reference basis. The bias-corrected population determined by our model must at every magnitude exceed this total population. As before, the solution of the L5 population barely passes this criterion, while that of the L4 population easily meets the test. This confirms the abundant nature of the L4 population over the L5 solution for the reasons outlined above.

The solution for the family populations may appear disappointing at first sight. Considering the limitations of our approach, however, we find it satisfactory how the major families are reasonably reconstructed in both clouds. In particular, the Eurybates family in the L4 population is well resolved and has a population of 385 ± 20 members with $H < 14.5$ as well as a cumulative magnitude slope changing at the same reference magnitude from 0.78 ± 0.05 to 0.60 ± 0.04. Here, just the last segment solution with a shallower slope is not exact. Similarly, the solution for the Deiphobus family in the L5 cloud indicates 210 ± 10 members with $H < 14.5$ and a change of the cumulative slope from 0.65 ± 0.12 to 0.40 ± 0.09. As in the Eurybates family case, the slope in the last segment is obviously again underestimated. Apart from the scarce set of observational data beyond 14.5 in the high-inclination zone of the L5 cloud, the additional complications are due to the Deiphobus family, which partially overlaps with the Ennomos family. The MultiNest solution tends to assign some of the Deiphobus members to the Ennomos part. The solution of smaller families, with only tens to hundreds of members, is less accurate (Figure 23). Recall that MultiNest only provides general information about the position of the families in orbital space. It then objectively decides how to sort the observations into the background and family populations. When the families are large and diffuse, and when they contain only small to limited numbers of members, the solution is necessarily approximate. Yet, it contributes some value to the model (note, for instance, the contribution of the small L4 families to the orbital parameter distribution on the top panels of Figure 21).

Figure 23, and parameters listed in Table 3, generally confirm previous results concerning the magnitude distribution of JTs: (i) a steep segment with a power-law exponent $\gamma \simeq 0.91$ to magnitude $\simeq(8.5–9)$, (ii) followed with a shallower part characterized by a power-law exponent $\gamma \simeq (0.45–0.5)$ to a certain break point H_b, (iii) beyond which the magnitude distribution becomes even shallower with $\gamma \simeq 0.36$ (see, e.g., Wong et al. 2014; Wong & Brown 2015; Yoshida & Terai 2017; Uehata et al. 2022). The literature differs at H_b, with values ranging from $13.56^{+0.04}_{-0.06}$ (Yoshida & Terai 2017) to $14.93^{+0.73}_{-0.88}$ (Wong & Brown 2015). In previous works, a rigid broken power-law model has often been applied to the observations. We believe our spline representation of the magnitude distribution is more flexible and accurate at the expense of only a small increase in the number of free parameters (with an additional quality of fitting the background population).

Results in Table 3 indicate the reality is more complicated than a simple change of the power-law slope at a certain break
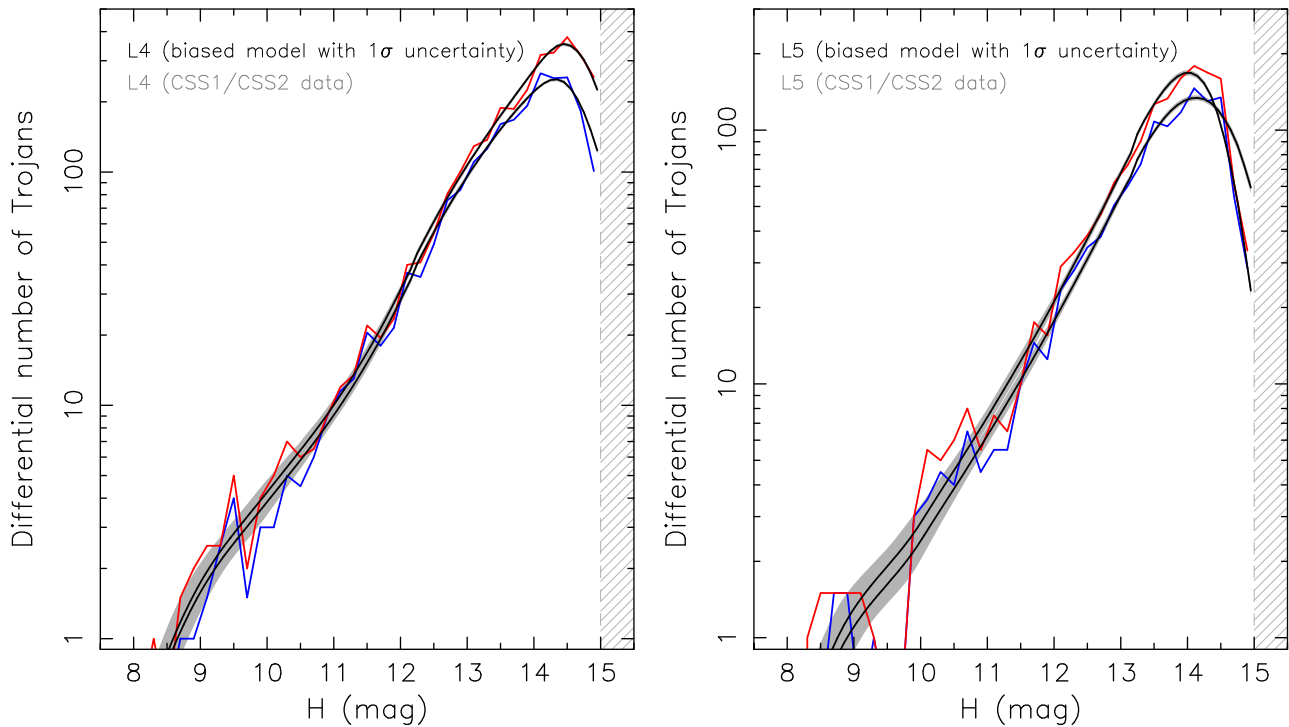
Figure 20. Differential magnitude distribution of the G96 observations (blue for phase I and red for phase II) compared with the best-fitting biased model (black line with a σ interval, based on analysis of 10,000 posterior random samples of the model, depicted by the gray zone). The left panel is for L4 Trojans, and the right panel is for L5 Trojans. The magnitude bin has a width of 0.1 mag for the model and 0.2 mag for the data.

point. The magnitude distribution in both Trojan clouds exhibits subtle features, such as a slight change from shallower to steeper slope values in the third and fourth magnitude segments.[11] Figure 24 shows the power-law slope variations at the highest resolution, namely 0.1 mag of the bins used. The switch between steep and shallow regimes at $\simeq 9$ mag is still the dominant feature. We can also conclude that the slope values of the L4 and L5 populations are statistically equivalent up to $\simeq 14$ mag. Beyond this value, we have less confidence in the L5 solution. The slope exponent of the L4 population indicates a small but steady decrease beyond 13 mag. This gradual change is perhaps the origin of the different H_b values mentioned above. The local slope at $H = 15$ is formally $\gamma = 0.38 \pm 0.01$. There is a small slope difference of the L4 and L5 clouds between magnitudes 9 and 10, with the L4 population having a steeper trend.

We find that this behavior is formally at the origin of the population L4/L5 asymmetry in our model. This is best seen in Figure 25, where the left panel shows the bias-corrected differential magnitude distributions of the L4 and L5 Trojan background populations. They are statistically different beyond $H \simeq 11$. In particular, the L4 distribution appears to be shifted by $\Delta H \simeq 0.4$ mag toward smaller H if compared to the L5 distribution (the break of the L5 population to a shallow trend

beyond $H \simeq 14$ is an artifact of scarce data set in this case and should not be trusted).

The origin of the population difference in magnitude-limited samples is unknown, leaving it open for speculation and hypothesis. For instance, assuming the underlying size distributions are the same for L4 and L5 Trojans, the inferred magnitude distribution shift may be caused by $\simeq 1-10^{-0.4\Delta H} \simeq 0.44$ fractional difference in the mean albedo value, such that small L4 Trojans would have a mean albedo of $\simeq 0.05$ and small L5 Trojans would have a mean albedo of $\simeq 0.07$, as an example. While apparently not huge, such an albedo difference would have been significant. There is no clear reason for this to happen. Data in Grav et al. (2011) and Grav et al. (2012) indicate the albedo distribution for the Trojans becomes much wider below $\simeq 30$ km (approximately magnitude 11 for albedo value 0.07), but there is no statistically substantial difference between the L4 and L5 populations at these smaller sizes. Additionally, recent observations focused on Lucy mission targets (e.g., Buie et al. 2018, 2021; Mottola et al. 2023) found that WISE albedo determinations for Trojans could be systematically too high (an issue possibly related to the shape uncertainty).

Another possibility, or rather a congruent effect, would be a slight difference in shape statistics of the L4 and L5 Trojans: more irregular shapes tend to have a larger cross section (and thus brightness) on average than less irregular shapes. If the L4 population has undergone slightly more collisional evolution than the L5 population (see, e.g., O'Brien & Morbidelli 2008), resulting in systematically more irregular shapes of small objects, it would appear on average slightly brighter. McNeill et al. (2021) use the observations from the ATLAS survey to support the case.

The asymmetry of the L4/L5 clouds in magnitude-limited populations has been discussed for more than a decade. Possible evidence for some kind of asymmetry of the orbital

---

[11] We performed a quantitative test supporting the need to represent the magnitude distribution of the background population with cubic splines in the following way. L4/L5 populations restricted to absolute magnitude 13.5 were fitted using our core model and, alternatively, by a test approach in which the cubic-spline magnitude representation was replaced by the traditional broken power-law recipe (Equations (15) and (16)). Upon convergence, we compared Bayesian-based evidence factors $\ln Z$ of the best-fit solutions provided by `MultiNest`. The relative preference of one over the other models is directly by $\exp(\Delta \ln Z)$ value. We obtained 5×10^{-3} for L4 and 10^{-5} for L5 in favor of the cubic-spline model.
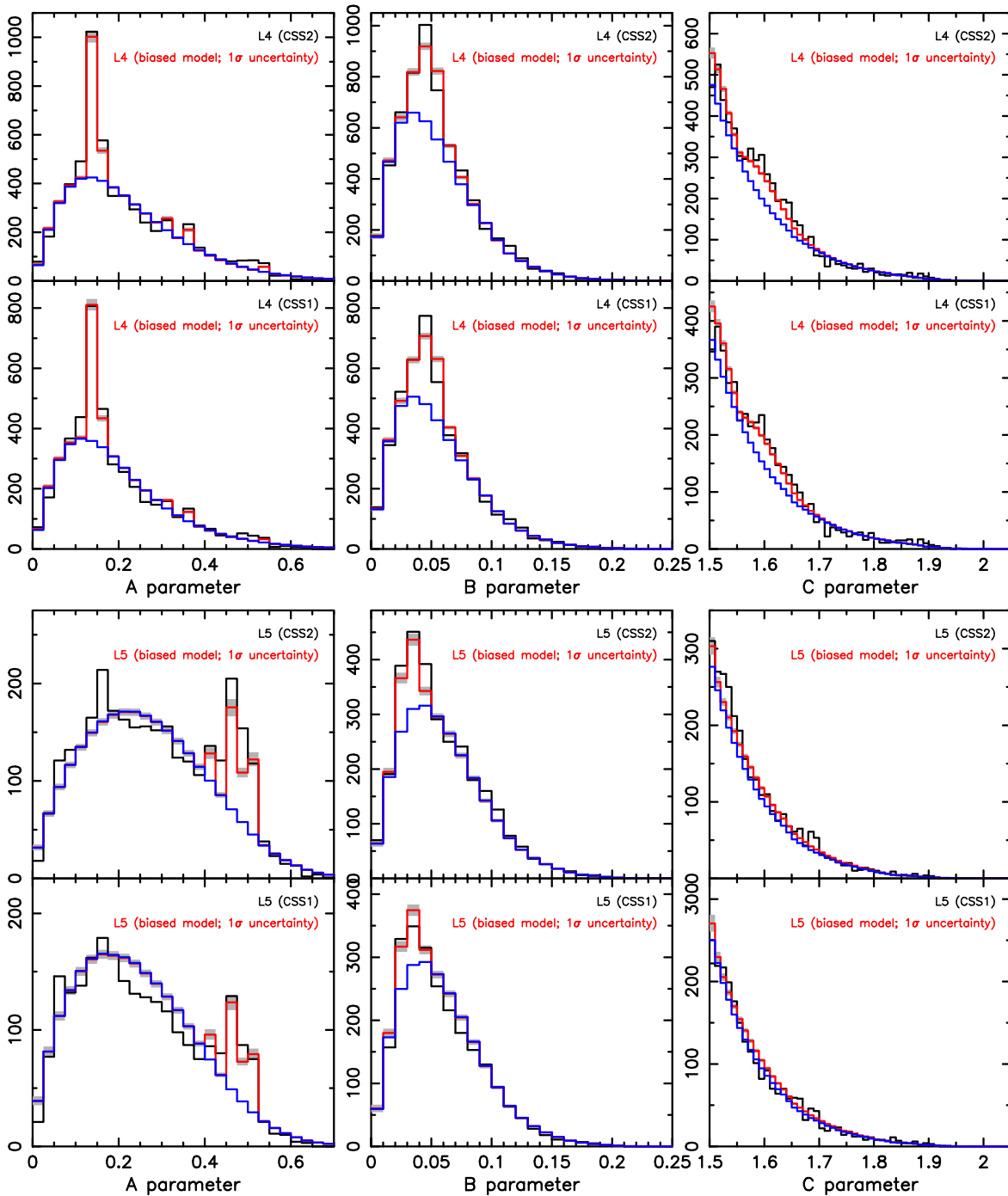
Figure 21. Projected distributions of the orbital parameters A (left), B (middle), and C (right) of the biased populations from our model (red lines) and the G96 observations (black histogram) using the phase I (bottom sectors) and phase II (top sectors) data: L4 data at the top panels, L5 data at the bottom panels. The shaded gray area delimits the σ region of the solution (created by 10,000 posterior random samples of the model). The blue histogram is the best-fitting model of the background population.

architecture of the L4 and L5 stability zones has yet to be identified. The above-mentioned anomalies in the inclination distribution (e.g., Jewitt et al. 2000; Slyusarev & Belskaya 2014) are readily explained by the population of the principal Trojan families. Separation of the families from the background has been one of the major goals of this work.

Therefore, we can now revisit the issue of a possible orbital asymmetry between the L4 and L5 populations more substantially by limiting our studies to the background populations in both clouds. The upper panels in Figure 26

show the cumulative distribution of the three orbital elements A, B, and C for background populations with a magnitude cut at $H = 13.5$. We used this limit because we previously argued that the L5 solution is less reliable for faint Trojans. These results have been obtained by specifically fitting the Trojan populations restricted to this magnitude, but they appear fairly similar to those obtained from the complete fit by limiting to magnitude 15 and downgrading to magnitude 13.5. Applying the Kolmogorov–Smirnov (KS) test to compare L4 and L5 data for distributions of the three elements, we obtain $D = 0.221$,
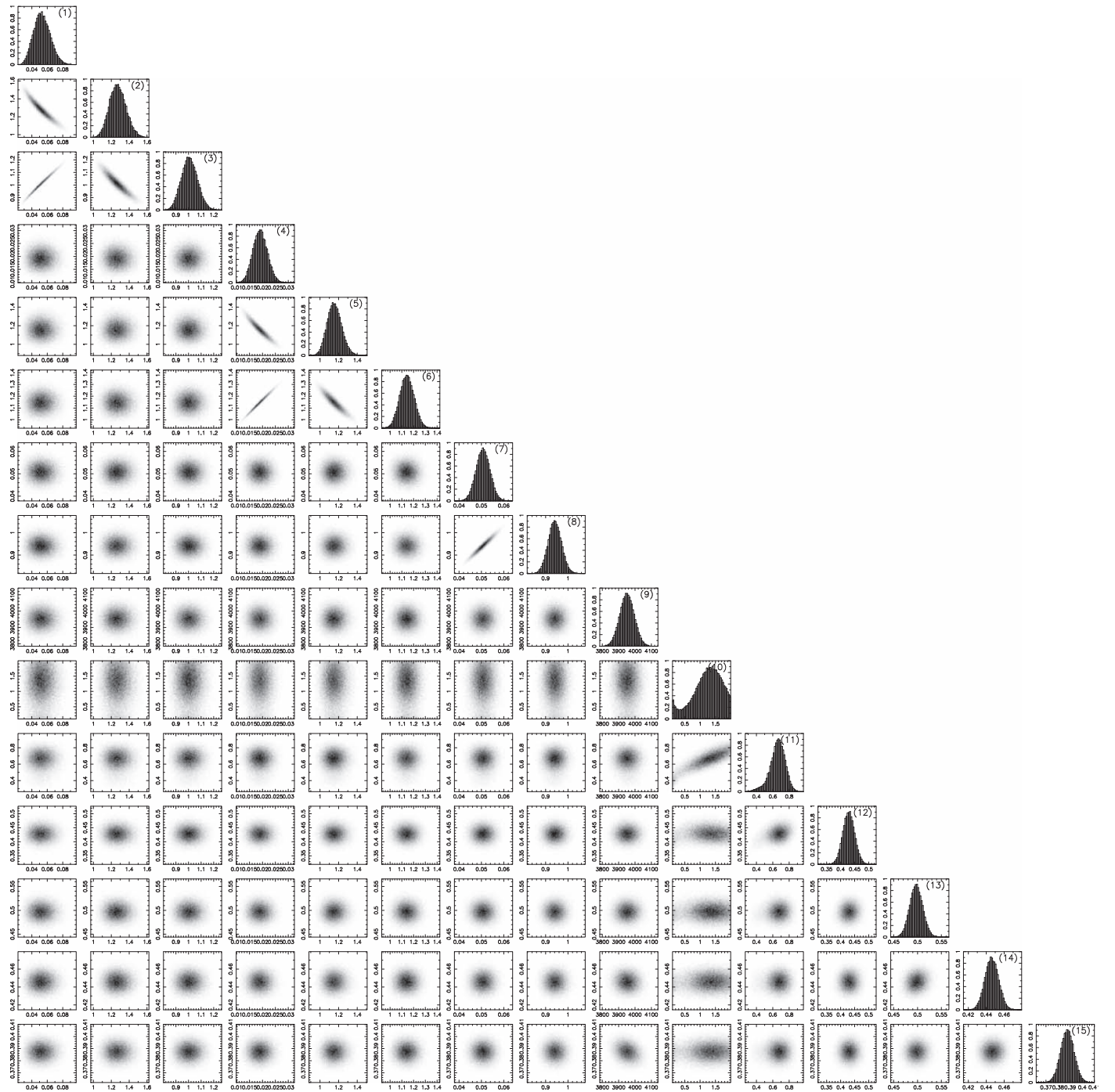
Figure 22. The posterior distribution of 15 model parameters characterizing the background population of the L4 Trojans from our nominal MultiNest fit to G96 observations (sometimes called the "corner diagram"; the L5 solution shows a fairly similar pattern). The individual plots are labeled (1)–(15) following the model parameter sequence given in Table 3; the first eight parameters determine the orbital distribution in *A*, *B*, and *C* elements, and the last seven parameters determine the absolute magnitude cumulative distribution (with the ninth parameter being the normalization at 14.5 mag), and the last six parameters the mean slope values in the chosen segments (Table 3).

$D = 0.051$, and $D = 0.043$ as a KS distance in the *A*, *B*, and *C* elements. With the background population numbers from Table 3, $N_4 = 1587$ and $N_5 = 1083$, which have been rescaled to the $H=13.5$ limit, we obtain the probability of the distributions being drawn from the same sample to be $\leqslant 10^{-20}$, 0.08, and 0.17 for *A*, *B*, and *C* distributions. While not entirely robust, the distributions of the *B* and *C* elements appear to be statistically similar, while the *A* distributions are distinct. The extent of the formal σ areas about the best-fit

distributions, constructed from the a posteriori variants of the fit, conform to the conclusion. To make sure these results are not affected by the choice of the limiting magnitude, we repeated the test, restricting now the Trojan populations to magnitude $H = 12$ (bottom panels in Figure 26). The cumulative distributions in all orbital elements exhibit the same behavior as before. The KS distances of the best-fit solutions are only slightly changed to $D = 0.193$, $D = 0.093$, and $D = 0.084$ for the *A*, *B*, and *C* distributions. The smaller
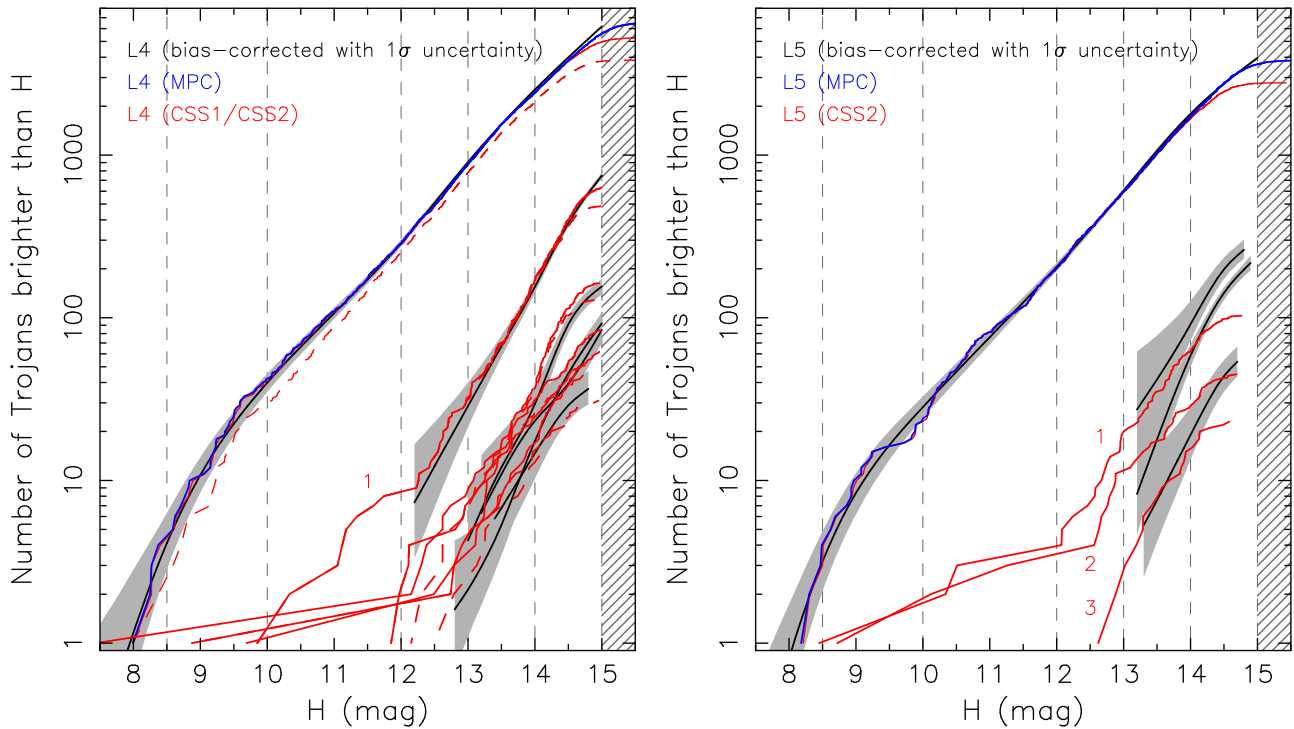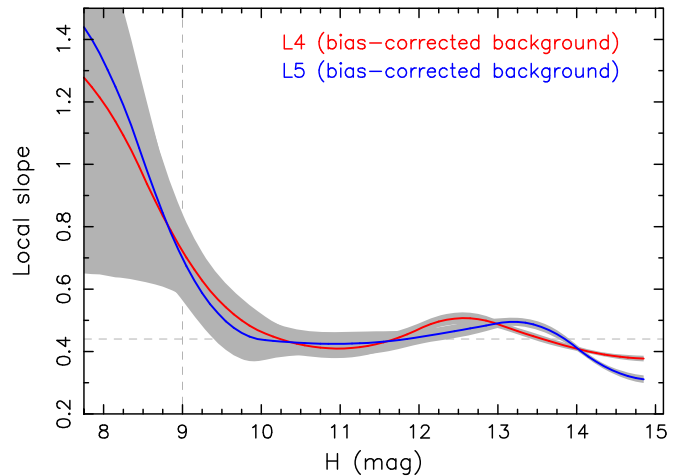
Figure 23. Bias-corrected cumulative magnitude distribution of the L4 (left panel) and L5 (right panel) Jupiter Trojan populations based on G96 observations. The background population, shown by the upper curves, is separated from the major families: (i) Eurybates (label 1), Arkesilaos, Hektor, Thronium, and Teucer in the L4 population, and (ii) Deiphobus (label 1), Ennomos (label 2) and 2001 UV209 (label 3) in the L5 population. The red lines are the CSS observations (solid are the data in phase II, dashed are the data in phase I), and the black line is the bias-corrected model with σ interval (gray zone). The blue line is the whole background population from the MPC catalog. The vertical dashed lines show the magnitude segments used for the representation of the background population (Table 3).

populations at the 12 mag limit imply the KS probabilities change to 2.5×10^{-4}, 0.20, and 0.35 for the *A, B,* and *C* distributions (see also wider σ regions, now basically overlapping in *B* and *C* cases). We therefore conclude that the L4 and L5 distributions in eccentricity and semimajor axis (or the libration amplitude) appear to be compatible with one another, while the distribution in inclination still appears to be statistically inconsistent. Here again we leave a more thorough analysis and a possible explanation for future studies.

Variants of the solution. We now explore the possibility of constraining the JT magnitude distributions beyond the limit $H = 15$ adopted in the nominal model. For the reasons discussed above, we will discard the L5 population and focus on observations from the L4 population. Keeping our nominal setup, we only add one more magnitude segment in the spline representation between 15 mag and 15.5 mag.

Figure 27 shows (i) the biased model compared to the differential magnitude distribution of the G96 observation in phases I and II, and (ii) the bias-corrected cumulative magnitude distribution for both the background and family components in the L4 cloud (compare with Figures 20 and 23). While visually the solution appears satisfactory to us, we believe it should be treated with caution. As expected from previous studies, beyond the 15 mag limit, the cumulative distribution becomes shallow. The local magnitude slope at $H = 15$ is now 0.30 ± 0.01, and at $H = 15.5$ becomes even 0.24 ± 0.02. Here we raise a flag of warning because the slope at $H = 15$ is not statistically compatible with that of the nominal model. Apparently, the `MultiNest` algorithm has decided to choose a very shallow slope at $H = 15.5$, and this affects the solution at $H = 15$ due to a rather small, half-a-magnitude last segment.


Figure 24. The local slope of the cumulative absolute magnitude distribution for the bias-corrected background population of L4 (red) and L5 (blue) Trojans. The gray zone is the σ interval of the solution. The vertical dashed line indicates the often-quoted break at $\simeq 9$ mag, delimiting the transition from a very steep distribution of larger Trojans to a shallower distribution of smaller Trojans. The horizontal dashed line at 0.44 slope is the characteristic value for $H > 9$ mag Trojans in the previous literature (see, e.g., Uehata et al. 2022). In the last segment of our solution, magnitude range 14–15, the slope of the L4 population becomes gradually shallower reaching $\simeq 0.38$ at $H = 15$ mag. The solution of the L5 population in the same magnitude segment is even shallower, but we consider it unreliable for reasons discussed in the main text.

The left panel in Figure 27 shows that beyond magnitude 15, the number of CSS detections becomes limited: only a few tens of detections in phase I and slightly more than 200 in phase II. In this situation, the fidelity of the detection probability determination is a critical element of the model. Figure 18 then
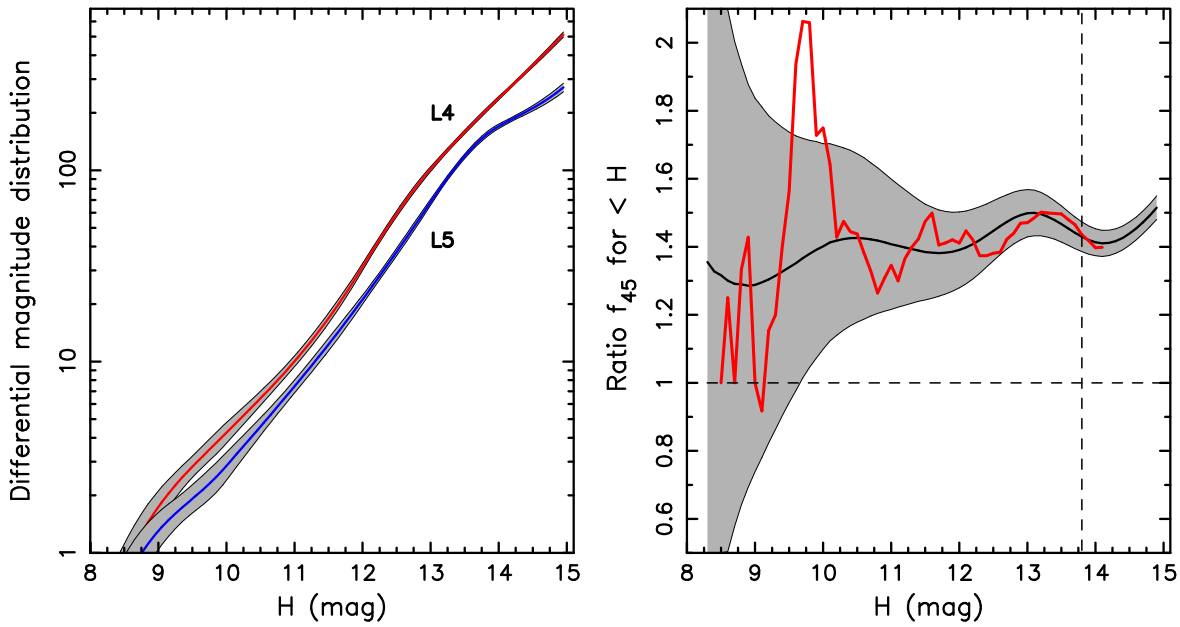
Figure 25. Left panel: differential magnitude distribution of the bias-corrected background Trojan populations: solid line is the median solution (red for L4 and blue for L5), and the gray zone is the σ uncertainty (0.1 mag bins wide). The Trojan populations in the families are not contributing. Right panel: the asymmetry factor $f_{45} = N_4/N_5$ of the L4 and L5 Jupiter Trojans. The background population counts N_4 and N_5 are (i) their respective cumulative values at a certain magnitude limit (the abscissa), and (ii) correspond to the bias-corrected background population in our model. The solid black line is the median value, and the gray area is the σ envelope from the 10,000 posterior solutions by MultiNest. The vertical dashed line is the approximate observational completeness to date. The solid red line is the ratio of the observed L4/L5 populations with the Trojans in families removed. Up to the completion limit, we expect this fraction to reside inside the uncertainty limits of the model. The group of the largest Trojans below magnitude $\simeq 9$–9.5 exhibit symmetry, since $f_{45} = 1$ is within the statistical uncertainty. Interestingly, the observed population fraction exceeds the σ interval of the model in the $\simeq 9.5$–10 range. This feature is due to the anomalous vacancy of the L5 Trojans in this magnitude range (see Figures 15 and 16). Trojan populations fainter than $\simeq 10$ deviate from symmetry, with the observed fraction returning to the σ interval of the model, and the statistical robustness increases with increasing H. At the approximate observational completeness limit, $H \simeq 13.8$, $f_{45} = 1.43 \pm 0.05$ (σ solution), with $f_{45} = 1$ excluded at $\simeq 7.9\sigma$ level.
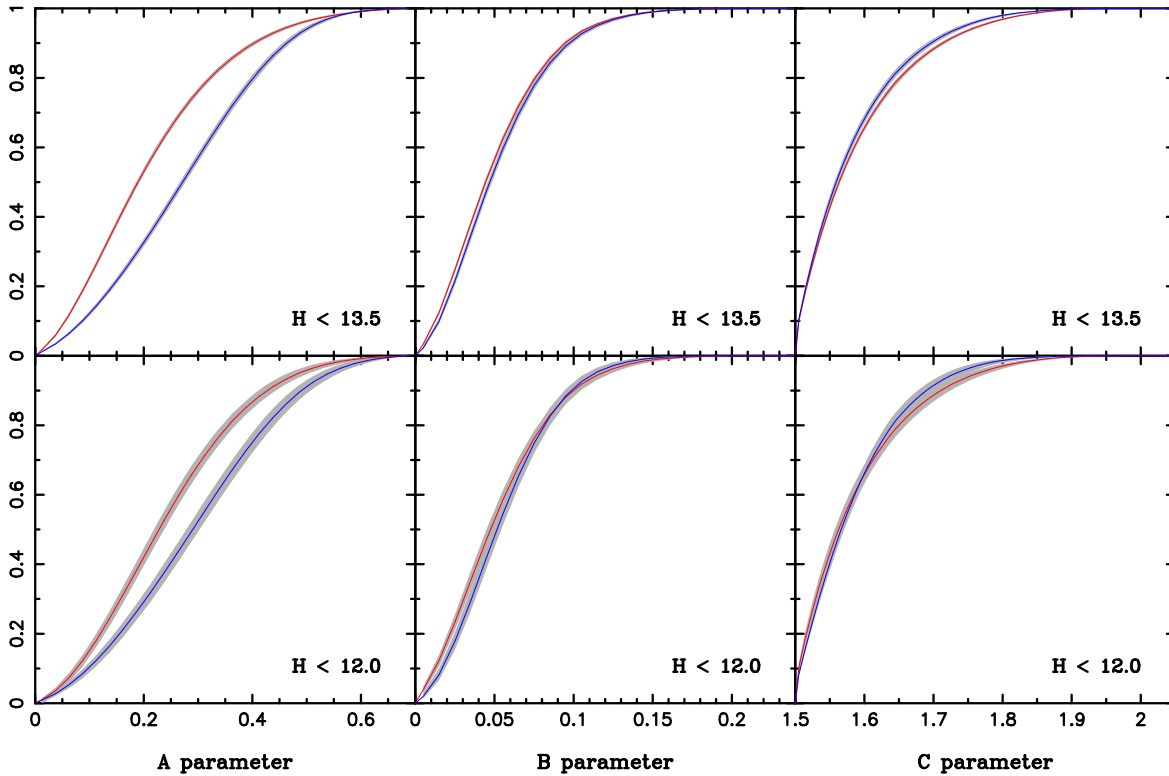
Figure 26. Cumulative distribution of the orbital parameters (A, B, C) (left to right) based on our biased-corrected solution of the Trojan background populations: L4 in red and L5 in blue. Because the model parameters of the faint L5 Trojans are not reliable enough, we use a maximum 13.5 mag limit in computing the upper plots; the lower plots provide the same information but for a population limited to absolute magnitude 12. The color-coded curves are the best-fit solution, and the gray region is a σ interval. The B and C distributions appear to be statistically identical, but the A (inclination) distribution is different.
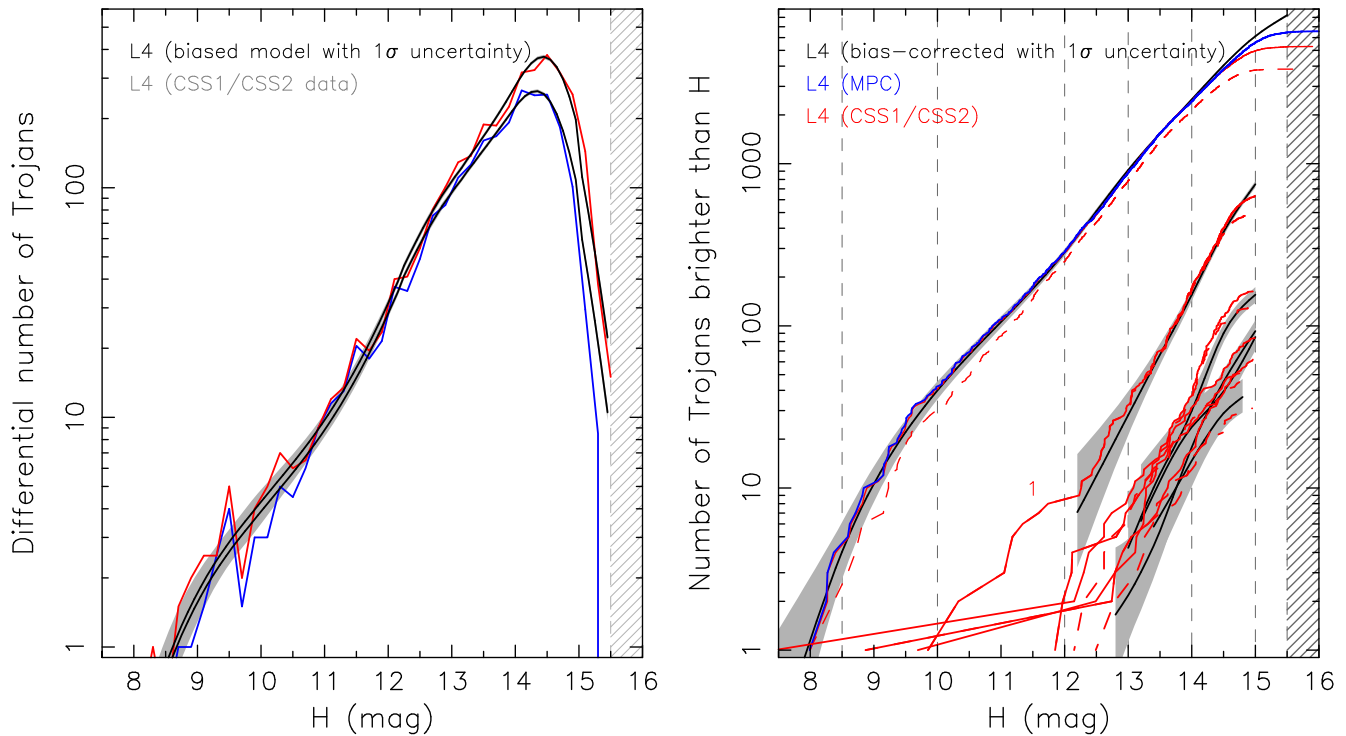
Figure 27. The solution of the L4 Trojan population using a model in which the maximum absolute magnitude has been extended to 15.5 (compare with the left panels in Figures 20 and 23). Left panel: Differential magnitude distribution of the G96 observations (blue for phase I and red for phase II) compared with the best-fitting biased model (black line with a σ interval depicted by the gray zone). Right panel: Bias-corrected cumulative magnitude distribution based on G96 observations. The background population, shown by the upper curves, is separated from the major families: (i) Eurybates (label 1), Arkesilaos, Hektor, Thronium, and Teucer. The red lines are the CSS observations (solid are the data in phase II, dashed are the data in phase I), and the black line is the bias-corrected model with σ interval (gray zone). The blue line is the whole background population from the MPC catalog. The vertical dashed lines show the magnitude segments used for the representation of the background population.

shows that the nominal probabilities are $\leqslant 0.3$ even in phase II (and 3 times smaller in phase I), where they depend on various details of the model. These could include more in-depth analysis of the detection probability at very low values of the apparent motion, phase function uncertainties, or further considerations about the choice of variables and detection probability computation (as an example, analysis in Appendix B allows us to consider our approach reasonable, but it could certainly be improved). For that reason, we hold a study of a very faint end of the Trojan population until further efforts have been made in the detection probability determination and more data has been acquired.

6. Conclusions

The main results of our work may be summarized as follows:

1. We developed a novel approach for the description of the orbital architecture and magnitude distribution of JT populations. The orbital part uses quasi-proper elements corresponding to the semimajor axis (or libration amplitude), eccentricity, and inclination. The model takes a simple averaging over the complementary three orbital angles. The orbital space is segmented into 38,500 bins. The probability density distribution used by the model in the orbital space is represented by a simple convolution of three 1D analytical functions, and the long-term stability zone is determined using numerical integration. The magnitude part is described by the cubic-spline representation of the cumulative distribution on six segments, and it is parsed to 80 mag bins. In addition

to the simultaneous analysis of the orbital and magnitude Trojan parameters, another novel aspect of or model is a separation of the Trojan population in clustered families and the smooth background.

2. The new determination of JT proper orbital elements and identification of Trojan families is a side result of our principal goal (see Appendix A). We find evidence of nine statistically robust families among L4 Trojans, and four statistically robust families among L5 Trojans. In the L5 population, we helped resolve the confusion that existed about the high-inclination Trojan clan (most often called the Ennomos family in the previous literature). Here we show it consists of two partially overlapping families with the largest members (1867) Deiphobus at a higher inclination and (4709) Ennomos at a lower inclination. This separation nicely matches the conclusions of Wong & Brown (2023) where multiband photometric observations are used to investigate members of the Ennomos–Deiphobus clan. The morphology of the L4 and L5 families is surprisingly different: the L4 families are sharp and highly concentrated clusters, with possibly very low populations of interlopers, while the L5 families are diffuse and broad clans, with possibly a substantial population of interlopers. The origin of this difference is unknown, but it possibly bears important clues about the past collisional evolution of these populations as well as their origin.

3. We applied our model to observations of CSS station G96 taken between 2013 January and 2022 June. More than 220,000 documented fields of view were well

characterized in terms of detection probability as a function of apparent magnitude and rate of motion. G96 camera upgrades in 2016 May made us split the survey period into phases I and II, which we consider as two independent surveys. During part I, G96 detected 4551 and 2460 individual JTs in the L4 and L5 populations. These numbers increased during part II to 6307 and 3041 individual JTs detected in the L4 and L5 populations. By 2022 June, G96 had detected more than 85% of the known populations in the two Trojan clouds. We developed a method to determine the detection probability defined over the orbital element and the absolute magnitude range used by our model. This probability is a convolution of the aforementioned detection probabilities within a given field of view and the probabilities that occur in any of the survey fields of view.

4. We applied the `MultiNest` code to determine which parameters within the model are needed to reach a maximum likelihood match to the CSS observations. This outcome leads to a suitably robust algorithm to tackle the multiparametric task with existing correlations. Conveniently, `MultiNest` also provides posterior distributions of the solved-for parameters, enabling us to evaluate the statistical significance of the model and its components.

5. Our results are in good agreement with previous inferences about the magnitude distribution of the Trojan population. Traditionally, a simple broken power-law model with one or two breakpoints has been used. Thanks to the cubic-spline representation of the magnitude distribution, our analysis is more detailed and shows evidence of fine variations of the slope exponent (e.g., a shallow local maximum between magnitudes 12 and 13; Figure 24). Between magnitudes 14.5 and 15, the power-law slope becomes shallower, reaching 0.38 ± 0.01 at $H = 15$. The available CSS observations of the L5 population are less numerous, making our ability to clearly separate the family populations less certain. For those reasons, the L5 solution should be considered less reliable beyond magnitude 14–14.5. We tried to extend the L4 population solution beyond $H = 15$, but the CSS data to date are insufficient to characterize the very faint end of the population.

6. Our results confirm the previously debated asymmetry in magnitude-limited populations of the L4 and L5 Trojans. However, unlike before, we evaluated the asymmetry measure using the background population of Trojans, objectively separating the population in the Trojan families. At magnitude $H = 15$ we find $f_{45} = N_4(<H)/N_5(<H) = 1.43 \pm 0.05$. The origin of this asymmetry is unknown. The end-member approach in this respect is to associate it with the possibility of a large-scale inward migration of Jupiter and in situ formation of Trojans (e.g., Pirani et al. 2019a, 2019b; there are, however, arguments against such a model, e.g., Deienno et al. 2022). While the effects of a more limited Jupiter migration (or a jump from Jupiter via an encounter with an ice giant) could play some role (e.g., Hou et al. 2016; Li et al. 2023a, 2023b), there are also additional possibilities, such as a slight albedo and/or shape irregularity difference between the small Trojans in the L4 and L5 populations (e.g., Section 5.2). The population asymmetry therefore requires further study in the future.

7. Our analysis suggests the possibility of an asymmetry in the orbital inclination of the JTs, with the L4 population having a tighter inclination distribution and the L5 population having a broader one. However, since the L5 population solution is less reliable (for the reasons mentioned above), we consider the inclination distribution asymmetry an interesting hypothesis that needs to be verified when problems of the L5 population modeling are improved in the future.

There were fewer and smaller magnitude-reaching observations of the Jupiter Trojan L5 population in the G96 data set between 2013 and 2022 (see Section 2). As a result, our ability to characterize this cloud was limited in this paper. The observational conditions of L5 populations significantly improved from the 2023 season, which is motivation to revisit our JT analysis in a few years' time. Continuing operations of CSS could provide the basis for this effort. They could be readily complemented with data from other, well-characterized surveys, such as the powerful Vera C. Rubin Observatory (e.g., Schwamb et al. 2023) or the upcoming NASA mission NEO Surveyor (e.g., Mainzer et al. 2021).

Appendix A
## New Catalog of Trojan Proper Elements and Identification of the Families

Our approach to determining proper elements of JTs closely follows the synthetic theory of Milani (1993; see also technical steps outlined in Appendix A of Holt et al. 2020a) and applies it to the currently known population of objects.[12] In this case, we used the MPC catalog of minor planet orbits as of 2023 April 15, containing about 1,275,000 entries, and selected JTs using the same steps as described in Section 2. We obtained 8,144 orbits in the L4 swarm and 4252 orbits in the L5 swarm. The slight increase with respect to the numbers given in Section 2 reflects (i) partly the new detections during the spring of 2023 but, more importantly, (ii) the fact that now we did not drop the orbits with short observation arcs (except the really poorly determined ones with arcs less than a few days).

Figure 28 shows a projection of the Trojan proper elements onto the (da_P, e_P) and $(da_P, \sin I_P)$ planes. The principal features to be noticed include (i) the correlation between the

---

[12] For the sake of brevity, we thus relegate an interested reader to Milani (1993) and Holt et al. (2020a) to learn about technical details, while here we discuss the results. The final products, namely (i) the catalog of the Trojan proper elements, and (ii) identification of the Trojan families, are available at https://sirrah.troja.mff.cuni.cz/~mira/tmp/trojans/.
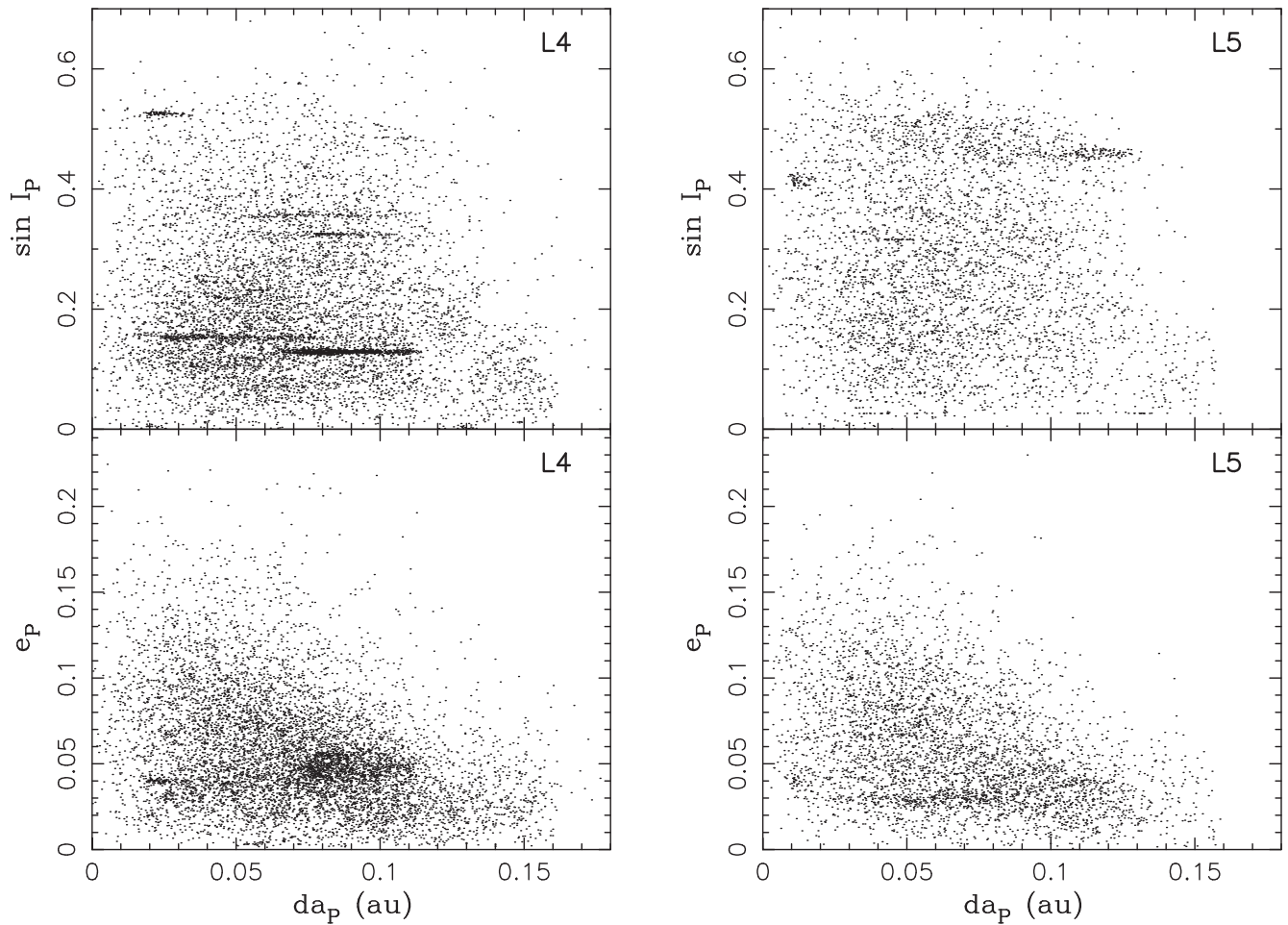
Figure 28. The newly determined proper elements of L4 (left) and L5 (right) Jupiter Trojans with the input orbital information as of April 2023. The top panels show a projection onto the da_P vs. $\sin I_P$ plane, and the bottom panels show a projection onto the da_P vs. e_P plane. Distinct clusters, especially among the L4 Trojans, are the subject of our analysis, resulting in a new catalog of the Trojan families.
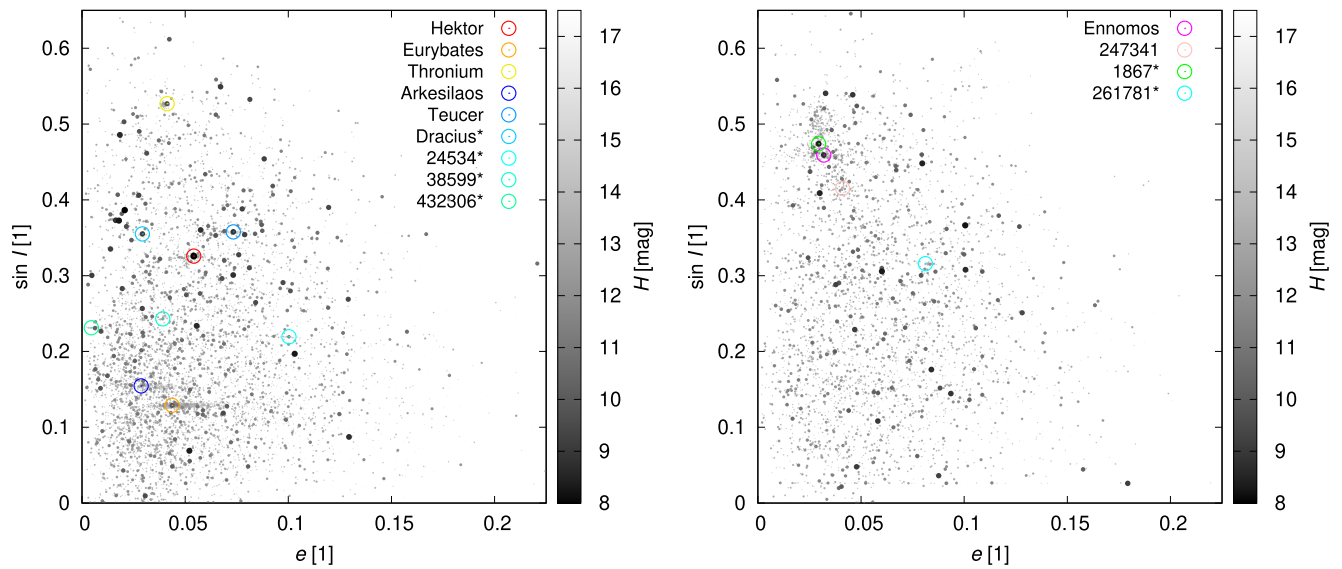
Figure 29. Trojan families highlighted in the plane of the proper eccentricity e_P and the proper sine of inclination $\sin i_P$ (compare with the rightmost panel in Figure 11); the objects librating about the leading point L4 on the left panel, those librating about the trailing point L5 on the right panel. The scale of gray and the size of the symbols are proportional to the absolute magnitude H (see the vertical bar). The family location is indicated by the largest remnant (color-coded open circles and labels); the newly discovered families are identified by the asterisk (*).

Table 4
Statistically Significant Families in the L4 and L5 Trojan Populations
Determined Using the HCM and Our New Catalog of Synthetic Proper
Elements

Number	Designation	v_{cutoff} (m s^{-1})	N_{mem}	D_{LR} (km)	D_{LF} (km)	D_{Durda} (km)
Families in the L4 cloud						
624	Hektor[a]	40	118	230	21	250
3548	Eurybates	40	875	68	53	140
9799	Thronium	20	69	72	22	120
20961	Arkesilaos[b]	40	235	23	21	110
2797	Teucer[c]	60	86	113	17	130
4489*	Dracius	60	24	95	15	
24534*	2001 CX27	60	45	29	15	
38599*	1999 XC210	60	22	20	12	
432306*	2009 SQ357[d]	40	24	7.3	6.8	
Families in the L5 cloud						
4709	Ennomos[e]	50	88	80	20	110
1867*	Deiphobus[e]	60	233	131	24	180
247341	2001 UV209[f]	55	46	18	16	90?
261781*	2006 BG132[g]	60	31	14	13	

Notes. Newly discovered clusters are indicated by asterisk symbols (*). The number and designation correspond to the central body, v_{cutoff} is the velocity cutoff used in the HCM identification, N_{mem} is the number of associated members, D_{LR} is the size of the largest remnant, D_{LF} is the size of the largest fragment, and D_{Durda} is the size of the parent body estimated using the method of Durda et al. (2007).
[a] Alternatively, only a tight cluster of small bodies at the HCM velocity of 20 m s^{-1} around (624) Hektor.
[b] Vinogradova (2020) opted to associate this cluster to (2148) Epeios, formerly also by Beaugé & Roig (2001).
[c] Identified by Vinogradova (2015), formerly also by Milani (1993).
[d] This cluster contains only small objects; large Trojans (4035) Thestor and (6545) Leitus are nearby but offset in a proper semimajor axis (see also Figure 30).
[e] The earlier studies (e.g., Brož & Rozehnal 2011; Rozehnal et al. 2016) had Ennomos as a single large but diffuse and spectrally controversial family candidate in the L5 cloud. Vinogradova (2020) associated this cluster with (1867) Deiphobus. We propose the former Ennomos cluster consists of two overlapping families associated with (4709) Ennomos and (1867) Deiphobus's largest objects; this is also nicely supported by the detailed color analysis in Wong & Brown (2023).
[f] This family has been associated with (37519) Amphios in Vinogradova (2020), but (247341) 2001 UV209 resides closer to the family center.
[g] Vinogradova (2020) mentions a cluster around (1172) Aneas, which is close to this cluster but offset in the proper eccentricity.

maximum proper eccentricity and da_{P}, which has been known since the works of E. Rabe (see, e.g., Rabe 1965, 1967; Levison et al. 1997; see also Figures 12 and 13), and (ii) statistically distinct orbital clusters, principally among the L4 population. In order to characterize the latter in a quantitative way, we follow the traditional steps (see, e.g., Milani 1993; Beaugé & Roig 2001). First, we adopt the d_3 metrics to define distances of the orbits in the proper elements space, and we use the hierarchical clustering method (HCM) to discern these principal families in the population. Our results confirm and extend those in Brož & Rozehnal (2011), Rozehnal et al. (2016), Vinogradova (2019), and Vinogradova (2020). In particular, we identify the previously known families and extend their membership toward Trojans with smaller sizes (obviously, this is the harvest of the powerful sky surveys from the last several years). Additionally, we see evidence for new, previously unknown families (see Table 4 for a summarizing information). Figure 29 highlights the location of the identified

families in the projection onto the proper element (e_{P}, $\sin I_{\text{P}}$) plane, suitable for their visualization (this is because they are often most extended in the da_{P} coordinate—or the libration amplitude—which is the least stable of the proper elements). Pushing the knowledge of membership in Trojan families toward smaller objects provides important hints about their contribution to the total Trojan population as a function of the absolute magnitude. As already mentioned in the main text, we selected the prominent families in each of the Trojan swarms and remapped their location from the proper element space to the space of (A, B, C) orbital parameters (see data in Table 1).

In what follows, we provide a brief overview of the novel findings about the Trojan families. Similarly to the case of the total observed populations, the gradual increase in the asymmetry of the Trojan families among the L4 and L5 swarms arose during the recent decade. Here we report nine cases in the L4 population versus only four in the L5 population. Additionally, their morphology seems different: sharp and concentrated families among the L4 Trojans versus rather broad and diffuse families among the L5 Trojans.

The Eurybates family in the L4 cloud remains the most pronounced of them, representing more than $\simeq 10\%$ of the population at magnitude $H \simeq 14.5$. This is because, as shown in Figure 16, the Eurybates family magnitude distribution keeps to be steeper than the background population until that magnitude limit. Rozehnal et al. (2016) paid close attention to a broad cluster of Trojans about the historically third discovered Trojan object (624) Hektor (e.g., Strömgren 1907; Wolf & Kopff 1907; Wolf 1907). Their motivation was multiple: (i) Hektor has a satellite, possibly formed along with the family; (ii) Hektor, and a few smaller fragments, have a rare D-type taxonomy among the asteroid families; and (iii) Hektor family was the second most populous at the time. Here, we find that the newly discovered small Trojans in the Hektor family zone preferentially occupy an immediate vicinity of the largest fragment, constituting thus its dense core. It is not clear whether this structure follows from the original family formation event, or if it arises from a secondary cratering on (624) Hektor more recently. Further studies of this interesting cluster are warranted. New data about the Arkesilaos family's small members continue the trend of a steep size distribution predicted in Rozehnal et al. (2016). In our identification, it is already the second most populous cluster in the L4 swarm (see also Figure 16). When plainly extrapolated to even smaller fragments, this family may rival the Eurybates family at $H \simeq (16.5-17)$. Finally, the cluster about the L4 Trojan (9799) 1996 RJ, first discovered by Brož & Rozehnal (2011), remains one of the fairly distinct families (the low background population at its very high inclination helps its identification). Because this object obtained a final designation, we call it the Thronium family.

Brož & Rozehnal (2011) reported a discovery of a broad cluster of L5 Trojans about the largest object (4709) Ennomos. Yet, its diffuse nature and spectral/albedo peculiarity immediately raised questions about its legitimacy and the interloper density. They have been recently carefully tested by dedicated broadband photometric observations of Wong & Brown (2023). These authors found that many of the proposed members in the Ennomos family are spectrally indistinguishable from the overall background population, except for a limited number of Trojans in the Ennomos vicinity. Vinogradova (2020), also observing the extended nature of this cluster,
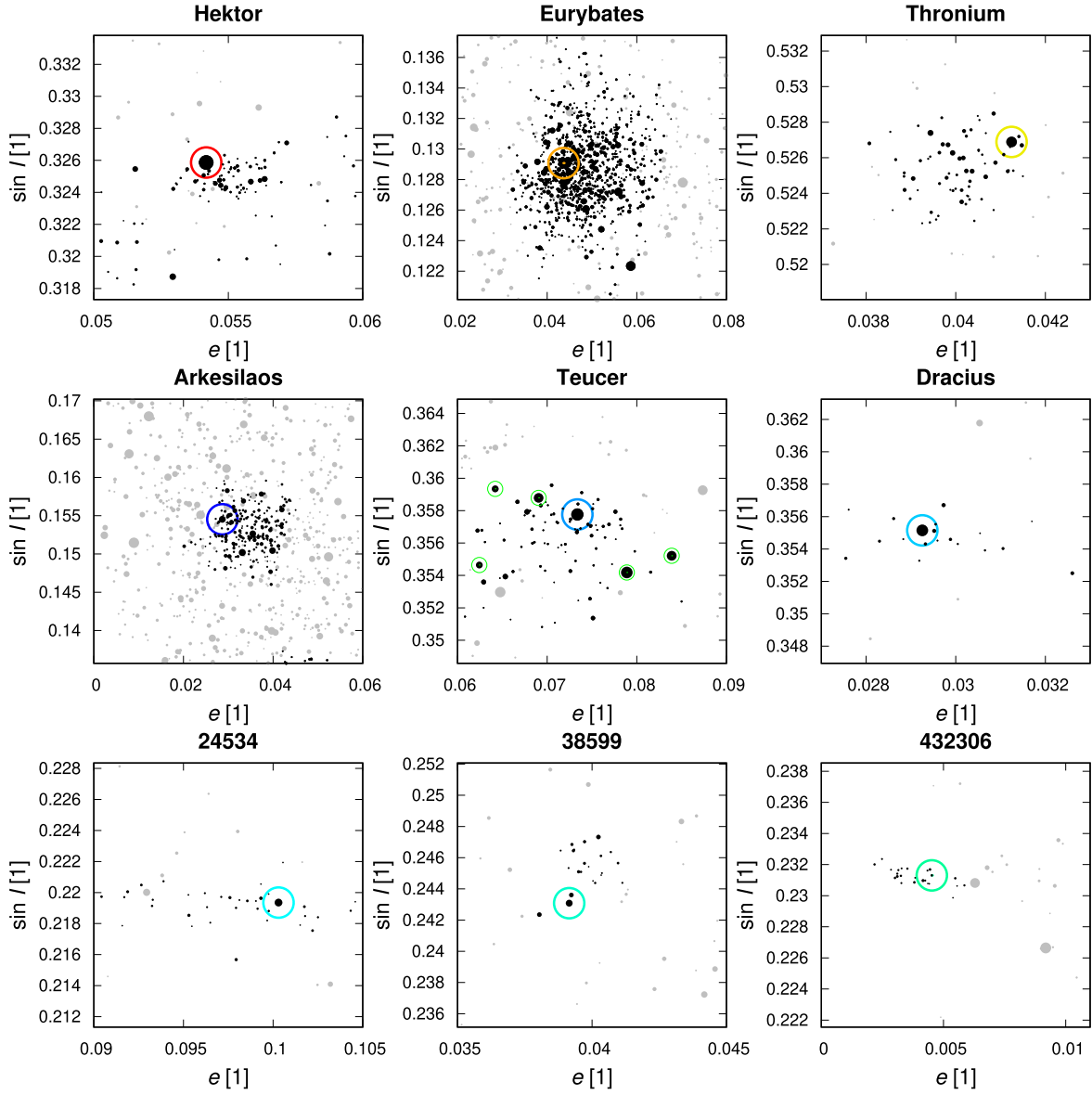
Figure 30. The same as Figure 29 (left panel), but now zoomed on the individual families among the L4 Trojans. The family members are black (the symbol size proportional to the physical size of the body), non-members projecting onto the same (e_P, $\sin I_P$) zone (but having offset the da_P third coordinate) are shown in gray. The family identification is at the top label, and the position of the largest remnant is highlighted by the open circle. The low-inclination families ($\sin I_P < 0.2$) are typically resolved by having a large population of members, and the high-inclination ones may be resolved more easily because of the low background population of Trojans. In the case of the Hektor family (top and right panel), we show its dense core consisting of only very small fragments, while previous studies considered its more extended version (e.g., Rozehnal et al. 2016).

took the liberty to associate it with another large L5 Trojan (1867) Deiphobus. Our results support this shifting point of view, or rather make it more accurate. When picking Ennomos and Deiphobus as the largest remnants in their respective families, we observe that they keep distinct at small HCM v_{cutoff} velocities and merge only when they exceed 60 m s^{-1}. The Ennomos family occupies a smaller $\sin i_P$ and larger e_P zone, and the Deiphobus family extends to a higher $\sin i_P$ zone (Figure 31). Additionally, the Ennomos part is more concentrated at a larger libration amplitude (or da_P), helping it separate from the Deiphobus part at a smaller libration amplitude in the 3D proper element space. This nicely matches the results of the photometric observations of Wong & Brown (2023).

The newly discovered families are typically compact clusters with a limited number of known and small Trojans. See, for instance, families about (38599) 1999 XC210 or (432306) 2009 SQ357 in the L4 swarm, or the family about (261781) 2006 BG132 in the L5 swarm (Figures 30 and 31).

It is interesting to compare the architecture of the Trojan orbits in the space of proper orbital elements described above to that described by the "quasi-proper" variables (A, B, C). This is similar to Figure 11, but here it allows a more direct correspondence to Figure 28– we use $da_P(C) = a_J\sqrt{8\mu(C-1.5)/3}$ to replace C. The result is shown in Figure 32. While the proper elements are certainly more accurate quasi-integrals of motion, we note that Trojan representation in the space of (A, B, C) parameters captures are important features of the population. Most importantly, Trojan families are very well reproduced in these simplified variables. This justifies their applicability for the population debiasing efforts.
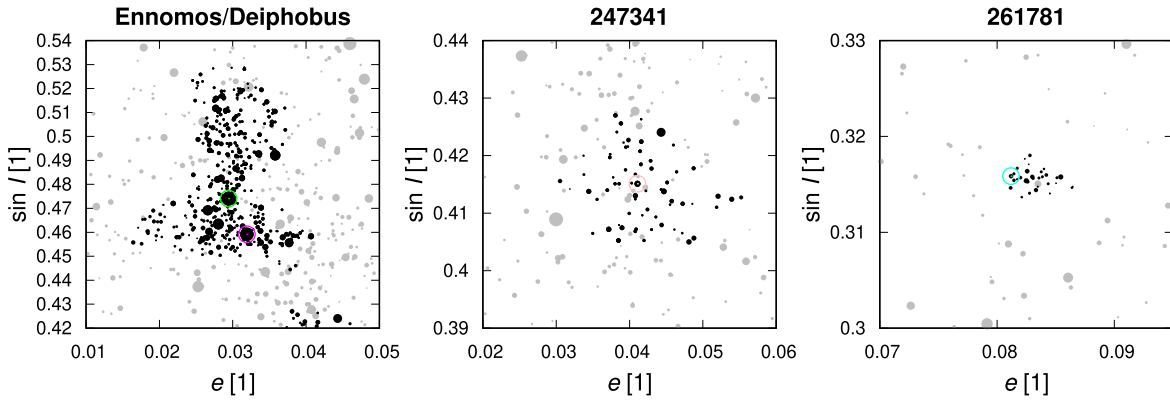
Figure 31. The same as in Figure 30, but now for the three families identified among the L5 Trojans. We argue that the former Ennomos family, shown on the leftmost panel, is in fact composed of two overlapping families: (i) Ennomos, at the right bottom corner, and (ii) Deiphobus, extending toward the high inclinations.
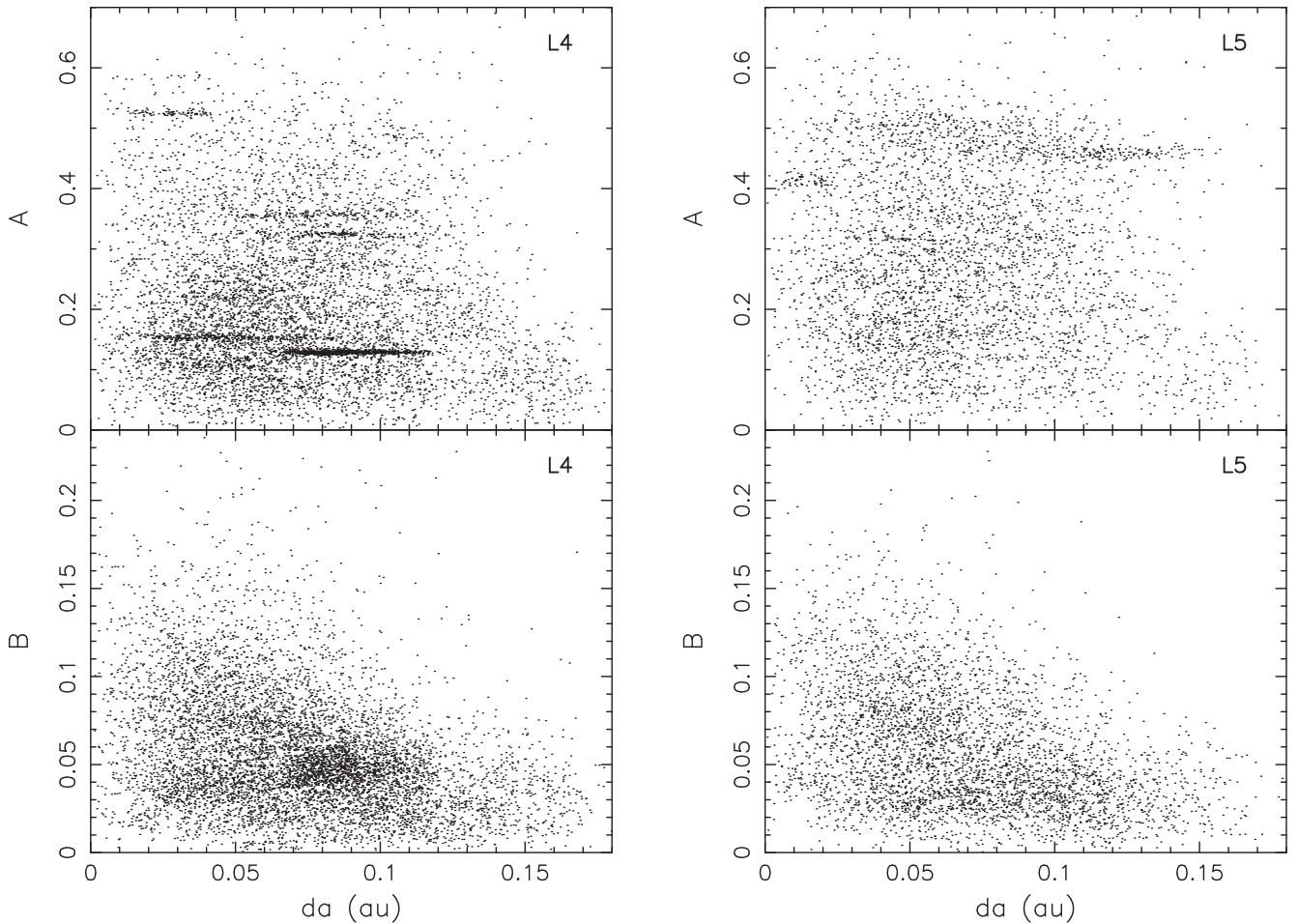
Figure 32. Population of L4 (left) and L5 (right) Jupiter Trojans from the MPC catalog (as of 2023 February 22) projected onto the "quasi-proper" elements used in our debiasing procedure: (i) $da_{\rm P}(C) = a_{\rm J}\sqrt{8\mu(C-1.5)/3}$ vs. A (top), and (ii) $da_{\rm P}(C) = a_{\rm J}\sqrt{8\mu(C-1.5)/3}$ vs. B (bottom). While these variables are much simpler than the true proper elements, they provide a picture nearly as accurate (compare with Figure 28).

Appendix B
Inferences of the Detection Bias from the Observations

Following the information in Section 2, we provide a few more examples of the observation biases affecting Trojan detections by CSS that need to be accounted for and removed when estimating the complete populations near L4 and L5 libration centers. We also test our formulation of the detection probability $\mathcal{P}(A, B, C; H)$ introduced in Section 4.1, seeking

justification for averaging over the proper angle ψ associated with the eccentricity parameter B.

Figures 33 and 34 show the angular difference between the longitude in orbit λ of the Trojan and the longitude in orbit $\lambda_{\rm Earth}$ of the Earth at the epoch of detection for the L4- and L5 swarm objects by CSS during phase II (2016 May 31–2022 June 15). The opposition geometry has $\lambda - \lambda_{\rm Earth} \simeq 0$ (neglecting Trojan's orbital inclination), while positive/negative values of the
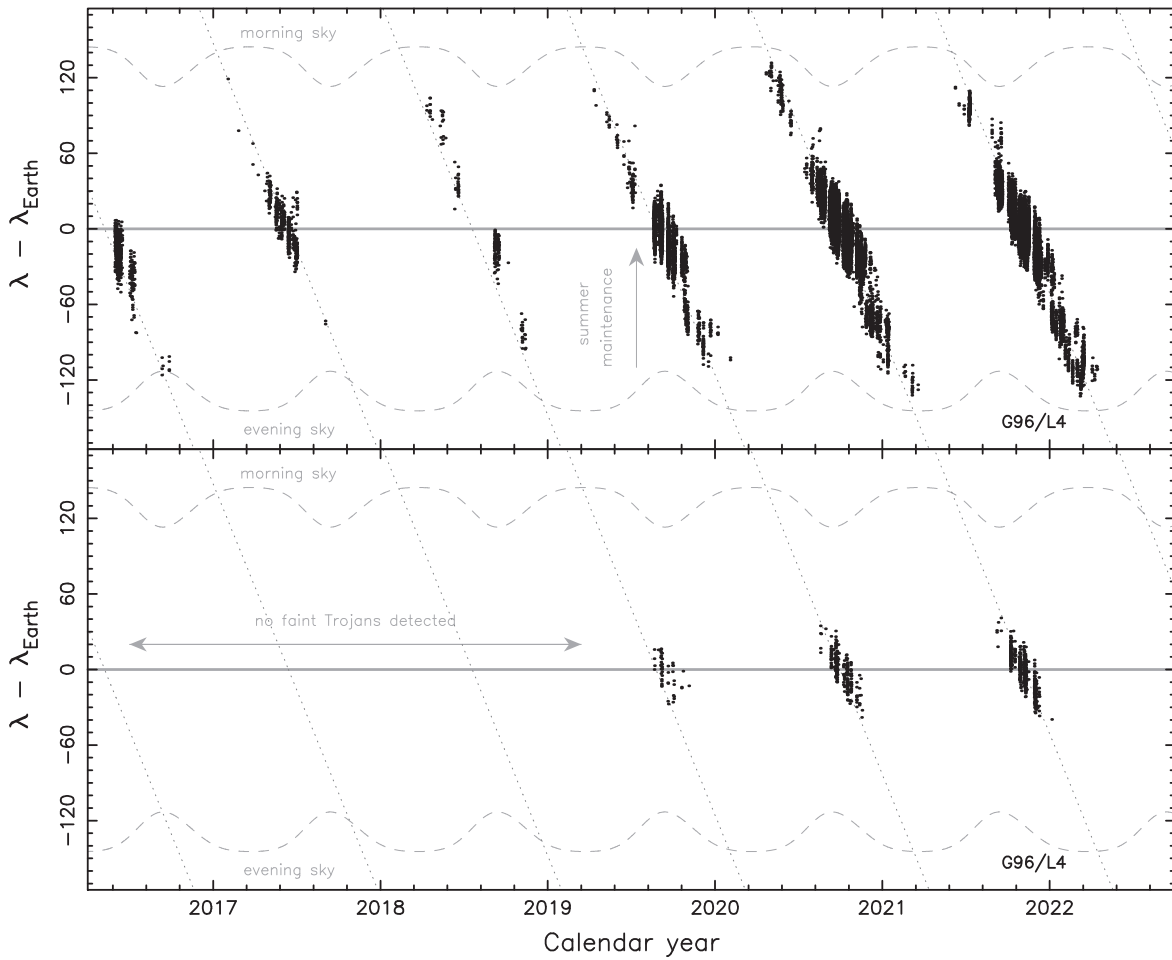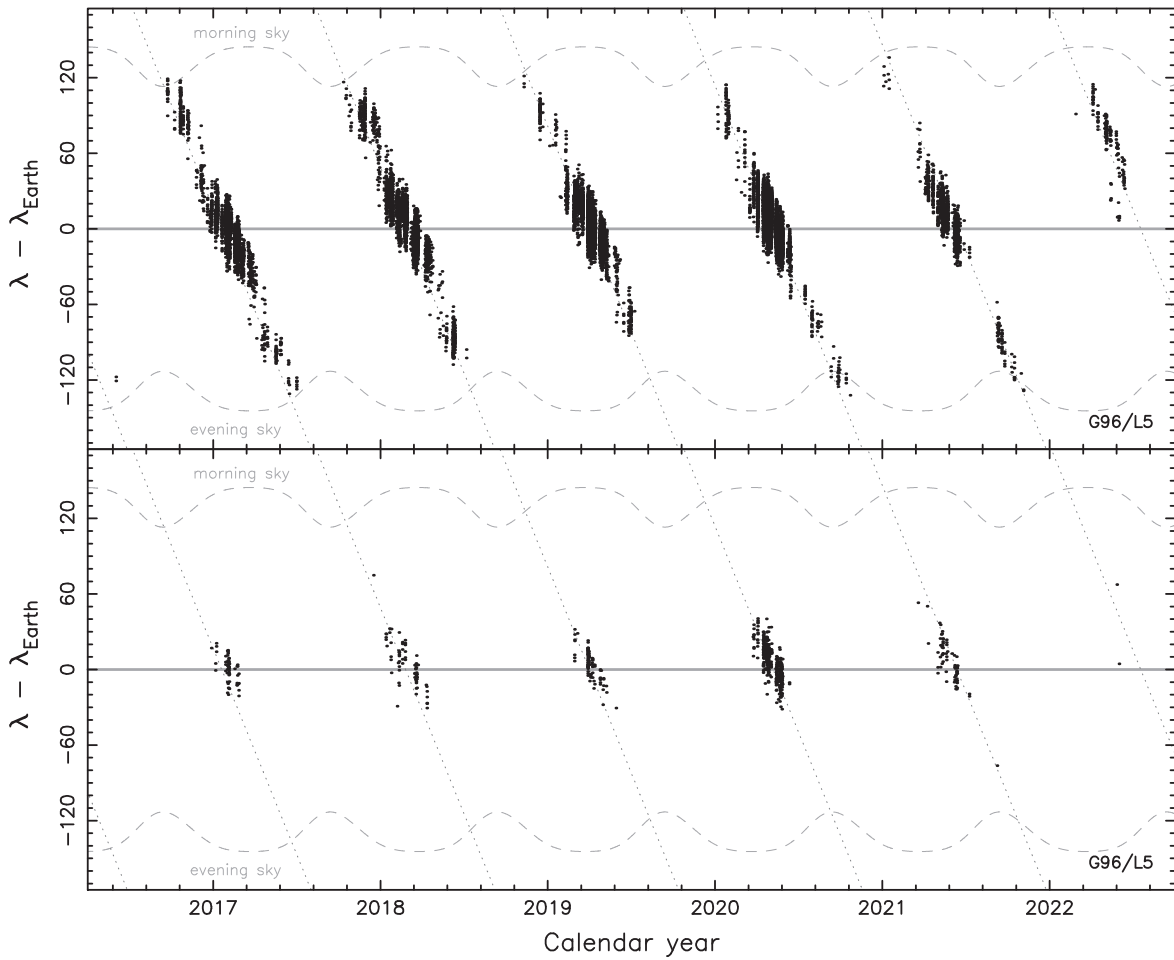
Figure 33. Detections of the L4 Trojans during phase II of the CSS observations (calendar date at the abscissa; see also Figure 4). The ordinate shows the Trojan ecliptic longitude λ referred to as the ecliptic longitude of the Earth λ_{Earth} at the moment of detection. The upper panel is for $H \leqslant 14$ Trojans (population of large and bright objects), and the lower panel is for $H \geqslant 15$ Trojans (population of small and faint objects). The dashed curves are the extremal configurations defined by (i) the Sun being $10°$ below the local horizon, (ii) the Trojan being at the ecliptic and $15°$ above the local horizon (the cyclic nature is due to longer nights as well as the higher maximum position of the ecliptic above the horizon in winter). At each season, the Trojans start to be observable in the extreme morning sky, and over a period of little less than a year, they move to the extreme evening sky. This is due to the Earth's faster mean motion about the Sun, such that the L4 swarm near Jupiter's libration center is being caught by the Earth-bound observed; the dotted line has the relevant synodic frequency $n - n_J$. The scatter of detections in $\lambda - \lambda_{Earth}$ at any given moment corresponds to Trojans at different libration amplitudes about L4. A combination of geometric, CSS-operation-dependent, and photometric selection effects impact detections. Bright Trojans are detectable during the whole season unless a galactic plane interferes (pre-2019 observations; see Figures 3 and 4) or the observations are interrupted by summer maintenance (see the example in 2019 shown by the arrow). Faint objects are observed selectively near the opposition ($\lambda \simeq \lambda_{Earth}$), which decreases their apparent magnitude in both factors on the right-hand side of Equation (23): (i) the product $R\Delta$ is minimum, as well as (ii) the magnitude-phase correction $P(\alpha)$. Due to the galactic-plane disturbance, no faint Trojans near L4 were detected during phase II until the opposition in late 2019.

difference shift the detection toward the morning/evening sky of the night. Detections proceed in "seasons," with the first objects in the swarm being detected on the extreme morning sky and drifting toward the extreme evening sky during nearly a year interval. They are affected not only by the galactic-plane interference (Figures 3 and 4), but also by practical aspects of the CSS operations. For instance, system maintenance is typically scheduled in summer, and this produces a gap in the observations (see the summer interruptions in detections of even the bright Trojans on the top panels of Figures 33 and 34). Small Trojans, which naturally appear faint, are detected only during the opposition (bottom panels). This helps to overcome the detection bar set by the limiting apparent magnitude on the image ($\leqslant 21.5$ typically), by minimizing magnitude-phase correction on the right-hand side of Equation (23). All the effects of the viewing geometry and CSS operations are presumably correctly accounted for in our determination of the detection probability $\mathcal{P}$

(Section 4.1). However, the photometric limit-related issues are slightly more delicate and warrant further testing.

This is because in determination of $\mathcal{P}$ we downgraded the full dependence on all orbital elements to only three "quasi-proper elements" (A, B, C), thus $\mathcal{P}(A, B, C; H)$. The fully detailed detection probability has been averaged over the associated "quasi-proper angles" (ϕ, ψ, θ) (Section 4.1). Consulting the statistics of the detected Trojans of different absolute magnitude H reveals that the averaging over ϕ and θ angles are well justified. The case of the ψ angle, associated with the eccentricity B, is slightly more tricky and requires a numerical check.

Figure 35 shows L4 swarm Trojans detected by CSS from 2021 April to 2022 April (the last season shown in Figure 33). During this period of time, the galactic latitude of the detected Trojans was large, such that no losses due to dense stellar fields near the galactic plane occurred (Figures 3 and 4). The summer

Figure 34. The same as in Figure 33, but now for the L5 Trojans. The upper panel is for detections of the $H \leqslant 14$ Trojans, and the lower panel is for detections of the $H > 14.5$ Trojans.
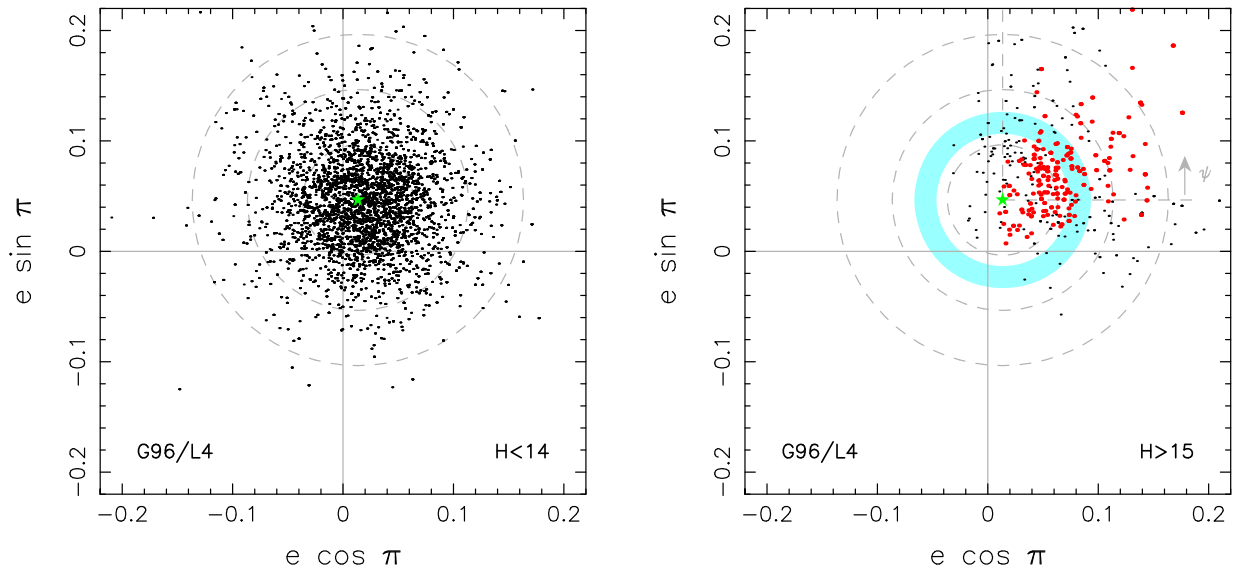
Figure 35. Trojans in the L4 swarm detected by the CSS in the 2021 April and 2022 April seasons (see Figures 4 and 33), projected on the plane of osculating nonsingular elements ($e \cos \varpi$, $e \sin \varpi$). The left panel is for bright objects with $H < 14$, and the right panel is for faint objects with $H > 15$. The green star is the forced center of the quasi-proper elements (B, ψ), namely at e_J polar distance from the center and polar angle $60° + \varpi_J$ (Equation (2)); several constant B circles are shown for the sake of illustration. The bright objects are distributed symmetrically about the forced center. The faint objects are mostly detected in the first quadrant, though clearly their complete population should follow the symmetric distribution shown by the bright objects. The symbols on the right panel are colored in red when the detection occurred at a 20° angular distance from the pericenter; this is the case for nearly all detected faint objects. The light blue annulus depicts $B \in (0.06, 0.08)$ interval of values that we have chosen for testing the validity of the detection probability $\mathcal{P}(A, B, C; H)$ averaging over the polar angle ψ (defined from the shifted axis as shown by the arrow).
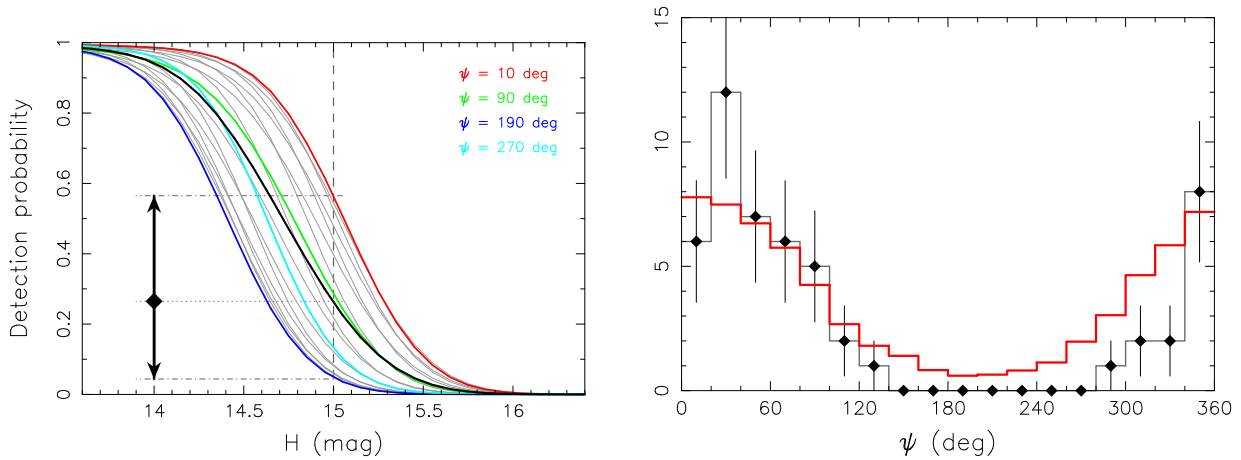
Figure 36. Left panel: detection probability of L4 Trojans in the quasi-proper orbital element bin defined by (i) $A \in (0.2, 0.225)$, (ii) $B \in (0.06, 0.08)$, and (iii) $C \in (1.58, 1.60)$. Here we use only CCS observations between 2021 April and 2022 April. The bold black line is the ψ-averaged detection probability $\mathcal{P}_{\mathrm{ave}} = \mathcal{P}(A, B, C; H)$, and the gray curves show the ψ-resolved detection probabilities $\mathcal{P}_i$ in 20° wide bins. Four individual values are color-highlighted. At $H = 15$ mag, the minimum and maximum detection probabilities $\mathcal{P}_i$ are more than 1 order of magnitude different (see the arrow). The diamond symbol is the $\mathcal{P}_{\mathrm{ave}}$ value. Right panel: the appropriately scaled $\mathcal{P}_i$ values (red histogram), compared to the actual number N_i of detected Trojans in the (B, ψ) annulus with $B \in (0.06, 0.08)$, but all (A, φ, C, θ) values (in order to increase statistics); for simplicity, the N_i are assumed to have $\sqrt{N_i}$ uncertainties shown by vertical intervals.

maintenance interruption affected only a small portion of the possible detections on the morning sky, such that the conditions are favorable to test the remaining photometric effects. The left panel in Figure 35 shows the position of the detected large Trojans, namely those with $H < 14$ mag. Their distribution in the plane of osculating heliocentric elements $(e \cos \varpi, e \sin \varpi)$ is fairly symmetrically distributed about the origin shifted to $(e_J \cos(\pi/3 + \varpi_J), e_J \sin(\pi/3 + \varpi_J))$ (this is the principal forcing effect by Jupiter; Equation (2)). When switching to the population of small L4 Trojans, with $H > 15$ mag on the right panel of Figure 35, things are different. Objects are preferentially detected only in the first quadrant characterized by $\varpi \in (0, \pi/2)$. Obviously, this only means that the complementary objects on different values of ϖ were not detected, and we need to check that the proposed simplified scheme for $\mathcal{P}(A, B, C; H)$ describes the situation correctly.

Inquiring a little more about the parameters of the detected faint Trojans, we analyzed the phase of their heliocentric motion at the detection epoch. In particular, we color coded in red those Trojans, whose mean anomaly M was less than 20° from the perihelion. As suspected, most of the detections of the large-H Trojans occur when they are near perihelion (i.e., $\lambda \simeq \varpi$). From the bottom panel in Figure 33 we already know that they are also detected near opposition (i.e., $\lambda \simeq \lambda_{\mathrm{Earth}}$). Combining both conditions together, we obtain $\varpi \simeq \lambda_{\mathrm{Earth}} \simeq 50°$ in the middle of the 2021 season, and this is where we see them. What is special about both conditions? They both help minimize the apparent magnitude m of the Trojan on the image by making both the second and the third terms on the right-hand side of Pogson's relation Equation (23) as small as possible: (i) the opposition and perihelion geometry make both R and Δ small, and (ii) the opposition geometry makes the magnitude-phase correction $P(\alpha)$ small as well. These are the optimum conditions, and the smallest detectable Trojans require this situation to occur.

In order to proceed quantitatively, we selected the following bin of the quasi-proper elements: (i) $A \in (0.2, 0.225)$, (ii) $B \in (0.06, 0.08)$, and (iii) $C \in (1.58, 1.60)$. This is still a fairly stable Trojan configuration (Figure 12), and in A and C parameters, quite representative of the population. When

determining $\mathcal{P}$ we averaged over ϕ (associated with A) and θ (associated with C). In the case of ψ angle, we proceeded as follows. First, we determined the proposed $\mathcal{P}_{\mathrm{ave}} = \mathcal{P}(A, B, C; H)$ by averaging over ψ too. This is the approach we use for debiasing the Trojan population in this paper. In order to check its validity, we next evaluated $\mathcal{P}$ using an extended formulation, where ψ angle has also been explicitly considered, thus $\mathcal{P}(A, B, C, \psi; H)$, and we used 20° bins in ψ. The bin indexed i has $\psi = \psi_i \in [(i-1)20°, i\,20°]$, and we denote the locally evaluated detection probability $\mathcal{P}_i = \mathcal{P}(A, B, C, \psi_i; H)$. The left panel in Figure 36 shows the individual $\mathcal{P}_i$ values as a function of H, highlighting those in the bins with $i = 1$ ($\psi \in (0°, 20°)$), $i = 5$ ($\psi \in (80°, 100°)$), $i = 10$ ($\psi \in (180°, 200°)$), and $i = 14$ ($\psi \in (260°, 280°)$). For the sake of comparison, we also show the averaged probability $\mathcal{P}_{\mathrm{ave}}$. At absolute magnitude $\simeq 13.75$, all probabilities are basically unity, indicating these are bright enough objects to be detected. At absolute magnitude $\simeq 16.1$, all probabilities are basically zero, indicating these are too faint objects to be detected. The interesting transition values are at $H \simeq 15$. The maximum $\mathcal{P}_i$ values for small ψ angles reach $\simeq 0.68$, while the minimum $\mathcal{P}_i$ values at about $\psi = 190°$ as $\simeq 0.06$. This is more than a magnitude difference, indicating that even these small Trojans may be detected if $\psi \simeq 10°$, but they are unlikely to be detected if $\psi \simeq 190°$. The averaged $\mathcal{P}_{\mathrm{ave}} \simeq 0.27$ is intermediate. This is the qualitative picture we get from the right panel in Figure 35. The right panel in Figure 36 makes this comparison quantitative. Here we show N_i, namely the number of Trojans in the ψ_i bin, and compare it with appropriately scaled $\mathcal{P}_i$ detection probability in each of the bins (red histogram). While the observed population in this particular bin is already low, such that the distribution of N_i is subject to considerable fluctuations,[13] the trend is reasonably well explained by the distribution of $\mathcal{P}_i$. Moreover, if we define $\mathcal{P}_{\mathrm{eff}} = (\sum_i N_i)/(\sum_i N_i/\mathcal{P}_i)$, an effective detection probability for Trojans in the tested blue annulus in Figure 35, we obtain

---

[13] We also consider $H > 15$ Trojans having all possible (A, φ, C, θ) values in the chosen annulus in B and different ψ bins. This is because the number of detections of such faint Trojans is already low.

$\mathcal{P}_{\text{eff}} = 0.40^{+0.07}_{-0.24}$. This compares reasonably well with the averaged $\mathcal{P}_{\text{ave}} = 0.27$.

ORCID iDs

David Vokrouhlický ⓘ https://orcid.org/0000-0002-6034-5452
David Nesvorný ⓘ https://orcid.org/0000-0002-4547-4301
Miroslav Brož ⓘ https://orcid.org/0000-0003-2763-1411
William F. Bottke ⓘ https://orcid.org/0000-0002-1804-7814
Rogerio Deienno ⓘ https://orcid.org/0000-0001-6730-7857

References

Beaugé, C., & Roig, F. 2001, Icar, 153, 391
Bien, R., & Schubart, J. 1987, A&A, 175, 292
Bottke, W. F., Vokrouhlický, D., Marschall, R., et al. 2023, PSJ, 4, 168
Bowell, E., Hapke, B., Domingue, D., et al. 1989, in Asteroids II, ed. R. P. Binzel, T. Gehrels, & M. S. Matthews (Tucson, AZ: Univ. Arizona Press), 524
Brož, M., & Rozehnal, J 2011, MNRAS, 414, 565
Buie, M. W., Keeney, B. A., Strauss, R. H., et al. 2021, PSJ, 2, 202
Buie, M. W., Zangari, A. M., Marchi, S., Levison, H. F., & Mottola, S. 2018, AJ, 155, 245
Chang, C.-K., Chen, Y.-T., Fraser, W. C., et al. 2021, PSJ, 2, 191
Christensen, E., Africano, B., Farneth, G., et al. 2019, EPSC-DPS Joint Meeting 2019, Vol. 2019, EPSC–DPS2019–1912
Degewij, J., & van Houten, C. J. 1979, in Asteroids , ed. T. Gehrels & M. S. Matthews (Tucson, AZ: Univ. Arizona Press), 417
Deienno, R., Izidoro, A., Morbidelli, A., Nesvorný, D., & Bottke, W. F. 2022, ApJL, 936, L24
Di Sisto, R. P., Ramos, X. S., & Beaugé, C. 2014, Icar, 243, 287
Durda, D. D., Bottke, W. F., Nesvorný, D., et al. 2007, Icar, 186, 498
Emery, J. P., Marzari, F., Morbidelli, A., French, L. M., & Grav, T. 2015, in Asteroids IV, ed. P. Michel, F. E. DeMeo, & W. F. Bottke (Tucson, AZ: Univ. Arizona Press), 203
Feroz, F., & Hobson, M. P. 2008, MNRAS, 384, 449
Feroz, F., Hobson, M. P., & Bridges, M. 2009, MNRAS, 398, 1601
Grav, T., Mainzer, A. K., Bauer, J., et al. 2011, ApJ, 742, 40
Grav, T., Mainzer, A. K., Bauer, J. M., Masiero, J. R., & Nugent, C. R. 2012, ApJ, 759, 49
Hendler, N. P., & Malhotra, R. 2020, PSJ, 1, 75
Holt, T. R., Vokrouhlický, D., Nesvorný, D., Brož, M., & Horner, J. 2020a, MNRAS, 499, 3630
Holt, T. R., Nesvorný, D., Horner, J., et al. 2020b, MNRAS, 495, 4085
Hou, X., Scheeres, D. J., & Liu, L. 2014, CeMDA, 119, 119
Hou, X., Scheeres, D. J., & Liu, L. 2016, CeMDA, 125, 451
Jewitt, D. C., Trujillo, C. A., & Luu, J. X. 2000, AJ, 120, 1140
Kalup, C. E., Molnár, L., Kiss, C., et al. 2021, ApJS, 254, 7
Levison, H. F., Shoemaker, E. M., & Shoemaker, C. S. 1997, Natur, 385, 42
Li, J., Lei, H., & Xia, Z. J. 2021, MNRAS, 505, 1730
Li, J., Xia, Z. J., Georgakarakos, N., & Yoshida, F. 2023a, AA, 674, A138
Li, J., Xia, Z. J., Yoshida, F., Georgakarakos, N., & Li, X. 2023b, A&A, 669, A68
Mainzer, A., Abell, P., Bauer, J., et al. 2021, DPS, 53, 306.16
Marschall, R., Nesvorný, D., Deienno, R., et al. 2022, AJ, 164, 167
Marzari, F., Scholl, H., Murray, C., & Lagerkvist, C. 2002, in Asteroids III, ed. W. F. Bottke et al. (Tucson, AZ: Univ. Arizona Press), 725
Marzari, F., Tricarico, P., & Scholl, H. 2003, MNRAS, 345, 1091
McNeill, A., Erasmus, N., Trilling, D. E., et al. 2021, PSJ, 2, 6
Milani, A. 1993, CeMDA, 57, 59
Morais, M. H. M. 1999, A&A, 350, 318
Morais, M. H. M. 2001, A&A, 369, 677
Morbidelli, A., Levison, H. F., Tsiganis, K., & Gomes, R. 2005, Natur, 435, 462
Mottola, S., Hellmich, S., Buie, M. W., et al. 2023, PSJ, 4, 18
Muinonen, K., Belskaya, I. N., Cellino, A., et al. 2010, Icar, 209, 542
Naidu, S. P., Chesley, S. R., & Farnocchia, D. 2017, DPS, 49, 112.04
Nakamura, T., & Yoshida, F. 2008, PASJ, 60, 293
Nesvorný, D. 2018, ARA&A, 56, 137
Nesvorný, D., Brož, M., & Carruba, V. 2015, in Asteroids IV, ed. P. Michel, F. E. DeMeo, & W. F. Bottke (Tucson, AZ: Univ. Arizona Press), 297
Nesvorný, D., Deienno, R., Bottke, W. F., et al. 2023, AJ, 166, 55
Nesvorný, D., Vokrouhlický, D., & Morbidelli, A. 2013, ApJ, 768, 45
Nesvorný, D., Vokrouhlický, D., Shelly, F., et al. 2024, Icar, 411, 115922
O'Brien, D. P., & Morbidelli, A. 2008, LPICo, 1405, 8367
Pirani, S., Johansen, A., Bitsch, B., Mustill, A. J., & Turrini, D. 2019a, A&A, 623, A169
Pirani, S., Johansen, A., & Mustill, A. J. 2019b, A&A, 631, A89
Rabe, E. 1965, AJ, 70, 687
Rabe, E. 1967, AJ, 72, 10
Robutel, P., & Gabern, F. 2006, MNRAS, 372, 1463
Rozehnal, J., Brož, M., Nesvorný, D., et al. 2016, MNRAS, 462, 2319
Schwamb, M. E., Jones, R. L., Yoachim, P., et al. 2023, ApJS, 266, 22
Shevchenko, V. G., Belskaya, I. N., Slyusarev, I. G., et al. 2012, Icar, 217, 202
Shoemaker, E. M., Shoemaker, C. S., & Wolfe, R. F. 1989, in Asteroids II, ed. R. P. Binzel, T. Gehrels, & M. S. Matthews (Tucson, AZ: Univ. Arizona Press), 487
Sicardy, B., & Dubois, V. 2003, CeMDA, 86, 321
Slyusarev, I. G., & Belskaya, I. N. 2014, SoSyR, 48, 139
Strömgren, E. 1907, AN, 175, 13
Szabó, G. M., Ivezić, Ž., Jurić, M., & Lupton, R. 2007, MNRAS, 377, 1393
Uehata, K., Terai, T., Ohtsuki, K., & Yoshida, F. 2022, AJ, 163, 213
Vereš, P., Jedicke, R., Fitzsimmons, A., et al. 2015, Icar, 261, 34
Vinogradova, T. A. 2015, MNRAS, 454, 2436
Vinogradova, T. A. 2019, MNRAS, 484, 3755
Vinogradova, T. A. 2020, IAUFM, 30, 24
Vokrouhlický, D., Nesvorný, D., Brož, M., & Bottke, W. F. 2023, A&A, 681, A23
Wolf, M. 1907, AN, 174, 63
Wolf, M., & Kopff, A. 1907, AN, 175, 191
Wong, I., & Brown, M. E. 2015, AJ, 150, 174
Wong, I., & Brown, M. E. 2023, AJ, 165, 15
Wong, I., Brown, M. E., & Emery, J. P. 2014, AJ, 148, 112
Yoder, C. F., Colombo, G., Synnott, S. P., & Yoder, K. A. 1983, Icar, 53, 431
Yoshida, F., & Terai, T. 2017, AJ, 154, 71